

---

# Methods<sup>1</sup>

---

Expedition 339 Scientists<sup>2</sup>

## Chapter contents

Introduction, background, and operations . . .	1
Lithostratigraphy . . . . .	4
Biostratigraphy . . . . .	11
Paleomagnetism . . . . .	15
Physical properties . . . . .	16
Geochemistry . . . . .	20
Downhole measurements . . . . .	24
Stratigraphic correlation . . . . .	28
References . . . . .	30
Figures . . . . .	36
Tables . . . . .	52

## Introduction, background, and operations

This chapter documents the procedures and methods employed in the various shipboard laboratories of the R/V *JOIDES Resolution* during Integrated Ocean Drilling Program (IODP) Expedition 339. This information applies only to shipboard work described in the Expedition Reports section of the Expedition 339 *Proceedings of the Integrated Ocean Drilling Program* volume. Methods for shore-based analyses of Expedition 339 samples and data will be described in individual scientific contributions to be published elsewhere. All shipboard scientists contributed to the completion of this volume.

### Site locations

GPS coordinates from precruise site surveys were used to position the vessel at all Expedition 339 sites. A SyQuest Bathymetry 2010 CHIRP subbottom profiler was used to monitor seafloor depth on the approach to each site to reconfirm the depth profiles from precruise surveys. Once the vessel was positioned at a site, the thrusters were lowered and a positioning beacon was dropped to the seafloor. The dynamic positioning control of the vessel used navigational input from the GPS system and triangulation to the seafloor beacon, weighted by the estimated positional accuracy. The final hole position was the mean position calculated from the GPS data collected over a significant portion of the time the hole was occupied. A survey of the seafloor was conducted at all sites using the underwater camera system to ensure that it was free of obstructions.

### Coring and drilling operations

All three standard coring systems, the advanced piston corer (APC), the extended core barrel (XCB), and the rotary core barrel (RCB), were used during Expedition 339. The APC was used in the upper portion of each hole when coring in the top of the hole was the objective. The APC cuts soft-sediment cores with minimal coring disturbance relative to other IODP coring systems. After the APC core barrel is lowered through the drill pipe and lands near the bit, the drill pipe is pressured up until the two shear pins that hold the inner barrel attached to the outer barrel fail. The inner barrel then advances into the formation and cuts the core (Fig.

<sup>1</sup>Expedition 339 Scientists, 2013. Methods. In Stow, D.A.V., Hernández-Molina, F.J., Alvarez Zarikian, C.A., and the Expedition 339 Scientists, *Proc. IODP, 339*: Tokyo (Integrated Ocean Drilling Program Management International, Inc.). doi:10.2204/iodp.proc.339.102.2013  
<sup>2</sup>Expedition 339 Scientists' addresses.



F1). The driller can detect a successful cut, or “full stroke,” from the pressure gauge on the rig floor.

APC refusal is conventionally defined in two ways: (1) the piston fails to achieve a complete stroke (as determined from the pump pressure reading) because the formation is too hard or (2) excessive force (>60,000 lb; ~267 kN) is required to pull the core barrel out of the formation. When a full stroke cannot be achieved, one or two additional attempts are typically made, and each time the bit is advanced by the length of recovered core. Note that this results in a nominal recovery of ~100% based on the assumption that the barrel penetrates the formation by the equivalent of the length of core recovered. When a full or partial stroke is achieved but excessive force cannot retrieve the barrel, the core barrel is sometimes “drilled over,” meaning after the inner core barrel is successfully shot into the formation, the drill bit is advanced to total depth to free the APC barrel.

Nonmagnetic core barrels were used during all conventional APC coring to a pull force of ~40,000 lb. Most APC cores recovered during Expedition 339 were oriented using the FlexIt tool (see “[Paleomagnetism](#)”). Formation temperature measurements were made to obtain temperature gradients and heat flow estimates (see “[In situ temperature measurements](#)”).

The XCB system was used to advance the hole when APC refusal occurred before the target depth was reached or when the formation became either too stiff for APC coring or hard substrate was encountered. The XCB is a rotary system with a small cutting shoe that extends below the large rotary APC/XCB bit. The smaller bit can cut a semi-indurated core with less torque and fluid circulation than the main bit, optimizing recovery. The XCB cutting shoe (bit) extends ~30.5 cm ahead of the main bit in soft sediments but retracts into the main bit when hard formations are encountered (Fig. F2). The XCB system was used extensively during Expedition 339 to greater depths than anticipated.

The bottom-hole assembly (BHA) is the lowermost part of the drill string. The exact configuration of the BHA is reported in the operations section in each site chapter. A typical APC/XCB BHA consists of a drill bit (outer diameter =  $11\frac{7}{16}$  inch), a bit sub, a seal bore drill collar, a landing saver sub, a modified top sub, a modified head sub, a nonmagnetic drill collar (for APC/XCB), a number of 8 inch (~20.32 cm) drill collars, a tapered drill collar, six joints (two stands) of  $5\frac{1}{2}$  inch (~13.97 cm) drill pipe, and one crossover sub. A lockable flapper valve was used so that down-hole logs could be collected without dropping the bit when APC/XCB coring.

The RCB was deployed when XCB coring rates diminished below an acceptable level or the bit was destroyed by the increasingly hard formation. The RCB is the most conventional rotary drilling system and was used during Expedition 339 to drill and core the deepest holes. The RCB requires a dedicated RCB BHA and a dedicated RCB drilling bit. The BHA used for RCB coring included a 9 inch RCB drill bit, a mechanical bit release, a modified head sub, an outer core barrel, a modified top sub, and seven control-length drill collars followed by a tapered drill collar to the  $5\frac{1}{2}$  inch drill pipe (Fig. F3). Most cored intervals were ~9.5 m long, which is the length of a standard core barrel and the length of a joint of drill pipe. In some cases, the drill string was drilled or “washed” ahead without recovering sediments to advance the drill bit to a target depth to resume core recovery. Such intervals were typically drilled using a center bit installed within the RCB bit.

### IODP depth conventions

Primary depth scale types are based on the measurement of drill string length (e.g., drilling depth below rig floor [DRF] and drilling depth below seafloor [DSF]), length of core recovered (e.g., core depth below seafloor [CSF] and core composite depth below seafloor [CCSF]), and logging wireline (e.g., wireline log depth below rig floor [WRF] and wireline log depth below seafloor [WSF]). All units are in meters. The relationship between scales is defined either by protocol, such as the rules for computation of CSF from DSF, or user-defined correlations, such as stratigraphic correlation of cores between holes to create a common CCSF scale from the CSF scales used in each hole. The distinction in nomenclature should keep the user aware that a nominal depth value at two different depth scales usually does not refer to exactly the same stratigraphic interval (also see “[Curatorial procedures and sample depth calculations](#)”).

For editorial convenience, the depth scale type acronym was not repeated with each depth reference in the site chapters. The scale type was declared at the beginning of each section and only mentioned again if a different scale type was used.

### Core handling and analysis

The coring strategy for Expedition 339 consisted of APC coring in two holes (A and B) at each site to refusal, except at Site U1385 where five holes were cored with the APC. Multiple holes allowed us to build a composite section at each site. The drillover technique was employed to maximize APC penetration where desirable. APC refusal was followed by XCB coring at each site to ~350 meters below sea-

floor (mbsf) (except at Site U1385 where only the APC was used to ~150 mbsf) and then by RCB coring to total depth when necessary.

Cores recovered during Expedition 339 were extracted from the core barrel in 67 mm diameter plastic liners. These liners were carried from the rig floor to the core processing area on the catwalk outside the Core Laboratory, where they were split into ~1.5 m sections. Liner caps (blue = top; colorless = bottom) were glued with acetone onto liner sections on the catwalk by the Marine Technicians. The length of each section was entered into the database as “created length” using the Sample Master application. This number was used to calculate core recovery.

As soon as cores arrived on deck, headspace samples were taken using a syringe for immediate hydrocarbon analysis as part of the shipboard safety and pollution prevention program. Core catcher samples were taken for biostratigraphic analysis. Whole-round samples were taken from some core sections for shipboard and postcruise interstitial water analyses. Rhizon interstitial water samples and syringe samples were taken from selected intervals in addition to whole rounds (see “[Geochemistry](#)”). In addition, whole-round and syringe samples were immediately taken from the ends of cut sections at three sites for shore-based microbiological analysis.

Core sections were then placed in core racks in the laboratory. When the cores reached equilibrium with laboratory temperature (typically after ~4 h), whole-round core sections were run through the Whole-Round Multisensor Logger (WRMSL; measuring *P*-wave velocity, density, magnetic susceptibility, and resistivity) and the Natural Gamma Radiation Logger (NGRL). Thermal conductivity measurements were typically taken at a rate of two per core (see “[Physical properties](#)”). The core sections were then split lengthwise from bottom to top into working and archive halves. Investigators should note that older material may have been transported upward on the split face of each section during splitting. The working half of each core was sampled for shipboard analysis (biostratigraphy, physical properties, carbonate, paleomagnetism, and bulk X-ray diffraction [XRD] mineralogy). The archive half of each core was scanned on the Section Half Imaging Logger (SHIL) and measured for color reflectance and magnetic susceptibility on the Section Half Multisensor Logger (SHMSL). At the same time, the archive halves were described visually and by means of smear slides. Finally, the archive halves were run through the cryogenic magnetometer. Both halves of the core were then put into labeled plastic tubes that were sealed and transferred to cold storage space aboard the ship. At the end of the expedition, the cores were trans-

ported from the ship to permanent cold storage at the Bremen Core Repository (BCR) at the University of Bremen, Germany. The BCR houses cores collected from the Atlantic and Arctic Oceans (north of the Bering Strait). A postexpedition sampling party was organized and carried out at the BCR from 9 to 17 June 2012 to take personal samples requested by members of the science party.

### Drilling disturbance

Cores may be significantly disturbed as a result of the drilling process and contain extraneous material as a result of the coring and core handling process. In formations with loose sand layers, sand from intervals higher in the hole may be washed down by drilling circulation, accumulate at the bottom of the hole, and be sampled with the next core. The uppermost 10–50 cm of each core must therefore be examined critically during description for potential “cave-in.” Common coring-induced deformation includes the concave-downward appearance of originally horizontal bedding. Piston action may result in fluidization (flow-in) at the bottom of APC cores. Retrieval from depth to the surface may result in elastic rebound. Gas that is in solution at depth may become free and drive core segments within the liner apart. Both elastic rebound and gas pressure can result in a total length for each core that is longer than the interval that was cored and thus a calculated recovery of >100%. If gas expansion or other coring disturbance results in a void in any particular core section, the void can be either closed by moving material if very large, stabilized by a foam insert if moderately large, or left as is. When gas content is high, pressure must be relieved for safety reasons before the cores are cut into segments. This is accomplished by drilling holes into the liner, which forces some sediment as well as gas out of the liner. These disturbances are described in the “Lithostratigraphy” sections in each site chapter and graphically indicated on the core summary graphic reports (visual core descriptions [VCDs]). In extreme instances core material was ejected from the core barrel, sometimes violently, onto the rig floor by high pressure in the core or other coring problem. This core material was replaced in the plastic core liner by hand and should not be considered to be in stratigraphic order. Core sections so affected are marked by a yellow label marked “disturbed,” and the nature of the disturbance is noted in the coring log.

### Curatorial procedures and sample depth calculations

The numbering of sites, holes, cores, and samples followed standard IODP procedure. A full curatorial

sample identifier consists of the following information: expedition, site, hole, core number, core type, section number, and interval in centimeters measured from the top of the core section. For example, a sample identification of “339-U1386A-1H-2, 10–12 cm,” represents a sample taken from the interval between 10 and 12 cm below the top of Section 2 of Core 1 (“H” designates that this core was taken with the APC system, “X” designates XCB cores, and “R” designates RCB cores) of Hole A of Site U1386 during Expedition 339. The “U” preceding the hole number indicates that the hole was drilled by the United States Implementing Organization (USIO) platform, the *JOIDES Resolution*.

Cored intervals are defined by the core top depth in DSF and the distance the driller advanced the bit and core barrel in meters. The length of the core is defined by the sum of lengths of the core sections. The CSF depth of a sample (referred to as mbsf) is calculated by adding the offset of the sample below the section top and the lengths of all higher sections in the core to the core top depth measured with the drill string (DSF). A soft to semisoft sediment core from less than a few hundred meters below seafloor expands upon recovery (typically a few percent to as much as 15%), so the recovered interval typically does not match the cored interval. In addition, a gap typically occurs between cores, as shown by composite depth construction. Thus, a discrepancy between DSF and CSF depths can exist with regard to a stratigraphic interval. Furthermore, when more than 100% of the cored interval is recovered, the CSF depth of a sample taken from the bottom of a core will be deeper than that of a sample from the top of the subsequent core (i.e., the data associated with the two core intervals overlap on the CSF depth scale).

If a core has incomplete recovery, all cored material is assumed to originate from the top of the drilled interval as a continuous section for curation purposes. The true depth interval within the cored interval is unknown and should be considered a sample depth uncertainty in age-depth analyses and in the correlation of core data with downhole logging data.

### Authorship of site chapters

The separate sections of the site chapters and “Methods” chapter were written by the following shipboard scientists (authors are listed in alphabetical order; no seniority is implied):

Background and objectives: C.A. Alvarez Zarikian, F.J. Hernández-Molina, D.A.V. Stow  
Operations: C.A. Alvarez Zarikian, R. Grout

Lithostratigraphy: E. Ducassou, R. Flood, S. Furota, L. Krissek, J. Kuroda, F. Nanayama, N. Nishida, C. Roque, C. Sloss, Y. Takashimizu  
Biostratigraphy: C.A. Alvarez Zarikian, B. Balestra, J.-A. Flores, P. Grunert, B. Li, M.F. Sanchez Goñi, F.J. Sierro, A.D. Singh, A. Voelker  
Paleomagnetism: C. Richter, C. Xuan  
Physical properties: A. Bahr, F. Jimenez-Espejo, E. Llave  
Geochemistry: D. Hodell, J.K. Kim, M. Miller, A. Tzanova  
Downhole measurements: J. Lofi, T. Williams  
Stratigraphic correlation: G. Acton, L. Lourens

## Lithostratigraphy

This section outlines the methods used to describe the sedimentary successions recovered during Expedition 339, including core description, core imaging (SHIL), color spectrophotometry and magnetic susceptibility (SHMSL), XRD analyses, smear slide description, and hand-drawn logs. Only general procedures are outlined, except where they depart significantly from IODP conventions.

### Sediment classification

The sediment recovered during Expedition 339 are composed of biogenic and siliciclastic components. They were described using a classification scheme derived from those of Ocean Drilling Program (ODP) Leg 155 (Shipboard Scientific Party, 1995), IODP Expedition 303 (Expedition 303 Scientists, 2006), and Stow (2005). The biogenic component is composed of the skeletal debris of open-marine calcareous and siliceous microfauna (e.g., foraminifers and radiolarians), microflora (e.g., calcareous nannofossils and diatoms), and macrofossil shell fragments. The siliciclastic component is composed of mineral and rock fragments derived from igneous, sedimentary, and metamorphic rocks. The relative proportion of these two components is used to define the major classes of sediments in this scheme (Fig. F4).

Naming conventions for Expedition 339 follow the general guidelines of the ODP sediment classification scheme (Mazzullo et al., 1988), with the exception that a separate “mixed sediment” category was not distinguished during Expedition 339. As a result, biogenic sediments are those that contain >50% biogenic grains and <50% siliciclastic grains, whereas siliciclastic sediments are those that contain >50% siliciclastic grains and <50% biogenic grains. Sediments containing >50% silt- and sand-sized volcanic grains are classified as ash layers. During Expedition 339, no ash layers or neritic and chemical sediments

were encountered except as accessory components; therefore, these categories are not addressed below. Sediment grain-size divisions for both biogenic and siliciclastic components are based on Wentworth (1922), with eight major textural categories defined on the basis of the relative proportions of sand-, silt-, and clay-sized particles (Fig. F5); however, distinguishing between some of these categories can be difficult (e.g., silty mud versus sandy mud) without accurate measurements of grain size abundances. The term “clay” is only used to describe particle size and is applied to both clay minerals and all other grains <4 µm in size. Size-textural qualifiers were not used for biogenic sediment names (e.g., nannofossil clay implies that the dominant component is detrital clay rather than clay-sized nannofossils).

The lithologic names assigned to these sediments consist of a principal name and modifiers based on composition and degree of lithification and/or texture as determined from visual description of the cores and from smear slide observations. The total calcium carbonate content of the sediments, determined on board (see “**Sedimentary inorganic and organic carbon**”), also aided in classification.

For a sediment that contains >90% of one component (either the siliciclastic or biogenic component), only the principal name is used. For sediments with >90% biogenic components, the name applied indicates the most limited group of grains that exceed the 90% threshold value. For example, a sediment composed of >90% calcareous nannofossils is called a nannofossil ooze, a sediment composed of 50% foraminifers and 45% calcareous nannofossils is called a calcareous ooze, and a sediment composed of 40% foraminifers, 40% calcareous nannofossils, and 15% diatoms is called a biosiliceous calcareous ooze. For sediment with >90% siliciclastic grains, the principal name is based on the textural characteristics of all sediment particles (both siliciclastic and biogenic) (Fig. F5).

For sediment that contains a significant mixture of siliciclastic and biogenic components (between 25% and 75% of both siliciclastic and biogenic components), the principal name is determined by the more abundant component. If the siliciclastic component is more abundant, the principal name is based on the textural characteristics of all sediment particles (both siliciclastic and biogenic) (Fig. F5). If the biogenic component is more abundant, the principal name is either (1) based on the predominant biogenic component if that component forms >75% of the biogenic particles or (2) the more encompassing term “biogenic ooze.”

If one component forms 75%–90% of the sediment, then the principal name is followed by a minor mod-

ifier (e.g., “with diatoms”), with the minor modifier based on the most abundant component that forms 10%–25% of the sediment. If the minor component is biogenic, then the modifier describes the most limited group of grains that exceeds the 10% abundance threshold. If the minor component is siliciclastic, the minor modifier is based on the texture of the siliciclastic fraction.

If one component forms 50%–75% of the sediment, then the principal name is preceded by a major modifier that is based on the component that forms 25%–50% of the sediment. If the less abundant component is biogenic, then the major modifier describes the most limited group of grains that exceeds the 25% abundance threshold (e.g., nannofossil versus calcareous versus biogenic). If the less abundant component is siliciclastic, the major modifier is based on the texture of the siliciclastic fraction.

If the primary lithology for an interval of core has a major modifier, then that major modifier is indicated in the Graphic lithology column of the VCD sheets using a modified version of the lithologic pattern for the primary lithology (Fig. F6). The modified lithologic patterns are shown in Figure F7. The minor modifiers of sediment lithologies are not included in the Graphic lithology column.

The following terms describe lithification that varies depending on the dominant composition:

- Sediment composed predominantly of calcareous, pelagic organisms (e.g., calcareous nannofossils and foraminifers): the lithification terms “ooze” and “chalk” reflect whether the sediment can be deformed with a finger (ooze) or can be scratched easily by a fingernail (chalk).
- Sediments composed predominantly of siliceous microfossils (diatoms, radiolarians, and siliceous sponge spicules): the lithification terms “ooze” and “radiolarite/spiculite/diatomite” reflect whether the sediment can be deformed with a finger (ooze) or cannot be easily deformed manually (radiolarite/spiculite/diatomite).
- Sediments composed of a mixture of calcareous pelagic organisms and siliceous microfossils and sediments composed of a mixture of siliceous microfossils: the lithification terms “ooze” and “indurated sediment” reflect whether the sediment can be deformed with a finger (ooze) or cannot be easily deformed manually (indurated sediment).
- Sediments composed predominantly of siliciclastic material: if the sediment can be deformed easily with a finger, no lithification term is added and the sediment is named for the dominant grain size (i.e., sand, silt or clay). For more consolidated

material, the lithification suffix “-stone” is appended to the dominant size classification (e.g., claystone).

- Sediments composed of sand-sized volcanoclastic grains: if the sediment can be deformed easily with a finger, the interval is described as “ash.” For more consolidated material, the rock is called “tuff.”

## Visual core description

### Preparation for core description

The standard method of splitting a core by pulling a wire lengthwise through its center tends to smear the cut surface and obscure fine details of lithology and sedimentary structure. When necessary during Expedition 339, the archive halves of cores were gently scraped across, rather than along, the core section using a stainless steel or glass scraper to prepare the surface for unobscured sedimentologic examination and digital imaging. Scraping parallel to bedding with a freshly cleaned tool prevented cross-stratigraphic contamination.

### Sediment visual core description sheets

VCD sheets provide a summary of the data obtained during shipboard analysis of each sediment core. Detailed observations of each section were initially recorded by hand on paper, adjacent to the printed scanned image of that section. Copies of these original descriptions were scanned and converted to PDF files and are included in the DRAWVCD folder in [“Supplementary material.”](#) This information was subsequently entered into the DESClogik software, which provides data that can be used in Strater to generate a simplified, annotated graphical description (VCD) for each core (Fig. F6). Site, hole, and depth (in meters core depth below seafloor [CSF-A], also called mbsf or meters composite depth [mcd], if available) are given at the top of the VCD sheet, with the corresponding depths of core sections along the left margin. Columns on the VCD sheets include Lithologic unit, Core image, Graphic lithology, Coring disturbance (type and intensity), Average grain size, Sedimentary structures, Lithological accessories, Bioturbation intensity, Shipboard samples, Age, and Color. Profiles of magnetic susceptibility, natural gamma radiation (NGR), and reflectance ( $L^*$ ,  $a^*$ , and  $b^*$ ) are also included. These columns are discussed in more detail below.

### Graphic lithology

Lithologies of the core intervals recovered are represented on the VCD sheets by graphic patterns in the Graphic lithology column, using the symbols illus-

trated in Figure F7A. A maximum of two different lithologies (for interbedded sediments) can be represented within the same core interval. The major modifier of a primary lithology is shown using a modified version of the primary lithology pattern. A secondary lithology present as interbeds within the primary lithology is shown by a pattern along the right side of the column, with a solid vertical line dividing the primary and secondary lithologies. Lithologic abundances are rounded to the nearest 10%; lithologies that constitute <10% of the core are generally not shown but are listed in the Description section. However, some distinctive secondary lithologies, such as ash layers, are included graphically in the Graphic lithology column as the primary lithology for a thin stratigraphic interval. Relative abundances of lithologies reported in this way are useful for general characterization of the sediment but do not constitute precise, quantitative observations.

### Hand-drawn logs (draw logs)

The hand-drawn logs, which were drafted after the cruise, are a representation of the recovered sediment sequence made by Expedition 339 sedimentologist Emmanuelle Ducassou based on the visual descriptions of the core as recorded on the VCD sheets and in core photos. These graphic representations were drawn at the vertical scale of one square to 50 cm, with the core and section indicated on the left. Drafted (numerically drawn) hand-drawn logs are included in the DRAWLOG folder in [“Supplementary material”](#) for Sites U1385–U1388. An example log from Hole U1386A is shown in Figure F8, and the legend for the logs at Site U1386 is shown in Figure F9.

The average grain size is represented by a curve. The first line to the right represents a mud average grain size, the second line represents a silt average grain size, and the third line represents a sand average grain size. Clay or ooze is represented by half of the spacing corresponding to mud average grain size, and coarse sandy grains or pebbles are represented by a half spacing to the right of the sand average grain size. Other gradations for specific isolated or unique sedimentary characteristics have been included in the logs and legends for individual sites.

The lithologies are represented by patterns as follows:

- Mud and clay/ooze are represented by a gray color based on the Munsell color assigned (Munsell Color Company, Inc., 1994) (lighter gray = 6, medium gray = 4 and 5, darker gray = 3),
- Silty mud is represented by alternating dots and dashes,

- Sandy mud and sandy silt are represented by dots and few dashes,
- Silty sand is represented by dots, and
- Granules and pebbles are represented by large open dots.

Contacts are represented as follows:

- Gradational contact: no horizontal line is drawn and there is a gradational curve between the two lithologies.
- Bioturbated contact: no horizontal line is drawn. Occasionally, a burrow is drawn at the right of the average grain size curve to show if the contact is sharp and bioturbated.
- Irregular contact: an irregular horizontal line is drawn by hand between the two lithologies.
- Sharp contact: a ruled straight line is drawn between the two lithologies and a dash is shown to the right of the curve.
- Erosional/scoured contact: a wavy line is drawn between the two lithologies and a short wavy dash is shown to the right of the curve.

Debrisites are represented by a drawing of the described clasts, and the matrix is represented with one of the patterns corresponding at the observed lithology. Identified slumps are represented by contorted strata, and presumed slumps are represented by “SS?” at the right of the intervals. Shelly sediments and shell hash are represented by small drawings to the right of the average grain size curve, woody fragments are represented by a leaf, parallel laminated sediments are represented by three small dashes arranged vertically, and cross laminations are represented by two small dashes forming a small angle.

The contact between cores is represented continuously if the previous core is full and the lithologies between the two cores are the same. If this is not the case, a small space is shown between the core catcher of the previous core and the first section of the following core.

Other specific annotations have been included at the right of the average grain size, such as a reddish or a greenish color, or “rock” in the case of fully indurated/lithified sediment.

### **Bioturbation**

Six levels of bioturbation are recognized using the scheme similar to that of Droser and Bottjer (1986). Bioturbation intensity is classified as complete (100%), heavy (>60%), moderate (40%–60%), slight (10%–40%), sparse (<10%), and absent (none). These levels are illustrated with a numeric scale in the Bioturbation intensity column.

### **Stratification and sedimentary structures**

The locations and types of stratification and sedimentary structures visible on the prepared surfaces of the split cores are shown in the Sedimentary structures column of the VCD sheet. Symbols in this column indicate the locations and scales of interstratification, as well as the locations of individual bedding features and any other sedimentary features, such as scours, ash layers, ripple laminations, and fining-upward, coarsening-upward, or bi-gradationally bedded intervals (Fig. F7B).

For Expedition 339, the following terminology (based on Stow, 2005) was used to describe the scale of stratification:

- Thin lamination = <3 mm thick.
- Medium lamination = 0.3–0.6 cm thick.
- Thick lamination = 0.6–1 cm thick.
- Very thin bed = 1–3 cm thick.
- Thin bed = 3–10 cm thick.
- Medium bed = 10–30 cm thick.
- Thick bed = 30–100 cm thick.
- Very thick bed = >100 cm thick.

### **Lithologic accessories**

Lithologic, diagenetic, and paleontologic accessories, such as nodules, sulfides, and shells, are indicated on the VCD sheets. The symbols used to designate these features are shown in Figure F7B. The following terminology was used to describe the abundance of lithologic accessories observed during visual core description:

- Barren = none observed per section of core.
- Present = 1 observed per section of core.
- Rare = 2–10 observed per section of core.
- Few = 10–20 observed per section of core.
- Common = 20–50 observed per section of core.
- Abundant = >50 observed per section of core.

### **Sediment disturbance**

Drilling-related sediment disturbance is recorded in the Disturbance column using the symbols shown in Figure F7B. The style of drilling disturbance is described for soft and firm sediments using the following terms:

- Fall-in: out-of-place material at the top of a core has fallen downhole onto the cored surface.
- Bowed: bedding contacts are slightly to moderately deformed but still subhorizontal and continuous.
- Flow-in, coring/drilling slurry, along-core gravel/sand contamination: soft-sediment stretching and/or compressional shearing structures are severe and are attributed to coring/drilling. The

particular type of deformation may also be noted (e.g., flow-in, gas expansion, etc.).

- Soupy or mousselike: intervals are water saturated and have lost all aspects of original bedding.
- Biscuit: sediments of intermediate stiffness show vertical variations in the degree of disturbance. Softer intervals are washed and/or soupy, whereas firmer intervals are relatively undisturbed.
- Cracked or fractured: firm sediments are broken but not displaced or rotated significantly.
- Fragmented or brecciated: firm sediments are pervasively broken and may be displaced or rotated.

### Shipboard samples

Sample material taken for shipboard sedimentologic and chemical analyses consisted of interstitial water whole rounds, micropaleontology samples, smear slides, and discrete samples for XRD and carbonate analysis. Typically, 1–5 smear slides were made per core. One interstitial water sample and one microbiology sample were taken at designated intervals (so that core is missing from those intervals), and a micropaleontology sample was obtained from the core catcher of most cores. XRD samples were taken from core catchers at some sites and from a split of the carbonate sample at other sites. Additional samples were selected to better characterize lithologic variability within a given interval. Tables summarizing relative abundance of sedimentary components from the smear slides were also generated.

### Color

Color is determined qualitatively using Munsell Soil Color Charts (Munsell Color Company, Inc., 1994) and described immediately after cores are split to minimize color changes associated with drying and redox reactions. When portions of the split core surface required cleaning with a stainless steel or glass scraper, this was done prior to determining the color. Munsell color names and the corresponding hue and chroma value are provided in the Color column on the VCD sheets.

### Remarks

The written description at the top of the VCD sheets for each core contains a brief overview of primary and secondary lithologies present, as well as notable features such as sedimentary structures, grading, and disturbances resulting from the coring process. Note that the fossil identified as scaphopod during the on-board visual description of the lithostratigraphy has subsequently been identified as *Arenaria*. This has been changed for the reports; however, “scaphopod”

will still appear in the VCD sheets and DESClogik output.

### Smear slides

Smear slide samples were taken from the archive halves during core description. For each sample, a small amount of sediment was removed with a wooden toothpick, dispersed evenly in deionized water on a 25 mm × 75 mm glass slide, and dried on a hot plate at a low setting. A drop of mounting medium and a 22 mm × 30 mm cover glass were added, and the slide was placed in an ultraviolet light box for ~15 min. Once fixed, each slide was scanned at 100×–200× with a transmitted light petrographic microscope using an eyepiece micrometer to assess grain-size distributions in clay (<4 μm), silt (4–63 μm), and sand (>63 μm) fractions. The eyepiece micrometer was calibrated once for each magnification and combination of ocular and objective, using an inscribed stage micrometer.

Relative proportions of each grain size and type were estimated by microscopic examination. Note that smear slide analyses tend to underestimate the abundance of sand-sized and larger grains (e.g., foraminifers, radiolarians, and siliciclastic sand) because these are difficult to incorporate into the smear. Clay-sized biosilica, which is transparent and isotropic, is also very difficult to quantify. Clay minerals, micrite, and nanofossils can also be difficult to distinguish at the very finest (<4 μm) size range. After scanning for grain-size distribution, several fields were examined at 200×–500× for mineralogic and microfossil identification. Standard petrographic techniques were employed to identify the commonly occurring minerals and biogenic groups, as well as important accessory minerals and microfossils.

Smear slide analysis data tables are included in “[Core descriptions.](#)” These tables include information about the sample location, description of where the smear slide was taken, the estimated percentages of texture (i.e., sand, silt, and clay), and the estimated percentages of composition (i.e., ash, siliciclastics, detrital carbonate, biogenic carbonate, and biogenic silica). Relative abundances of identified components such as mineral grains, microfossils, and biogenic fragments were assigned on a semi-quantitative basis using the following abbreviations:

- A = abundant (>20% of field of view).
- C = common (>5%–20% of field of view).
- F = few (1%–5% of field of view).
- R = rare (<1% field of view).
- P = present (1 per 1–10 fields of view).
- B = barren (none in field of view).

For smear slide data from Site U1385 only, note that subsequent comparison to carbonate contents determined geochemically indicated that smear slide estimates were too high by a factor of ~2. The smear slide data and individual VCD sheets have not been corrected for this overestimation, but the lithologic names used in “**Lithostratigraphy**” in the “Site U1385” chapter [Expedition 339 Scientists, 2013] were adjusted to indicate the lower carbonate content. The adjusted lithologies also are used in the summary lithologic columns shown for Site U1385.

### Section Half Multisensor Logger

Spectrophotometry and magnetic susceptibility of the archive-section halves were measured with the SHMSL. The SHMSL takes measurements in empty intervals and intervals where the core surface is well below the level of the core liner but cannot recognize relatively small cracks, disturbed areas of core, or plastic section dividers. Thus, SHMSL data may contain spurious measurements, which should be edited out of the data set by the user. Additional detailed information about measurement and interpretation of spectral data can be found in Balsam et al. (1997, 1998) and Balsam and Damuth (2000).

### Spectrophotometry

Reflectance of visible light from the archive halves of sediment cores was measured using an Ocean Optics USB4000 spectrophotometer mounted on the automated SHMSL. Freshly split soft cores were covered with clear plastic wrap and placed on the SHMSL. Measurements were taken at 2.0 cm spacing at Site U1385 and at 5.0 cm spacing at all other sites to provide a high-resolution stratigraphic record of color variations for visible wavelengths. Each measurement was recorded in 2 nm wide spectral bands from 400 to 900 nm.

### Magnetic susceptibility

Magnetic susceptibility was measured with a Bartington Instruments MS2E point sensor (high-resolution surface-scanning sensor) on the SHMSL. Because the SHMSL demands flush contact between the magnetic susceptibility point sensor and the split core, measurements were made on the archive halves of split cores that were covered with clear plastic wrap. Measurements were taken at 2.0 cm spacing at Site U1385 and at 5.0 cm spacing at all other sites. Measurement resolution was 1.0 SI, and each measurement integrated a volume of 10.5 mm × 3.8 mm × 4 mm, where 10.5 mm is the length perpendicular to the core axis, 3.8 mm is the width along the core axis, and 4 mm is the depth into the core. Only one

measurement was taken at each measurement position.

### X-ray diffraction analysis

Samples for XRD analyses were selected from the working half of sections the first time a particular depth interval was cored. In general, one 5 cm<sup>3</sup> sample was taken per core, with the sample mostly taken in Section 5 or 6. Whatever lithology was present at that depth interval was sampled. Additional samples were occasionally taken and analyzed based on visual core observations (e.g., color variability and visual changes in lithology and texture) and smear slides. Except for Site U1385, samples taken once per core for X-ray analysis were generally also analyzed for sedimentary inorganic (i.e., carbonate analysis) and organic (i.e., CHNS analysis) carbon in the Geochemistry Laboratory (see “**Geochemistry**”). Samples analyzed for bulk mineralogy were freeze-dried in the case of unlithified samples and ground by hand or in an agate ball mill, as necessary. Prepared samples were top-mounted onto a sample holder and analyzed using a Bruker D-4 Endeavor diffractometer mounted with a Vantec-1 detector using nickel-filtered CuK $\alpha$  radiation. The standard locked coupled scan was as follows:

Voltage = 37 kV.

Current = 40 mA.

Goniometer scan = 4°–70°2 $\theta$ .

Step size = 0.0174°2 $\theta$ .

Scan speed = 1 s/step.

Divergence slit = 0.3 mm.

Shipboard results yielded only qualitative results on the presence and relative abundances of the most common mineralogical components.

Diffractograms of bulk samples were evaluated with the aid of the EVA software package, which allowed for mineral identification and basic peak characterization (e.g., base line removal and maximum peak intensity). Files were created that contained d values, diffraction angles, and peak intensities without and with background removed. These files were scanned by a computer program to find d spacing values characteristic of a limited range of minerals, using quartz or calcite as an internal standard, that we anticipated would be present in the sediments and that had peaks with little interference from other minerals present in the sample (Table T1) (Cook et al., 1975; Flood, 1978; Shipboard Scientific Party, 1995). Peak intensities were reported for each mineral identified in an effort to provide a semiquantitative measure about how each mineral identified varied down-hole and between sites. Although some of the secondary peaks were checked to confirm the min-

eral identifications for some samples, not all sample identifications were checked to be sure that there were no false identifications. Thus, if the peak of a rare mineral fell within the detection window of a mineral to be identified, then the identification of the mineral will be wrong. Also, on occasion there were peaks on the XRD patterns that did not match the minerals being searched, and the materials responsible for those peaks have not yet been identified. Digital files with the diffraction patterns are available from the IODP Laboratory Information Management System (LIMS) database ([iodp.tamu.edu/tasapps/](http://iodp.tamu.edu/tasapps/)).

Glauconite is one mineral that was often identified in smear slides but not identified in the XRD data. A diffraction pattern was run on a sample of glauconitic sand recovered from a core catcher and on a standard in the shipboard XRD. The resulting pattern showed a broad peak from  $\sim 7^\circ$  to  $9^\circ 2\theta$ , suggesting an amorphous structure, and then numerous peaks at angles higher than  $19^\circ 2\theta$ . However, no single peak was identified that would allow us to quantify glauconite in these samples.

One way to evaluate the potential usefulness of the bulk X-ray intensities is to compare the peak intensities to an independent measurement of the same material. As noted previously, XRD studies and  $\text{CaCO}_3$  determinations (sample code COUL) were generally made on the same samples starting with Site U1386, and thus we can compare percent  $\text{CaCO}_3$  with peak intensity of the carbonate minerals, calcite, and dolomite (aragonite was only rarely observed in these samples; Fig. F10). For the purposes of this analysis, we have added together the values of the calcite ( $\text{CaCO}_3$ ) and dolomite ( $\text{CaMg}[\text{CO}_3]_2$ ) XRD peaks to compare with percent  $\text{CaCO}_3$  from the COUL analysis. The resulting plot shows a fairly good relationship between  $\text{CaCO}_3$  percentage and peak height with some noticeable exceptions. In particular, the sample with the highest peak intensity has an intermediate  $\text{CaCO}_3$  percentage. This sample (339-U1387C-45R-1W, 76–77 cm) is from a sandstone rock which has a calcite cement. The recrystallized calcite apparently creates a much stronger reflection than the biogenic carbonate, detrital calcium carbonate, authigenic dolomite, or detrital dolomite that make up the rest of the samples analyzed. Except for this sample, these data suggest that there is a good correlation between the intensity of a particular X-ray peak and the amount of that material in a sediment sample.

Clay minerals were also of interest to this study, and clay mineral analyses were used in two ways during Expedition 339. First, the clay minerals chlorite, illite, and kaolinite make identifiable peaks. We con-

firmed the presence of kaolinite by heating a sample to  $550^\circ\text{C}$  and noting that the kaolinite peak disappeared. We could not identify any particular peak for smectite, but we did observe that there was a region of raised baseline between peaks identified for illite and chlorite. At Site U1385, the bulk samples were glycolated to expand the smectite minerals, and this treatment depressed the baseline between illite and chlorite to more normal levels and created a broad peak near  $4.96^\circ 2\theta$ ,  $d$  spacing  $17.8 \text{ \AA}$ , as expected for smectite. It was not possible to treat all bulk samples with glycolation, so, based on the analysis of glycolated and untreated bulk mineralogy samples from Site U1385, we estimate the smectite peak intensity using the following method. A baseline is drawn from  $5.8^\circ$  to  $9.5^\circ 2\theta$  on the diffraction plot, and the number of counts between that baseline and the diffraction trace at  $7.85^\circ 2\theta$  was measured. Multiplying this value by 1.27 and adding 242 resulted in a number that closely matched the glycolated smectite peak at  $4.96^\circ 2\theta$ . This value was used to characterize smectite on bulk XRD samples during Expedition 339.

For selected samples, clay materials were separated from the coarser sediments and scanned separately as oriented samples. The separated clay material was scanned before treatment, subjected to ethylene glycol treatment, and then scanned again to allow additional analysis of the clay mineral fraction. At Site U1385, clays were separated from a few of the samples, treated with ethylene glycol, and rescanned. No treatment was done at Site U1386, but the clay fraction was separated by centrifuge on a portion of the sample from every fourth core from Sites U1387–U1391. We did not interpret these later analyses in terms of clay mineral percentages, but instead the X-ray diffractograms for both the untreated and treated samples are shown to allow a qualitative evaluation of the nature of the clay mineral assemblage. The digital diffraction patterns are available from the IODP LIMS database ([iodp.tamu.edu/tasapps/](http://iodp.tamu.edu/tasapps/)).

The clay separation method is described in the X-Ray Diffractometer User Guide onboard the *JOIDES Resolution* as follows:

1. Bulk sample ( $1 \text{ cm}^3$ ; fresh, not freeze-dried) sediment was mixed with 1% borax solution (total of 30 mL of solution). The sample/borax solution was placed in a dismembrator for 2 min.
2. The sample/borax solution was centrifuged at 1500 rpm for 5 min to remove the particle size fraction  $>2 \mu\text{m}$ .
3. The sample/borax solution was decanted into a new centrifuge tube and spun at 1500 rpm for 15 min to remove the remaining  $\sim 2 \mu\text{m}$  particle size fraction.

4. The sample/borax solution was decanted, and the remaining clay residue was washed with distilled water.
5. The distilled water and clay residue was centrifuged at 1500 rpm for 15 min to help remove any borax from the clay residue. These last two steps were repeated.
6. An oriented clay mount was made on a zero-background single-crystal quartz disk by placing several drops of solution onto the quartz disk and allowing it to dry in the desiccator.
7. The quartz disk with the clay material was placed in a sample holder and was scanned using the same settings as for the bulk samples, except that the scanning range was 4°–35°2θ.

### Digital color imaging

The archive half of each core was placed in the SHIL. The high-resolution digital core images were used to generate digital images that aided in core description. The SHIL collects digital images with three line-scan charge-coupled device arrays (2048 pixels each) behind an interference filter to create three channels (red, green, and blue). The image resolution is fixed at 20 lines at 500 dpi, and image acquisition was controlled by a 2 nm encoder. A constant aperture setting of f/22 was used. The SHIL system was calibrated with a white, mid-gray, and dark gray color chip (QPCard 101) placed at the top of each section that was checked frequently. A microscanner was used to identify samples, and the software-generated digital label was appended to the image.

For each section, scanned output from the SHIL included an ROI file of the original data with links to the TIFF file and an enhanced, uncropped JPEG file. A manually cropped JPEG image was generated to assist in visual core description. Postprocessing of data included color balance (performed by the Imaging Specialist) and the construction of a composite JPEG image of each core.

## Biostratigraphy

### Paleontology

Paleontological studies were based on semiquantitative analyses of nannofossil and planktonic foraminifer assemblages as well as benthic foraminifer and ostracod associations. In addition, the pollen and microcharcoal particle content in sediment was analyzed and the presence of pteropod shells was noted.

Nannofossil and planktonic foraminifer assemblages can be used as indicators for surface water conditions, like sea-surface temperature and productivity (e.g., Colmenero-Hidalgo et al., 2004; Baumann et

al., 2005; Narciso et al., 2006; Kucera, 2007; Salgueiro et al., 2010), to identify past surface water variations. Aragonitic pteropod shells are preserved in sediments during specific time intervals (Herman, 1971), such as the layer dated at 19.1 calendar k.y. before present in the Gulf of Cádiz (Voelker et al., 2006). Pteropod assemblages are found to be useful for inferring oceanographic circulation and ventilation conditions at intermediate depth. Changes in abundance variation and preservation condition of their assemblages are related to hydrographic parameters like salinity, temperature, and oxygen conditions, as well as the aragonite saturation state of deep water (e.g., Almogi-Labin et al., 1986; Gerhardt et al., 2000; Singh et al., 2005). They are frequent north of the Azores Front (Schiebel et al., 2002), which during the Last Glacial Maximum extended into the Gulf of Cádiz (Rogerson et al., 2004).

By contrast, variations in the benthic foraminifer and ostracod assemblages are very useful as proxies for deepwater circulation since they are very sensitive to bottom water conditions, such as food availability, oxygen content, and other physicochemical properties (e.g., Murray, 2006). In particular, variations in the benthic assemblages along the Iberian continental margin may have been driven by the interplay between surface productivity and changes in the flow intensity of the prevailing deep water (i.e., North Atlantic Deep Water, Antarctic Bottom Water, or Mediterranean Outflow Water) (e.g., Schönfeld and Zahn, 2000).

The information about the composition of the planktonic and benthic foraminifer assemblages will be very useful to plan future stable isotope studies, in particular, to select the most appropriate species based on their occurrence in the different sites.

Pollen and microcharcoal content can be used to explore past changes in vegetation and fire regime and, therefore, in atmospheric circulation, air temperature, and precipitation on the Iberian Peninsula. So far such changes have been reported at orbital and millennial timescales for the last 425 k.y. (e.g., Daniau et al., 2007; Sánchez Goñi et al., 2008; Desprat et al., 2005; Naughton et al., 2009; Margari et al., 2010).

### Biostratigraphy

Preliminary ages were assigned primarily based on core catcher samples. Additional samples taken within the cores were examined when a more refined age determination was required. Calcareous nannofossil and foraminifer age events from the late Miocene to Quaternary were estimated by correlation to the geomagnetic polarity timescale (GPTS) of Lourens et al. (2004). Nannofossil and planktonic

foraminifer events, zones, and subzones are summarized in Figure F11. The following terminology was applied for each group:

- FO = first occurrence.
- LO = last occurrence.
- FcO = first common occurrence.
- LcO = last common occurrence.
- FaO = first abundant occurrence.
- LaO = last abundant occurrence.
- LrO = last regular occurrence.
- T = top.
- B = bottom.
- AB = acme bottom.

The concept of acme (dominance interval) and paracme (absence interval) has been also applied.

The Pliocene/Pleistocene boundary has been formally established at 2.588 Ma at the boundary between the Piacenzian and Gelasian, located just above the Matuyama/Gauss magnetic reversal within marine isotope Stage 103 (Gibbard et al., 2010). The boundary can be approximated by the LO of *Discoaster surculus* (2.53 Ma) and the LO of *Globorotalia puncticulata* (2.41 Ma) (Fig. F11). The Miocene/Pliocene boundary is a remarkable event in the Mediterranean because it marks the Pliocene flooding after the Messinian salinity crisis, astronomically dated at 5.33 Ma (Hilgen, 1991), and the recovery of open-marine deep-sea microfaunas in the Mediterranean basins. However, its identification in the Atlantic is problematic because no major environmental change occurred in this area at that time. The location of this boundary is not well constrained because no bioevent has been identified in this time interval. Nevertheless, the biohorizons of the FO of *Ceratolithus acutus* and the LO of *Discoaster quinqueramus*, occurring at 5.34 and 5.54 Ma, respectively, may be used to approximate the boundary in the Atlantic. These events, however, are not valid for the Mediterranean because of the restricted connection between the Atlantic and the Mediterranean. Details of the shipboard methods are described below for each microfossil group.

### Calcareous nannofossils

Bioevent ages were assigned based on the occurrence of calcareous nannofossils (presence, absence, or dominance) in core catcher samples and in selected sections. The calibration of the identified events was derived mainly from Raffi et al. (2006). Additionally, Martini (1971) and Okada and Bukry (1980) standard zonal schemes were adopted (Fig. F11; Table T2).

The change in abundance of the large *Emiliania huxleyi* (>4  $\mu\text{m}$ ), that characterizes Termination 1 in

mid- to low-latitude water masses in the northeast Atlantic Ocean (Flores et al., 2010), was utilized.

*Gephyrocapsa* species are grouped in several size categories. Specimens <3  $\mu\text{m}$ , mainly *Gephyrocapsa ericsonii* and *Gephyrocapsa aperta*, are classified as “small *Gephyrocapsa*.” Specimens of *Gephyrocapsa muellerae* and *Gephyrocapsa margerelii*, as well as other identified specimens in the 3–5.5  $\mu\text{m}$  size range, are referred to as “medium *Gephyrocapsa*.” The “large *Gephyrocapsa*” category includes forms >5.5  $\mu\text{m}$ . *Gephyrocapsa oceanica* is divided into *G. oceanica* >5  $\mu\text{m}$  and *G. oceanica* <5  $\mu\text{m}$ .

*Reticulofenestra* specimens were also considered following a size concept. *Reticulofenestra pseudumbilicus* is divided into *R. pseudumbilicus* >7  $\mu\text{m}$  and *R. pseudumbilicus* 5–7  $\mu\text{m}$ . *Reticulofenestra haqii* and *Reticulofenestra minutula* are considered “medium *Reticulofenestra*,” ranging between 3 and 5  $\mu\text{m}$ . Forms <3  $\mu\text{m}$  are “small *Reticulofenestra*,” mainly corresponding to *Reticulofenestra minuta*. *Reticulofenestra asanoi* is divided into *R. asanoi* >6  $\mu\text{m}$  and *R. asanoi* <6  $\mu\text{m}$ .

Morphometric subdivision within *Calcidiscus leptoporus* s.l. and *Coccolithus pelagicus* s.l. complexes are used according to the taxonomy of Klejine (1993), Knappertsbusch et al. (1997), Steel (2001), Geisen et al. (2002), Quinn et al. (2003, 2004), and Parente et al. (2004).

Otherwise, taxonomic concepts for Neogene taxa were adopted from Perch-Nielsen (1985).

The magnetostratigraphy for the Cenozoic is based on Lourens et al. (2004).

### Foraminifers

Preliminary ages were assigned based on the occurrence of planktonic foraminifers (presence, absence, and acme) in core catcher samples. Biostratigraphic events were derived mainly from Lourens et al. (2004). Additional datums are adopted from Weaver and Clement (1987), Chaisson and Pearson (1997), Krijgsman et al. (2004), Berggren et al. (1995), Hilgen (1991), Serrano et al. (1999), and Sierro (unpubl. data) (Fig. F11; Table T3). We use bioevent names as reported by the previous authors.

*Globorotalia conomiozea* and *Globorotalia miotumida* are grouped together under the name of the *G. miotumida* group. In the Miocene, the *Globorotalia menardii* group also includes *Globorotalia plesiotumida* and *Globorotalia merotumida* following Sierro et al. (1993). *Globorotalia crassaformis* comprises the two subspecies *G. crassaformis hessi* and *G. crassaformis ronda*. *Globigerinoides extremus* includes *Globigerinoides obliquus* because it is difficult to distinguish these two species in Pliocene sediments from the Atlantic and Mediterranean regions. *Globigerinella calida* and

*Globogerinella obesa* are grouped as well. For abundance estimates, *Neogloboquadrina acostaensis* is combined with *Neogloboquadrina pachyderma*, and the nomenclature of *N. pachyderma* (dextral) instead of *Neogloboquadrina incompta* is applied.

Otherwise, taxonomic concepts for Neogene taxa are adopted from Kennett and Srinivasan (1983).

Ages for the magnetic polarity reversals are based on Lourens et al. (2004).

Benthic foraminifers provide limited biostratigraphic age control. Whenever possible, the “*Stilostomella* extinction” was recorded, during which a high number of deep-sea foraminifer species of *Stilostomellidae*, *Pleurostomellidae*, and *Nodosariidae* disappeared from the global ocean. Previous studies demonstrate that a pulsed decline in these foraminiferal groups starts at ~1.2 Ma, and that the final *Stilostomella* extinction datum occurs globally between 0.7 and 0.58 Ma (e.g., Hayward, 2002; Kawagata et al., 2005).

## Paleoceanography

### Benthic foraminifers

Benthic foraminifers from core catcher samples were primarily used to determine past changes in oceanographic conditions (Murray, 2006). To record changes in current velocity, the abundance of suspension-feeding benthic foraminifers was evaluated (“epibenthos group”; Schönfeld, 1997, 2002; Schönfeld and Zahn, 2000). Taxonomic assignments on the generic level follow Loeblich and Tappan (1988) with updates from Hayward (2002).

### Ostracods

Ostracods are small bivalved crustaceans that are commonly preserved as fossils in the ocean floor at depths shallower than the calcium carbonate compensation depth (CCD) and lysocline. Like benthic foraminifers, ostracods are used to reconstruct past environmental and oceanographic conditions because their distribution is controlled by physical and chemical characteristics of bottom water (Dingle and Lord, 1990; Corrège, 1993; Ayress et al., 1997; Cronin et al., 1999; Alvarez Zarikian et al., 2009; Yasuhara et al., 2009a). During Expedition 339, ostracods were studied from most sites and were identified using taxonomic assignments by Whatley and Coles (1987), Coles and Whatley (1989), Alvarez Zarikian (2009), and Yasuhara et al. (2009b).

## Sample preparation methods

### Calcareous nannofossils

Samples were prepared following the standard smear slide technique with Norland optical adhesive. Cal-

careous nannofossils were examined with a Zeiss polarized microscope at 1000× magnification.

Preservation includes effects of dissolution and overgrowth. Preservation of calcareous nannofossils was categorized as

G = good (little or no evidence of dissolution and/or overgrowth; specimens are identifiable to the species level).

M = moderate (minor to moderate dissolution and/or overgrowth; most specimens are identifiable to the species level).

P = poor (extreme dissolution and overgrowth).

Total abundance of calcareous nannofossils was categorized as

VA = very abundant (>100 specimens per field of view).

A = abundant (11–100 specimens per field of view).

C = common (1–10 specimens per field of view).

F = few (1 specimen per 2–10 fields of view).

R = rare (1 specimen per ≥11 fields of view).

B = barren.

Abundances of individual taxa or groups of calcareous nannofossils were categorized as

D = dominant (>20 specimens per field of view).

A = abundant (11–20 specimens per field of view).

C = common (1–10 specimens per field of view).

F = few (1 specimen per 2–10 fields of view).

R = rare (1 specimen per ≥11 fields of view).

P = present (abundance not quantitatively determined).

### Foraminifers and ostracods

From each core catcher, 20–30 cm<sup>3</sup> of sediment was analyzed for planktonic and benthic foraminifers and ostracods. Unlithified sediment samples were soaked in tap water and washed over a 63 μm sieve. Semilithified material was soaked in a 3% H<sub>2</sub>O<sub>2</sub> solution for a few minutes before washing. In addition, mudline samples were taken from most holes and analyzed for benthic foraminifers and ostracods. Mudline samples were collected by emptying the sediment/water material from the top core liner of each hole into a bucket. Tests using Rose Bengal staining confirmed the presence of some living ostracods and benthic foraminifers in the mudline samples. Washed samples were dried at 60°C. The dried residue (>63 μm size fraction) was split for planktonic (25%) and benthic foraminifer (75%) assemblage studies. The samples were analyzed under a ZEISS Discovery V8 and ZEISS Stemi SV11 stereomicroscope, respectively. In order to avoid contamination between successive samples, sieves used for wet sieving were cleaned in an ultrasonic bath for several

minutes, and those used for dry sieving were cleaned with compressed air.

Planktonic foraminiferal abundance in the >150  $\mu\text{m}$  fraction in relation to the total residue of each sample was categorized as

- D = dominant (>30%).
- A = abundant (>10%–30%).
- F = few (>5%–10%).
- R = rare (1%–5%).
- P = present (<1%).
- B = barren.

Benthic foraminiferal abundance in samples of the >63  $\mu\text{m}$  size fraction is registered as

- D = dominant (>30%).
- A = abundant (>10%–30%).
- F = few (>5%–10%).
- R = rare (1%–5%).
- P = present (<1%).
- B = barren.

Ostracods were examined from the >150  $\mu\text{m}$  fraction of each sample, and their abundance in relation to the total residue was recorded as

- A = abundant (40 or more per sample).
- C = common (15–39 per sample).
- R = rare (1–14 per sample).
- B = barren.

Relative abundance was characterized as

- D = dominant (>30%).
- A = abundant (>10%–30%).
- F = few (>5%–10%).
- R = rare (1%–5%).
- P = present (<1%).

Pteropod abundance in the >150  $\mu\text{m}$  fraction in relation to the total residue of each sample was categorized as

- C = common (>5 specimens).
- R = rare (1–5 specimens).
- B = barren.

Preservation includes the effects of diagenesis, epigenesis, abrasion, encrustation, and/or dissolution. Preservation of planktonic and benthic foraminifers and ostracods was categorized as

- VG = very good (no evidence of breakage or dissolution).
- G = good (only very minor dissolution and no recrystallization; <10% of specimens are broken).
- M = moderate (frequent etching and partial breakage; 30%–90% of specimens are unbroken).
- P = poor (much dissolution and recrystallization; broken specimens dominate).

## Palynology

### Pollen, microcharcoals, dinoflagellate cysts, and other palynomorphs

Palynological sample preparations yielded several types of organic-walled microfossils (i.e., palynomorphs) that include mainly dinoflagellate cysts (dinocysts), pollen, microcharcoal particles, spores from terrestrial plants, and organic linings of foraminifers. During Expedition 339, all palynomorphs were investigated with primary focus on pollen grains as paleoecological, paleoclimatic, and rough biostratigraphic indicators. A number of studies have documented the most abundant pollen morphotypes in northwestern and central Europe for the Miocene, Pliocene, Pleistocene, and Holocene (Traverse, 1988), in the Mediterranean region for Pliocene–Pleistocene (Suc, 1984), and, more recently, from the Iberian Peninsula for the Miocene–Pliocene (Jiménez-Moreno et al., 2010) and the Mid-Pleistocene Transition (MPT), from ~1 to 0.8 Ma (Joannin et al., 2011). The Pliocene vegetation of the southwestern part of this region, the area addressed by this expedition, was dominated by *Cathaya*, *Engelhardtia*, *Sequoia*, *Myrica*, and *Taxodium*; Ericaceae and Mediterranean xerophytes such as *Olea*, *Phillyrea*, *Cistus*, Rhamnaceae, and evergreen *Quercus* were also significantly represented. During the MPT, the most common taxa were deciduous *Quercus*, Ericaceae, and high- and mid-altitude conifers such as *Cedrus*, *Abies*, *Tsuga*, and *Picea*. Additionally, many studies (e.g., Lézine and Denèfle, 1997; Sánchez Goñi et al., 1999, 2000, 2008, 2009; Fletcher et al., 2007; Roucoux et al., 2006; Margari et al., 2010) have documented the most frequent pollen morphotypes from the late mid-Pleistocene (~0.425 Ma) to the Holocene in this region. On the basis of these studies, the analysis of the pollen content may allow us to roughly assign sediment to one of these epochs. However, the distinction between mid-Pleistocene, late Pleistocene, and Holocene will remain problematic, as the same Mediterranean and semidesert pollen morphotypes (deciduous and evergreen *Quercus*, *Artemisia*, Chenopodiaceae, and *Ephedra*) are common during these time intervals (Table T4).

### Sample preparation methods

Approximately 1–3  $\text{cm}^3$  of sample was processed using a simplified palynologic treatment, avoiding HF treatments. The procedures included sieving through 100  $\mu\text{m}$  mesh to discard coarse material. The fraction <100  $\mu\text{m}$  was treated first with cold and then with warm HCl (30%) to remove carbonates. The residue was sieved again through a 10  $\mu\text{m}$  mesh using a magnetic agitator plate to eliminate clay and fine silt particles. To concentrate palynomorphs, quartz particles

were eliminated by applying the watch-glass procedure. The final residue was mounted between slides and coverslips with bi-distilled glycerine. Tablets of *Lycopodium* spores with known concentration (20,848 spores/tablet), referred to as exotics in the table, were included in the sample at the beginning of the preparation to allow a concentration calculation.

The slides were examined on a Zeiss Axioplan microscope with magnification ranging from 200× to 500×. Taxonomic identifications were verified at 1000× magnification.

Abundances are reported as

- A = abundant (>2000/cm<sup>3</sup>).
- C = common (500–2000/cm<sup>3</sup>).
- F = few (100–500/cm<sup>3</sup>).
- R = rare (<100/cm<sup>3</sup>).

Special attention was given to pollen, grains of which were counted and identified to the genus or type within genus level when possible.

Preservation of pollen grains, and palynomorphs in general, was determined qualitatively and reported as

- G = good (no trace of alteration of the organic walls; pollen and dinocysts are spherical; occurrence of the least resistant taxa).
- M = moderate (subtle indication of alteration; flattening of palynomorphs; specimen occasionally broken).
- P = poor (only most resistant palynomorph present, showing strong alteration features and flattening; specimens often broken).

## Paleomagnetism

### Samples, instruments, and measurements

Paleomagnetic studies during Expedition 339 focused mainly on measuring the natural remanent magnetization (NRM) of archive-half sections before and after alternating field (AF) demagnetization. We typically collected one discrete sample per section from working-half sections for use in full AF demagnetization experiments. Discrete samples were taken from the first deep hole cored at a site (typically Hole A) and from the rotary-drilled holes that recovered the deeper parts of the cored sections. The samples were collected by inserting a hollow extruder into the middle of the split-core sections and then extruding the sediments into plastic cubes (2 cm × 2 cm × 2 cm, with an internal volume of ~7 cm<sup>3</sup>) as described in Richter et al. (2007).

All remanence measurements were made using a 2G Enterprises Model-760R superconducting rock magnetometer (SRM) equipped with direct-current super-

conducting quantum interference devices (DC-SQUIDS) and an in-line, automated AF demagnetizer capable of reaching a peak field of 80 mT. The spatial resolution measured by the width at half-height of the pickup coils response is <10 cm for all three axes, although they sense a magnetization over a core length up to 30 cm. The magnetic moment noise level of the cryogenic magnetometer is ~2 × 10<sup>-10</sup> Am<sup>2</sup>. The practical noise level, however, is affected by the magnetization of the core liner and the background magnetization of the measurement tray, resulting in magnetizations of ~2 × 10<sup>-5</sup> A/m that can be reliably measured.

NRM measurements of the archive-half core sections were made at 5 cm interval resolution along the split-core sections, as well as over a 15 cm interval before the sample passed the center of the pick-up coils of the SQUID sensors and a 15 cm interval after the samples had passed through it. These are referred to as the leader and trailer measurements and serve the dual function of monitoring the background magnetic moment and allowing for future deconvolution analysis. Typically, we measured NRM before any demagnetization and after a 20 mT peak field AF demagnetization. In a few instances, when time permitted, we also measured the NRM after a 10 mT AF demagnetization step. Because core flow (the analysis of one core after the other) through the laboratory dictates the available time for measurements, which was ~2–3 h per core for Expedition 339, we did not always have time for the optimal number of demagnetization steps.

During Expedition 339, a number of discrete samples, selected to characterize typical intervals or to help determine poorly resolved magnetostratigraphy, were subjected to progressive AF demagnetization and measured at 5 mT steps to a peak field of 60 mT and then 10 mT steps to 80 mT. This was done to determine whether a characteristic remanent magnetization (ChRM) could be resolved and, if so, what level of demagnetization was required to resolve it.

Low-field magnetic susceptibility was measured on whole-core sections using the Special Task Multisensor Logger (STMSL) and WRMSL, and on archive-half core sections using the SHMSL (see “[Physical properties](#)” and “[Stratigraphic correlation](#)”). The WRMSL and STMSL are equipped with a Bartington Instruments MS2C sensor with an internal diameter of 80 mm, which corresponds to a coil diameter of 88 mm. The sensor has a nominal resolution of ~2 × 10<sup>-6</sup> SI (Blum, 1997). The “units” option for the meters was set on SI units, and the values were stored in the database in raw meter units. To convert to true SI volume susceptibilities, these raw units should be multiplied by ~0.68 × 10<sup>-5</sup> (Blum, 1997). The SHMSL

is equipped with a Bartington Instruments MS2E point sensor that measures the susceptibility of an integrated volume of approximately 10.5 mm × 3.8 mm × 4 mm, where 10.5 mm is the length perpendicular to the core axis, 3.8 mm is the width in the core axis, and 4 mm is the depth. Magnetic susceptibility is typically measured every 2.5 cm for the whole-core sections and every 2–5 cm for the split-core sections.

### Coring and core orientation

Cores were collected using nonmagnetic core barrels, except at depths where overpull tension was large enough to cause damage to the more expensive nonmagnetic core barrel. In addition, the BHA included a Monel (nonmagnetic) drill collar when the FlexIt core orientation tool was used. The FlexIt tool uses three orthogonally mounted fluxgate magnetometers to record the orientation of the double lines scribed on the core liner with respect to magnetic north. The tool also has three orthogonally mounted accelerometers to monitor the movement of the drill assembly and help determine when the most stable, and thus useful, core orientation data were gathered. The tool declination, inclination, total magnetic field, and temperature are recorded internally at regular intervals until the tool's memory capacity is filled. For a measurement interval of 6 s, which is what we used, the tool can typically be run for ~24 h, although we aimed to switch tools at least every 8–12 h.

Standard operating procedure for the FlexIt tool is described in the IODP “Core Orientation Standard Operating Procedure” manual (available from the IODP Cumulus database ([iodp.tamu.edu/tasapps/](http://iodp.tamu.edu/tasapps/))). This involves synchronizing the instrument to a PC running the FlexIt software and inserting the tool inside a pressure casing. The enclosed tool is then installed on the sinker bars that reside above the core barrel. The double lines on the core liner are aligned relative to the tool. Prior to firing the APC, the core barrel is held stationary (along with the pipe and BHA) for several minutes. During this time, the data recorded are those used to constrain the core orientation. When the APC fires, the core barrel is assumed to maintain the same orientation, although this and past expeditions have found evidence that the core barrel can rotate and/or the core liner can twist as it penetrates the sediments. Generally, the core barrel is pulled out after a few minutes except for cores collected with the advanced piston corer temperature tool (APCT-3) (see “[Downhole measurements](#)”), for which the core barrel remains in the sediments for ≥10 min.

### Magnetostratigraphy

Magnetic polarity zones (magnetozones) were assigned based on changes in inclinations, as well as distinct ~180° alternations in declination that occur along each stratigraphic section. Inclination and declination of NRM after 20 mT peak field AF demagnetization were used for the determination of magnetozones during Expedition 339. For cores with FlexIt tool data, declinations were first corrected for core orientation. Magnetostratigraphy for each site was then constructed by correlating the magnetozones with the GPTS. Biostratigraphic age constraints significantly limit the range of possible correlations of the magnetozones with the GPTS. The GPTS used during Expedition 339 is based upon the Neogene timescale of Lourens et al. (2004).

### Physical properties

High-resolution physical property measurements were made during Expedition 339 mainly to aid lithostratigraphic correlation and for tying borehole data to seismic profiles. In more detail, physical property data plays a major role in the following tasks:

- Hole-to-hole and site-to-site stratigraphic correlation for construction of composite stratigraphic sections;
- Detection of discontinuities and lateral inhomogeneities, either caused naturally or by the drilling process;
- Obtaining information about differences in the composition and texture of sediment, especially regarding the distinction between contourite and turbidite deposits;
- Detection of orbital cycles and tuning to reference cores for stratigraphic purposes; and
- Identification of major seismic reflectors and construction of synthetic seismic profiles.

First, physical properties were measured on whole-round core sections. Core sections are generally 1.5 m in length, so a typical coring length (stroke) of 9.5 m yields six sections plus a shorter seventh section. Two core logging systems were run on each section: (1) the STMSL was run on sections immediately after they were sectioned on the catwalk and (2) the WRMSL was run on core sections that had warmed to ambient laboratory temperature (20°–21°C). The linear track of the STMSL houses a gamma ray attenuation (GRA) bulk densitometer and a magnetic susceptibility sensor loop. The WRMSL employs, in order, a GRA bulk densitometer, a magnetic susceptibility sensor loop, and a compressional *P*-wave velocity sensor.

After WRMSL scanning, the whole-round sections were logged for NGR. Thermal conductivity was then measured on certain whole-round sections (Section 3 of each core in one hole per site, usually Hole A) by a needle probe inserted into the section through a small hole drilled through the plastic core liner close to the middle of the section.

At this phase, the sections were split into working and archive halves. Discrete samples were collected from the working halves of every second section to measure wet bulk density, dry bulk density, water content, porosity, and grain density with moisture and density (MAD) procedures. Compressional  $P$ -wave velocity measurements on split cores were made for every section for one hole (usually Hole A), employing the transducers oriented in  $x$ -axis direction. Archive halves were documented by the SHIL and analyzed with the SHMSL for color reflectance and magnetic susceptibility. A full discussion of all methodologies and calculations used aboard the *JOIDES Resolution* in the Physical Properties Laboratory is available in Blum (1997).

### Special Task Multisensor Logger

The purpose of STMSL logging operations during Expedition 339 was to rapidly record medium- to high-resolution sets of GRA and magnetic susceptibility data. This information was needed at multihole sites to ensure that drilling depth offsets were set at different stratigraphic depths in each hole so that a complete composite stratigraphic section could be constructed. The GRA bulk densitometer and magnetic susceptibility loop incorporated in the STMSL are effectively identical to those in the WRMSL (see below). The spacing distance between STMSL measurements was typically 2.5 cm for GRA density and magnetic susceptibility measurements. Scanning time averaged 8 s per sample with one repeat for the magnetic susceptibility measurements. A core can therefore be passed in ~25 min through the STMSL. Comments about structural integrity and incomplete filling of liners were recorded.

### Whole-Round Multisensor Logger

High-resolution WRMSL data, especially GRA bulk density and magnetic susceptibility, were gathered to advance shipboard core-to-core correlation between drill holes and the construction of composite stratigraphic sections. WRMSL data assembly had to be completed within a reasonable time to not encumber downstream core processing and sample collection. The quality of WRMSL data is highly dependent on the structural integrity of the sediment (cracks, voids, biscuiting, etc.) and whether any gaps between the sediment and the core liner are present.

GRA bulk density and magnetic susceptibility were measured nondestructively on all whole-round core sections.  $P$ -wave velocity was measured in sections undisturbed by gas expansion voids and cracks. To optimize WRMSL performance, the same sampling spacing, typically 2.5 cm, was set for all sensors. Measurement time, although somewhat different for the different sensors, averaged ~8 s per data, with one repeat of the magnetic susceptibility providing sufficient reproducibility. With handling and data initializing, a 1.5 m section took ~10 min to scan. A 9.5 m core therefore took ~1 h to pass through the WRMSL.

### Gamma ray attenuation bulk density

Bulk density is a reflection of water-saturated porosity, grain density (dominant mineralogy), grain packing, and coring disturbance. To measure bulk density, the GRA densitometer uses a 10 mCi  $^{137}\text{Cs}$  capsule as a gamma ray source (with the principal energy peak at 0.662 MeV) and a scintillation detector. The narrow collimated peak is attenuated as it passes through the center of the core. Incident photons are scattered by the electrons of the sediment by Compton scattering.

The attenuation of the incident intensity ( $I_0$ ) is directly related to the electron density in the sediment core of diameter  $D$  that can be related to bulk density given the average attenuation coefficient (in micrometers) of the sediment (Evans, 1965; Harms and Choquette, 1965). Because the attenuation coefficient is similar for most common minerals and aluminum, bulk density is obtained through direct calibration of the densitometer using aluminum rods of different diameters mounted in a core liner filled with distilled water. The GRA densitometer has a spatial resolution of <1 cm.

### Magnetic susceptibility

Magnetic susceptibility is a measure of the degree to which a material can be magnetized by an external magnetic field. It provides information on the magnetic composition of the sediment that commonly can be related to mineralogical composition (e.g., terrigenous versus biogenic materials) and diagenetic overprinting. Magnetite and a few other iron oxides with ferromagnetic characteristics have a specific magnetic susceptibility several orders of magnitude higher than clay, which has paramagnetic properties. Carbonate layers, opal, water, and plastic (core liner) have small negative values of magnetic susceptibility. Calcareous and biogenic deposits with low clay and iron-bearing mineral debris content thus have values approaching the detection limit of magnetic susceptibility meters.

Magnetic susceptibility was measured on the WRMSL and STMSL with the Bartington Instruments MS2C system. The frequency at which the magnetic susceptibility loop operates is 565 Hz for the WRMSL and STMSL (Blum, 1997). The output of the magnetic susceptibility sensors can be set to centimeter-gram-second (cgs) units or SI units, the IODP standard. However, to obtain dimensionless SI volume-specific magnetic susceptibility values, the instrument units stored in the IODP database must be multiplied by a correction factor (0.68) to compensate for instrument scaling and the geometric ratio between core and loop dimensions.

### Compressional *P*-wave velocity

*P*-wave velocity varies with the material's lithology, porosity, and bulk density, as well as state of stress, temperature, and fabric or degree of fracturing. In sediment and rock, velocity is controlled by the degree of consolidation and lithification, fracturing, and occurrence and abundance of free gas and gas hydrate. Together with bulk density, velocity data are used to calculate acoustic impedance and reflection coefficients in order to construct synthetic seismic profiles and to estimate the depth of specific seismic horizons.

The *P*-wave velocity sensor measures the ultrasonic *P*-wave velocity of the whole-round sample residing in the core liner. The *P*-wave logger transmits a 500 kHz *P*-wave pulse across the core section at a specified repetition rate.

Traveltime is determined by signal processing software that automatically detects the first arrival of the *P*-wave signal to a precision of 50 ns. Ultrasonic *P*-wave velocity is calculated after correcting for system propagation delay, liner thickness, and liner material velocity.

### Natural Gamma Radiation Logger

The NGRL was designed and built at the Texas A&M University IODP-USIO facility and measures gamma rays emitted from whole-round core sections. Gamma rays detected by the logger arise primarily from the decay of mineral-hosted uranium, thorium, and potassium isotopes. In general, high counts identify fine-grained deposits containing K-rich clay minerals and their absorbed U and Th atoms. The NGR data reveals stratigraphic details that aid in core-to-core correlations.

The main NGR detector unit consists of 8 sodium iodide (NaI) scintillator detectors surrounding the lower half of the section, 7 shielding plastic scintillator detectors, 22 photomultipliers, and passive lead shielding. The NaI detectors are covered by at least 8

cm of lead shielding. In addition, lead separators (~7 cm of low-background lead) are positioned between the NaI detectors. Half of the lead shielding closest to the NaI detectors is composed of low-background lead, whereas the outer half is composed of common (virgin) lead. In addition to this passive lead shielding, the overlying plastic scintillators detect incoming high-energy gamma and muon cosmic radiation and cancel this signal from the total counted by the NaI detectors.

A measurement run generally consisted of counting one position on each core section for 7 min for a total of 8 measurements per 150 cm section. For analyses, "Position 2" was commonly chosen to avoid analyzing the disturbed uppermost part of the first section of each core. Therefore, NGR logging required ~50 min measurement time and another ~10 min for core, software, and data handling. In some cases, when time permitted, the two-position configuration (10 cm spacing) was chosen, doubling measurement time.

### Thermal conductivity

After NGR measurements were completed, thermal conductivity was measured with the TK04 (Teka Bollen) system using the needle-probe method in full-space configuration for whole-round sediment cores (Von Herzen and Maxwell, 1959). The needle probe contains a heater wire and calibrated thermistor. The probe was inserted into a 2 mm hole drilled through the liner along one of the lines that later guided the splitting of the core. To avoid interference from airflow in the laboratory, an insulating jacket of foam rubber was placed over the core section during measurement of thermal conductivity.

Because the probe is much more conductive than unconsolidated sediment, the probe is assumed to be a perfect conductor. Under this assumption, the temperature of the superconductive probe has a linear relationship with the natural logarithm of the time after the initiation of the heat:

$$T(t) = (q/4\pi k) \times \ln(t) + C,$$

where

- $T$  = temperature (K),
- $q$  = heat input per unit length per unit time (J/m/s),
- $k$  = thermal conductivity (W/[m·K]),
- $t$  = time after the initiation of the heat (s), and
- $C$  = instrumental constant.

Three measuring cycles were automatically performed at each probe location to calculate average conductivity. A self-test, which included a drift study, was conducted at the beginning of each mea-

surement cycle. Once the probe temperature stabilized, the heater circuit was closed and the temperature rise in the probe was recorded. Thermal conductivity was calculated from the rate of temperature rise while the heater current was flowing. Temperatures measured during the first 150 s of the heating cycle were fitted to an approximate solution of a constantly heated line source (for details, see Kristiansen, 1982; Blum, 1997). Measurement errors were 5%–10%. Thermal conductivity measurements were routinely taken in one hole per site and in one section per core, typically Section 3. Cores retrieved by XCB and RCB usually yielded no results for thermal conductivity measurements because cracks in the sediment caused bad coupling of the probe to the sediment. In these cases the self-test during the measurement procedure failed and no results were reported to the data base.

### Moisture and density

After the completion of thermal conductivity measurements, whole-round cores were split into working and archive halves. The working halves were placed on the sampling table for the collection of discrete samples to determine wet and dry bulk density, grain density, water content, and porosity. In soft sediment, ~10 cm<sup>3</sup> samples were collected with a plastic syringe, the diameter of which fit that of the glass vial. An attempt was made to sample every other section per core at the 59–60 cm position. Samples were placed in numbered, preweighed 16 mL Wheaton glass vials for wet and dry sediment weighing, drying, and wet and dry volume measurements. The weights of wet and dry sample masses were determined to a precision of 0.005 g using two Mettler Toledo electronic balances and a computer averaging system to compensate for the ship's motion.

Dry sample volume was determined using a hexapycnometer system of a six-celled, custom-configured Micromeritics AccuPyc 1330TC helium-displacement pycnometer. The precision of each cell is 1% of the full-scale volume. Volume measurement was preceded by three purges of the sample chamber with helium warmed to ~28°C. Three measurement cycles were run for each sample. A reference volume (calibration sphere) was placed sequentially in one of the chambers to check for instrument drift and systematic error. The volumes of the numbered Wheaton vials were calculated before the cruise by multiplying each vial's weight against the average density of the vial glass. Dry mass and volume were measured after samples were heated in an oven at 105° ± 5°C for 24 h and allowed to cool in a desiccator. The procedures for the determination of these physical

properties comply with the American Society for Testing and Materials (ASTM) designation (D) 2216 (ASTM International, 1990). The fundamental relation and assumptions for the calculations of all physical property parameters are discussed by Blum (1997) and summarized below.

### Mass and volume calculation

Wet mass ( $M_{\text{wet}}$ ), dry mass ( $M_{\text{dry}}$ ), and dry volume ( $V_{\text{dry}}$ ) were measured in the laboratory. The ratio of mass (rm) is a computational constant of 0.965 (i.e., 0.965 g of freshwater per 1 g of seawater). Salt precipitated in sediment pores during the drying process is included in the  $M_{\text{dry}}$  and  $V_{\text{dry}}$  values. The mass of the evaporated water ( $M_{\text{water}}$ ) and salt ( $M_{\text{salt}}$ ) in the sample are given by, respectively,

$$M_{\text{water}} = M_{\text{wet}} - M_{\text{dry}} \text{ and}$$

$$M_{\text{salt}} = M_{\text{water}}[s/(1 - s)],$$

where  $s$  is the assumed saltwater salinity (0.035%) corresponding to a pore water density ( $\rho_{\text{pw}}$ ) of 1.024 g/cm<sup>3</sup> and a salt density ( $\rho_{\text{salt}}$ ) of 2.22 g/cm<sup>3</sup>. The corrected mass of pore water ( $M_{\text{pw}}$ ), volume of pore water ( $V_{\text{pw}}$ ), mass of solids excluding salt ( $M_{\text{solid}}$ ), volume of salt ( $V_{\text{salt}}$ ), volume of solids excluding salt ( $V_{\text{solid}}$ ), and wet volume ( $V_{\text{wet}}$ ) are, respectively,

$$M_{\text{pw}} = (M_{\text{wet}} - M_{\text{dry}})/\text{rm},$$

$$V_{\text{pw}} = M_{\text{pw}}/\rho_{\text{pw}}$$

$$M_{\text{solid}} = M_{\text{wet}} - M_{\text{pw}}$$

$$M_{\text{salt}} = M_{\text{pw}} - (M_{\text{wet}} - M_{\text{dry}}),$$

$$V_{\text{salt}} = M_{\text{salt}}/\rho_{\text{salt}},$$

$$V_{\text{wet}} = V_{\text{dry}} - V_{\text{salt}} + V_{\text{pw}} \text{ and}$$

$$V_{\text{solid}} = V_{\text{wet}} - V_{\text{pw}}$$

### Calculation of bulk properties

For all sediment samples, water content ( $w$ ) is expressed as the ratio of mass of pore water to wet sediment (total) mass,

$$w = M_{\text{pw}}/M_{\text{wet}}.$$

Wet bulk density ( $\rho_{\text{wet}}$ ), dry bulk density ( $\rho_{\text{dry}}$ ), sediment grain density ( $\rho_{\text{solid}}$ ), porosity ( $\phi$ ), and void ratio (VR) are calculated as

$$\rho_{\text{wet}} = M_{\text{wet}}/V_{\text{wet}}$$

$$\rho_{\text{dry}} = M_{\text{solid}}/V_{\text{wet}}$$

$$\rho_{\text{solid}} = M_{\text{solid}}/V_{\text{solid}}$$

$$\rho = V_{\text{pw}}/V_{\text{wet}} \text{ and}$$

$$\text{VR} = V_{\text{pw}}/V_{\text{solid}}$$

Moisture and density properties reported and plotted in the “Physical properties” sections of all site chapters were calculated with the MADMax shipboard program.

### Section Half Measurement Gantry

*P*-wave velocity measurements on split cores were performed by using the *x*-axis caliper-type contact probe transducers on the Section Half Measurement Gantry with one analysis per section, usually in Hole A. Measurements were usually taken at ~75 cm section depth; however, if this interval provided no good sediment/transducer coupling (e.g., caused by high amounts of sand or cracks), different positions were chosen to generate viable data. Cores drilled with XCB or RCB generally did not provide usable data because of bad sediment/liner contact and disturbed sediments. In some cases in which sediment was sufficiently indurated, *P*-wave measurements were carried out on discrete pieces taken from the liner.

The system uses Panametrics-NDT Microscan delay line transducers, which transmit at 0.5 MHz. The signal received through the sample was recorded by the computer attached to the system, and the peak (*P*-wave arrival) was chosen with autopicking software. In case of a weak signal, the first arrival was manually picked. The distance between transducers was measured with a built-in linear voltage displacement transformer (LDVT).

Calibration was performed with a series of acrylic cylinders of differing thicknesses and a known *P*-wave velocity of  $2750 \pm 20$  m/s. The determined system time delay from calibration was subtracted from the picked arrival time to give a traveltime of the *P*-wave through the sample. The thickness of the sample (calculated by LDVT in meters) was divided by the traveltime (in seconds) to calculate *P*-wave velocity in meters per second.

### Section Half Multisensor Logger

Spectrophotometry and magnetic susceptibility of the archive halves were measured with the SHMSL. The SHMSL also takes measurements on empty intervals and in places where the core surface is well below the level of the core liner. Spurious measure-

ments can also result from small cracks, sediment disturbance caused by the drilling process, or plastic section dividers. This data should be edited out of the data set by the user. Additional detailed information about measurement and interpretation of spectral data can be found in Balsam et al. (1997, 1998) and Balsam and Damuth (2000).

### Spectrophotometry

Reflectance of visible light from the archive halves of sediment cores was measured using an Ocean Optics USB4000 spectrophotometer mounted on the automated SHMSL. Freshly split soft cores were covered with clear plastic wrap and placed on the SHMSL. Measurements were taken at 2–5 cm spacing to provide a high-resolution stratigraphic record of color variations for visible wavelengths. Each measurement was recorded in 2 nm wide spectral bands from 400 to 900 nm.

### Magnetic susceptibility

Magnetic susceptibility was measured with a Bartington Instruments MS2E point sensor (high-resolution surface scanning sensor) on the SHMSL. Because the SHMSL demands flush contact between the magnetic susceptibility point sensor and the split core, measurements were made on the archive halves of split cores that were covered with clear plastic wrap. Measurements were taken at 2–5 cm spacing and integrate a volume of 10.5 mm × 3.8 mm × 4 mm, where 10.5 mm is the length perpendicular to the core axis, 3.8 mm is the width in the core axis, and 4 mm is the depth. For conversion of the instrument units stored in the IODP database, a correction factor (67/80) must be employed to correct for the relation of the sensor diameter and sediment thickness.

## Geochemistry

The shipboard geochemistry program for Expedition 339 included characterization of (1) volatile gases, (2) interstitial water composition, and (3) sedimentary inorganic geochemistry including inorganic carbon, sedimentary organic carbon, and C/N ratios. These analyses were carried out to satisfy routine shipboard safety and pollution prevention requirements, to characterize interstitial waters and sediment geochemistry for shipboard interpretation, and to provide samples for shore-based research. Non-standard sampling and analyses were also carried out to address some of the specific research goals of this expedition, namely high-resolution sampling and analysis of interstitial water for stable isotopes and chlorinity.

## Sediment gases sampling and analysis

The organic geochemistry program monitored the compositions and concentrations of volatile hydrocarbons ( $C_1$ – $C_6$ ) and other gases in the sediments from headspace gas samples at intervals of typically one per core. The routine headspace procedure involved placing  $\sim 5$  cm<sup>3</sup> of sediment sample in a 21.5 cm<sup>3</sup> glass serum vial that was sealed with a septum and metal crimp cap and heated at 70°C for 30 min. After heating, a 5 cm<sup>3</sup> volume of gas from the headspace in the vial was removed with a glass syringe for analysis by gas chromatography. A second gas sampling procedure was used for gas pockets or expansion voids that appeared in the core while it was still in the core liner. A device with a heavy-duty needle was used to penetrate the core liner, and an attached syringe was employed to collect the gas.

Headspace gas samples were analyzed using an Agilent 6890 gas chromatograph equipped with a 2.4 m  $\times$  3.2 mm stainless steel column packed with 80/100 mesh HayeSep R and a flame ionization detector. The instrument quickly measures concentrations of methane ( $C_1$ ), ethane ( $C_2$ ), ethene ( $C_{2=}$ ), propane ( $C_3$ ), and propene ( $C_{3=}$ ). The gas syringe was directly connected to the gas chromatograph through a 1 cm<sup>3</sup> sample loop. Helium was used as the carrier gas, and the gas chromatograph oven temperature was programmed to start with an oven temperature of 80°C held for 8.25 min before ramping at 40°C/min to 150°C, with a final holding time of 5 min. Data were collected and evaluated with an Agilent Chemstation data-handling program. Chromatographic response was calibrated against known standards.

## Interstitial water sampling

Routine interstitial water was extracted from 5–15 cm long whole-round sediment sections that were cut and capped immediately after core retrieval on deck. Standard whole rounds are 5 cm long, but as porosity decreased downhole, the size of the whole-round sections was increased to enable extraction of the needed  $\sim 30$  mL of water to split between shipboard and shore-based analyses. Samples were taken from near the bottom of each core for the upper 150 m and at intervals of every third core thereafter to total depth, with modifications as indicated (see “Geochemistry” in each site chapter). Samples from more than one hole were treated as constituting a single depth profile (“splice”) using CSF-A as the depth reference if possible.

High-resolution interstitial water sampling was done at Sites U1385, U1386, U1389, and U1391. For high-resolution interstitial water sampling, small plugs of sediment ( $\sim 10$  cm<sup>3</sup>) were taken in the upper 150 m

from one of the holes from the bottom of each section using a 60 mL syringe, excluding the section from which the whole round came (Fig. F12). A 25 mm diameter wire was inserted through two holes drilled at the end of the syringe in order to facilitate clean removal of the sediment. When the syringe was completely inserted into the core (and full of sediment), the syringe was rotated before removal to cut the sample cleanly from the section. Sediment plugs were taken on the catwalk, before running the core through the STMSL. This sampling technique was used to obtain high-resolution interstitial water samples while minimizing impact on the continuity of the core. No acetone was used to seal the end caps of the cut cores until after all interstitial water had been extracted because organic solvents can interfere with the spectroscopic analysis of stable water isotopes.

At Site U1385, interstitial water was also sampled using Rhizon samplers (Rhizosphere Research Products), consisting of a hydrophilic porous polymer tube (Seeberg-Elverfeldt et al., 2005). Two methods were employed at this site in order to assess and compare their performance in five areas:

1. Contamination of interstitial water chemistry,
2. Amount of disturbance to the sediment and stratigraphy,
3. Amount of water recovered,
4. Ease of implementation, and
5. Efficiency/disruption to core flow.

Rhizon samplers were carefully inserted through holes drilled in the core liner. Syringes were attached to each Rhizon sampler with a Luer-lock, pulled to generate vacuum, and held open with wooden spacers. Samplers were left in place during the core temperature equilibration ( $\sim 3$  h). We found that emptying the syringes and re-pulling vacuum on the Rhizon samplers at intervals of  $\sim 30$  min to 1 h increased their yield. The Rhizon samplers were used in sets of three spaced 3 cm apart at the center of each section (i.e., 75 cm). Water from all three samplers was combined into one sample and shaken to mix before analysis and splitting. Contrary to the methods used on previous expeditions, the Rhizon samplers were used dry in order to avoid sample contamination from presoaking. In qualitative tests done during Expedition 339, we found that flow rate through the Rhizon samplers did not depend on presoaking. Further, stable water isotope measurements were sensitive to the isotopic values of the solution in which the Rhizon samplers were presoaked, even when the first few milliliters were discarded from the syringe during sampling. That is, after an initial sampling period using a presoaked Rhizon, the syringe was detached from the Rhizon, a few milliliters of

water were discarded, and then the syringe was reattached and a “fresh” sample was taken. The isotopic measurements of this “fresh” sample were different than those of the sample taken with a dry Rhizon sampler. Because of the low total water volume recovery, the presoaking fluid cannot be flushed completely from the Rhizon sampler in order to recover an uncontaminated measurement.

In the shipboard laboratory, whole-round sediment samples were removed from the core liner and the outside surfaces (~1 cm) of the sediment samples were carefully scraped off with spatulas to minimize potential contamination with drill fluid. The drill fluid used was surface seawater, which had significant sulfate concentration at all sites; therefore, contamination of samples below the sulfate reduction zone was inferred when there were small deviations from 0 in the sulfate profile. Scraped whole-round sediment samples were placed into a Manheim titanium squeezer and squeezed at ambient temperature with a Carver hydraulic press (Manheim and Sayles, 1974), reaching pressures typically up to 200 MPa and occasionally as high as 300 MPa, if needed. Interstitial water samples discharged from the squeezer were passed through 0.45  $\mu\text{m}$  polyethersulfone membrane filters, collected in plastic syringes, and stored in plastic sample tubes for shipboard analyses or archived in flame-sealed glass ampules for shore-based analyses. Samples used for analysis by inductively coupled plasma–atomic emission spectrometer (ICP-AES) were acidified with  $\text{HNO}_3$  in order to prevent precipitation of element complexes.

### Interstitial water chemistry

Interstitial water analyses followed the procedures outlined by Gieskes et al. (1991), Murray et al. (2000), and user manuals for the new shipboard instrumentation with modifications as indicated (see “Geochemistry” in each site chapter).

Interstitial water samples were analyzed for salinity with a digital refractometer made by Index Instruments Ltd., for pH and alkalinity by Gran titration with a Brinkman pH electrode and Metrohm 794 Basic Titrino autotitrator, for  $\text{Cl}^-$  concentrations by titration against silver nitrate using a Metrohm 785 DMP Titrino Autotitration system, and for  $\text{SO}_4^{2-}$  concentrations by ion chromatography with a Dionex ICS-3000 ion chromatograph. Alkalinity is reported throughout as milliequivalences per liter (meq/L), which means the equivalent millimols of hydrogen ion added (in the form of HCl) to bring 1 L of sample to the reaction’s final endpoint. Measurements by the Dionex were made on autodilutions of 1/200 (v/v) sample to deionized water. For  $\text{Cl}^-$  titrations, 0.3–0.5 mL samples

of interstitial water were diluted with 30 mL of dilute nitric acid to keep precipitated flocculent well separated, which increased the probability of contact between  $\text{Cl}^-$  and  $\text{Ag}^+$ . Dissolved ammonium concentration was determined spectrophotometrically (Gieskes et al., 1991) using an Agilent Cary 100 ultraviolet-visible light (UV-VIS) spectrophotometer.

Major and minor elements were determined with the Teledyne Prodigy high-dispersion ICP-AES. ICP-AES techniques for the major cations  $\text{Na}^+$ ,  $\text{Mg}^{2+}$ ,  $\text{Ca}^{2+}$ , and  $\text{K}^+$  used dilutions of International Association for the Physical Sciences of the Ocean (IAPSO) standard seawater as calibration standards. For major element analysis on the ICP-AES, standards and acidified samples were diluted 1:100 (v/v) with a 2%  $\text{HNO}_3$  (by volume) solution (matrix) with Y at 10 ppm as an internal standard. Calibration for the minor elements  $\text{Mn}^{2+}$ ,  $\text{Fe}^{2+}$ , B, Si,  $\text{Sr}^{2+}$ ,  $\text{Ba}^{2+}$ , and  $\text{Li}^+$  was done with dilutions of a multielement synthetic standard solution (composed of single-element standards). Acidified samples measured for minor elements on the ICP-AES were diluted 1:10 (v/v) with the same matrix used for the major element analysis. Drift correction was made for both major and minor elements using the factor from a drift monitor solution (high-value standard solution) that was analyzed every five samples. The ICP-AES autosampler and analysis chamber were rinsed with a 3% (by volume)  $\text{HNO}_3$  solution between samples. Major cations  $\text{Mg}^{2+}$ ,  $\text{Ca}^{2+}$ ,  $\text{K}^+$ , and  $\text{Na}^+$  were also determined by ion chromatography on the same 1:200 dilutions used for sulfate determinations. Because values measured on both the ion chromatograph and the ICP-AES agreed well at Sites U1385–U1387, the major cations were only measured on the ion chromatograph for Sites U1388–U1391.

Typical precision of digital refractometer measurements is 0.1% (1‰). On the ion chromatograph, typical internal precision (standard deviation/average measured value) from eight measurements of a standard for  $\text{Na}^+$ ,  $\text{K}^+$ ,  $\text{Mg}^{2+}$ ,  $\text{Ca}^{2+}$ , and  $\text{SO}_4^{2-}$  was, respectively, <0.5%, <1%, <1%, <2%, and <1.5%. Replicates of IAPSO alkalinity measurements throughout the expedition were usually within 2% of the theoretical value ( $[\text{measured} - \text{theoretical}]/\text{theoretical}$ ), with a maximum measured error of 5%. Chloride standard and sample replicate maximum variation using titration was generally <0.8% (maximum difference/average) and often as low as or lower than 0.2%, particularly for the higher concentration samples. Internal precision on the ICP-AES measurements (four replicates) of minor major and minor elements was <3%. Typical external precision for major elements measured on the ICP-AES was <3%

(relative standard deviation [RSD]). The spectrophotometer internal precision (RSD) was 0.01% and the external precision was <0.5%.

Chemical data for interstitial water are reported in molar concentration units in each site report. No water samples were weighed over the course of the expedition; all measured dilutions were done volumetrically, either by autodilution or pipetting.

### Water isotope analysis

Oxygen and hydrogen isotope measurements of interstitial water were made for the first time aboard the *JOIDES Resolution* by cavity ringdown laser spectroscopy (CRDS). CRDS is a time-based measurement system that uses a laser to quantify spectral absorption lines unique to  $\text{H}_2^{16}\text{O}$ ,  $\text{H}_2^{18}\text{O}$ , and  $\text{HD}^{16}\text{O}$  in an optical cavity (Gupta et al., 2009). The equipment consisted of an L1102-*i* Picarro water isotope analyzer manufactured in July 2009 (serial number 202-HBDS033; 200-CPVU-HBQ33), an A0211 high-precision vaporizer manufactured in August 2011 (serial number VAP 292), and a CTC HTC-Pal liquid autosampler (serial number 142552). The Picarro L1102-*i* measures  $\delta^{18}\text{O}$ ,  $\delta\text{D}$ , and total  $\text{H}_2\text{O}$  concentration simultaneously. The bench-top instrument is field deployable, and shock and vibration tests indicate the ship environment should have no impact on instrument performance. Guaranteed precision for liquid water using the Picarro L1102-*i* with autosampler injection is <0.1‰ for  $\delta^{18}\text{O}$  and <0.5‰ for  $\delta\text{D}$ . Guaranteed drift is less than  $\pm 0.3\%$  for  $\delta^{18}\text{O}$  and less than  $\pm 0.9\%$  for  $\delta\text{D}$ . Precision and drift are defined based on the standard deviation and range (maximum – minimum) of the average values for 12 injections of the same water sample (tap water) measured 12 times, which is equivalent to 144 injections averaged in blocks of 12.

During Expedition 339, approximately 500  $\mu\text{L}$  of filtered interstitial water was loaded in a 2 mL glass vial with septum top and placed in the autosampler. Each water sample was injected into the vaporizer nine times. Memory effects from previous samples were avoided by rejecting the first three results and averaging the final six injections. An internal seawater standard (SPIT) was analyzed between each unknown sample to correct for drift. Each value measured on an unknown sample was normalized to the mean of the two adjacent standards. Analysis of each sample, consisting of nine injections, took 90 min. Three hours per sample is required if one includes the time needed to measure bracketing standards. The vaporizer septum was changed regularly, after no more than 300 injections. Considerable salt buildup occurred in the vaporizer, which necessi-

tated periodic cleaning. We used two vaporizers so that one could be cleaned while the other was analyzing samples.

The instrument was calibrated using three working standards from the University of Cambridge (United Kingdom) with known values: Delta ( $\delta^{18}\text{O} = -27.6$ ;  $\delta\text{D} = -213.5$ ), Botty ( $\delta^{18}\text{O} = -7.65$ ;  $\delta\text{D} = -52.6$ ), and either standard mean ocean water (SMOW) or SPIT ( $\delta^{18}\text{O} = 0$ ;  $\delta\text{D} = 0$ ). The  $\delta^{18}\text{O}$  and  $\delta\text{D}$  of SPIT is indistinguishable from SMOW within analytical error. Because the Picarro analyzer is extremely linear, it is only necessary to use three calibration standards. The calibration line was determined by subtracting the measured values of SPIT from each of the standards and deriving a regression equation forced through the origin. Over the duration of the expedition, the slope of the  $\delta^{18}\text{O}$  regression varied between 1.051 and 1.083 (average = 1.067), whereas the  $\delta\text{D}$  slope varied from 1.129 to 1.160 (average = 1.147). Measured  $\delta^{18}\text{O}$  and  $\delta\text{D}$  were corrected to Vienna SMOW in parts per thousand (‰) by multiplying the SPIT-normalized value by the slope of the calibration line. Because organic compounds can cause spectroscopic interference in CRDS and affect isotopic results, we processed the data using Picarro's ChemCorrect software that identifies irregularities caused by hydrocarbons. Despite significant amounts of methane in headspace samples, interstitial water samples were not flagged as being contaminated by the ChemCorrect software, suggesting that methane gas was lost during the interstitial water sampling and squeezing process.

Figures F13 and F14 show the measured  $\delta^{18}\text{O}$  and  $\delta\text{D}$  of the SPIT standard measured for approximately a 1.5 month period. The measured  $\delta^{18}\text{O}$  and  $\delta\text{D}$  values vary considerably, with a range of 3‰ and 13.6‰, respectively. Shifts in values are expected between runs as instrument conditions vary, but jumps also occurred in the middle of some runs. The cause of this atypical behavior could not be determined onboard. As shown in Figure F14, the times of the shifts did not correspond to power outages (PO) or autosampler septum changes (S). The shifts in isotopic value were corrected by normalizing to the mean of adjacent values. In the normalized data, the shifts largely disappeared except for samples straddling the boundaries of the shift. Care was taken to eliminate any sample data run near one of these shifts. The standard deviation ( $1\sigma$ ) of the normalized SPIT values over the 1.5 month period was  $\pm 0.2\%$  for  $\delta^{18}\text{O}$  and  $\pm 0.6\%$  for  $\delta\text{D}$ . At Site U1386, we replicated seven samples (10% of the samples taken), and the mean difference of the absolute values of replicate analyses was 0.05‰ for  $\delta^{18}\text{O}$  and  $\pm 0.4\%$  for  $\delta\text{D}$ . Ad-

ditional replication will occur postcruise to determine the reproducibility of the measurements.

### Bulk sediment geochemistry

#### *Sedimentary inorganic and organic carbon*

Inorganic carbon concentrations were determined using a Coulometrics 5011 carbon dioxide coulometer. Samples of ~10 mg of freeze-dried ground sediment were reacted with 2N HCl. The liberated CO<sub>2</sub> was back-titrated to a colorimetric end point. Calcium carbonate content, as weight percent, was calculated from the inorganic carbon (IC) content with the assumption that all inorganic carbon is present as calcium carbonate,

$$\text{wt\% CaCO}_3 = \text{wt\% IC} \times 8.33.$$

Reproducibility was determined by replicate measurements of selected samples and standards treated as samples, with typical absolute standard deviations of 0.3–0.4 wt% on sample and standard duplicates.

Total carbon content was determined using a Thermo Electron Flash EA 1112 element analyzer equipped with a Thermo Electron packed column CHNS/NCS (polytetrafluoroethylene; length = 2 m; diameter = 6 mm × 5 mm) and thermal conductivity detector (TCD) on a subset of the samples used for inorganic carbon determinations. Aliquots of 10 mg of freeze-dried ground sediment in tin cups were combusted at 1800°C in a stream of oxygen. Nitrogen oxides were reduced to N<sub>2</sub>, and the mixture of N<sub>2</sub>, CO<sub>2</sub>, H<sub>2</sub>O, and SO<sub>2</sub> gases was separated by gas chromatography and detection performed by the TCD. The gas chromatograph oven temperature was set at 65°C. H<sub>2</sub> values represent hydrogen from both organic matter and (clay) minerals. All measurements were calibrated by comparison to pure sulfanilamide as a standard. The reproducibility of total carbon measurements was determined to be from ±0.03 to ±0.06 wt% (1σ; N = 5), with a typical detection limit of 0.03 wt%. Contents of total organic carbon (TOC), as weight percent, were calculated as the difference between total carbon (TC) and inorganic carbon,

$$\text{wt\% TOC} = \text{wt\% TC} - \text{wt\% IC}.$$

The “acidification method” of TOC analysis was not applied for direct analysis. Freeze-dried samples (~30 mg) in precombusted silver capsules were treated with small aliquots (10 μL) of 2N HCl at room temperature to remove CaCO<sub>3</sub>; however, the available silver capsules disintegrated, resulting in sample loss.

## Downhole measurements

Downhole logs are used to determine physical, chemical, and structural properties of the formation penetrated by a borehole. The data are rapidly collected, continuous with depth, and measured in situ; they can be interpreted in terms of the stratigraphy, lithology, mineralogy, and geochemical composition of the penetrated formation. Where core recovery is incomplete or disturbed, log data may provide the only way to characterize the borehole section. Where core recovery is good, log and core data complement one another and may be interpreted jointly.

Downhole logs measure formation properties on a scale that is intermediate between those obtained from laboratory measurements on core samples and geophysical surveys. They are useful in calibrating the interpretation of geophysical survey data (e.g., through the use of synthetic seismograms) and provide a necessary link for the integrated understanding of physical properties on all scales.

### Wireline logging

During wireline logging operations, the logs are recorded with Schlumberger logging tools combined into tool strings, which are lowered into the hole after completion of coring operations. Three tool strings were used during Expedition 339: the triple combination (triple combo), which measures natural gamma radiation, porosity, density, and resistivity; the Formation MicroScanner (FMS)-sonic, which provides FMS resistivity images of the borehole wall and sonic velocities; and the Versatile Seismic Imager (VSI) for the vertical seismic profile (VSP) (Fig. F15; Table T5). Each tool string also contains a telemetry cartridge for communicating through the wireline to the Schlumberger data acquisition system (MAXIS unit) on the drillship. The triple combo was run in different configurations in order to test the High-Resolution Laterolog Array (HRLA), which was run in sedimentary formations for the first time in IODP.

In preparation for logging, the boreholes were flushed of debris by circulating a high-viscosity mud (sepiolite) sweep and filled with heavy mud (attapulgitite weighted with barite; approximate density = 10.5 lb/gal) to help stabilize the borehole walls. The BHA was pulled up to between 84 and 102 m WSF to cover the unstable upper part of the hole. The tool strings were then lowered downhole on a seven-conductor wireline cable before being pulled up at constant speed, typically 275 or 550 m/h, to provide continuous measurements of several properties simultaneously. A wireline heave compensator (WHC) was used to minimize the effect of ship's

heave on the tool position in the borehole (see below). During each logging run, incoming data were recorded and monitored in real time on the Schlumberger MCM MAXIS logging computer.

### Logged sediment properties and tool measurement principles

The logged properties, and the principles used in the tools to measure them, are briefly described in this section. The main logs are listed in Table T6. More detailed information on individual tools and their geological applications may be found in Serra (1984, 1986, 1989), Schlumberger (1989, 1994), Rider (1996), Goldberg (1997), Lovell et al. (1998), and Ellis and Singer (2007). A complete online list of acronyms for the Schlumberger tools and measurement curves is at [www.slb.com/modules/mnemonics/index.aspx](http://www.slb.com/modules/mnemonics/index.aspx).

#### Natural gamma radioactivity

The Hostile Environment Natural Gamma Ray Sonde (HNGS) was used on the triple combo tool string to measure and classify NGR in the formation. It has two bismuth germanate scintillation detectors and uses five-window spectroscopy to determine concentrations of K, U, and Th from the characteristic gamma ray energies of isotopes in the  $^{40}\text{K}$ ,  $^{232}\text{Th}$ , and  $^{238}\text{U}$  radioactive decay series.

An additional NGR sensor is housed in the Enhanced Digital Telemetry Cartridge (EDTC), run on all tool strings. Its sodium iodide scintillation detector measures the total NGR emission of the formation, with no spectral information.

The inclusion of a gamma ray sonde in every tool string allows use of the NGR data for depth correlation between logging strings and passes and for core-log integration. Although the EDTC NGR measurement has less sensitivity than the HNGS measurement, it was sufficiently accurate to be used for depth matching because of the generally high NGR values and the abundance of distinctive features in the logs at the Expedition 339 sites.

#### Density and photoelectric factor

Formation density was measured with the Hostile Environment Litho-Density Sonde (HLDS). The sonde contains a radioactive cesium ( $^{137}\text{Cs}$ ) gamma ray source (622 keV) and far and near gamma ray detectors mounted on a shielded skid, which is pressed against the borehole wall by a hydraulically activated decentralizing arm. Gamma rays emitted by the source undergo Compton scattering, in which gamma rays are scattered by electrons in the formation. The number of scattered gamma rays that reach

the detectors is proportional to the density of electrons in the formation, which is in turn related to bulk density. Porosity may also be derived from this bulk density if the matrix (grain) density is known.

The HLDS also measures photoelectric absorption as the photoelectric factor (PEF). Photoelectric absorption of the gamma rays occurs when their energy falls below 150 keV as a result of being repeatedly scattered by electrons in the formation. Because PEF is higher for elements with a higher atomic number, it also varies according to the mineral composition and can be used for the identification of some minerals. For example, the PEF of calcite is 5.08 b/e<sup>-</sup>, illite is 3.03 b/e<sup>-</sup>, quartz is 1.81 b/e<sup>-</sup>, and kaolinite is 1.49 b/e<sup>-</sup>. Good contact between the tool and borehole wall is essential for good HLDS logs; poor contact results in underestimation of density values.

#### Porosity

Formation porosity was measured with the Accelerator Porosity Sonde (APS) in two holes (U1387C and U1389E). It was not run in the other holes because the often-wide borehole and porous sediments were not ideally suited for the APS porosity measurement. The sonde includes a minitron neutron generator that produces fast (14.4 MeV) neutrons and five neutron detectors (four epithermal and one thermal) positioned at different distances from the minitron. The tool's detectors count neutrons that arrive at the detectors after being scattered and slowed by collisions with atomic nuclei in the formation.

The highest energy loss occurs when neutrons collide with hydrogen nuclei, which have practically the same mass as the neutron (the neutrons bounce off of heavier elements without losing much energy). If the hydrogen (i.e., water) concentration is low, as in low-porosity formations, neutrons can travel farther before being captured and the count rates increase at the detector. The opposite effect occurs in high-porosity formations where the water content is high. However, because hydrogen bound in minerals such as clays or in hydrocarbons also contributes to the measurement, the raw porosity value is often an overestimate.

Upon reaching thermal energies (0.025 eV), the neutrons are captured by the nuclei of Cl, Si, B, and other elements, resulting in a gamma ray emission. This neutron capture cross section ( $\Sigma_t$ ) is also measured by the tool.

#### Electrical resistivity

This expedition continues the transition to the HRLA resistivity tool from the reliable but dated Phasor Dual Induction/Spherically Focused Resistivity

tool (DIT), which is being retired. The HRLA was first used during IODP Expedition 335 in Hole 1256D, but had not been run in low-resistivity IODP sediment formations until this expedition.

The HRLA provides six resistivity measurements with different depths of investigation, including the borehole mud resistivity and five measurements of formation resistivity with increasing penetration into the formation. The tool sends a focused current into the formation and measures the intensity necessary to maintain a constant drop in voltage across a fixed interval, providing direct resistivity measurements. The tool has one central (source) electrode and six electrodes above and below it, which serve alternatively as focusing and returning current electrodes. By rapidly changing the role of these electrodes, a simultaneous resistivity measurement at six penetration depths is achieved. The tool is designed to ensure that all signals are measured at exactly the same time and tool position, and to reduce the sensitivity to “shoulder bed” effects when crossing sharp beds thinner than the electrode spacing. The design of the HRLA, which eliminates the need for a surface reference electrode, improves formation resistivity evaluation compared to the traditional dual induction. The HRLA needs to be run centralized in the borehole for optimal results, so bowspring centralizers are used to keep the HRLA in the center of the borehole, while knuckle joints allow the density and porosity tools to be eccentralized and maintain good contact with the borehole wall (Fig. F15).

The DIT was used to measure electrical resistivity in Hole U1386C as a quality control check because the HRLA was untested in the low-resistivity formations commonly logged in IODP. The DIT provides three measures of electrical resistivity, each with a different depth of investigation into the formation (Table T6). The two induction devices (deep and medium depths of penetration) transmit high-frequency alternating currents through transmitter coils, creating magnetic fields that induce secondary currents in the formation. These currents produce a new inductive signal, proportional to the conductivity of the formation, which is measured by the receiving coils. The measured conductivities are then converted to resistivity (in ohm-meters). The spherically focused resistivity is measured by an electrode device that sends a current into the formation maintaining a constant voltage drop. The amount of current necessary to keep the voltage gives a direct measure of resistivity. This device uses several electrodes to focus the current flow into the formation so that equipotential surfaces are spherical and has a higher vertical resolution than the induction measurements.

Calcite, silica, and hydrocarbons are electrical insulators, whereas ionic solutions like interstitial water are conductors. Electrical resistivity, therefore, can be used to evaluate porosity for a given salinity and resistivity of the interstitial water. Clay surface conduction also contributes to the resistivity values, but at high porosities this is a relatively minor effect.

### Acoustic velocity

The Dipole Shear Sonic Imager measures the transit times between sonic transmitters and an array of eight receivers. It combines replicate measurements, thus providing a direct measurement of sound velocity through formations that is relatively free from the effects of formation damage and an enlarged borehole (Schlumberger, 1989). Along with the monopole transmitters found on most sonic tools, it also has two crossed-dipole transmitters, which allow the measurement of shear wave velocity in addition to compressional wave velocity. Dipole measurements are necessary to measure shear velocities in slow formations whose shear velocity is less than the velocity of sound in the borehole fluid. Such slow formations are typically encountered in deep-ocean drilling.

### Formation MicroScanner

The FMS provides high-resolution electrical resistivity-based images of borehole walls. The tool has four orthogonal arms and pads, each containing 16 button electrodes that are pressed against the borehole wall during logging. The electrodes are arranged in two diagonally offset rows of eight electrodes each. A focused current is emitted from the button electrodes into the formation, with a return electrode near the top of the tool. Resistivity of the formation at the button electrodes is derived from the intensity of current passing through the button electrodes. Processing transforms these measurements into oriented high-resolution images that reveal the geologic structures of the borehole wall.

The development of the FMS added a new dimension to wireline logging (Luthi, 1990; Salimullah and Stow, 1992; Lovell et al., 1998). Features such as bedding, stratification, fracturing, slump folding, and bioturbation can be resolved. Because the images are oriented to magnetic north, further analysis can be carried out to provide measurement of the dip and direction (azimuth) of planar features in the formation. In addition, when the corresponding planar features can be identified in the recovered core samples, individual core pieces can be reoriented with respect to true north.

The maximum extension of the caliper arms is 40.6 cm (16 inches). In holes with a diameter greater than

this maximum (relatively common during Expedition 339), the pad contact at the end of the caliper arms will be inconsistent, and the FMS images may appear out of focus and too conductive. Irregular (rough) borehole walls will also adversely affect the images if contact with the wall is poor. Standard procedure is to make two full passes up the borehole with the FMS to maximize the chance of getting full borehole coverage with the pads.

### Vertical seismic profile

In a VSP experiment, a borehole seismic tool is anchored against the borehole wall at regularly spaced intervals and records the full waveform of elastic waves generated by a seismic source positioned just below the sea surface. These “check shot” measurements relate depth in the hole to traveltime in reflection seismic lines. The VSI used here contains a three-axis geophone. In the planned VSP survey, the VSI was anchored against the borehole wall at approximately 25 m station intervals (where possible), with 5–10 air gun shots typically taken at each station. The recorded waveforms were stacked and a one-way traveltime was determined from the median of the first breaks for each station. The seismic source used was a Sercel G. Gun Parallel Cluster, composed of two 250 in<sup>3</sup> air guns separated by 1 m. It was positioned on the port side of the *JOIDES Resolution* at a water depth of ~7 meters below sea level (mbsl) with a borehole offset of ~45 m.

Precautions were taken to protect marine mammals. If there were no mammals in or approaching the safety radius (940 m for water depths >1000 m, 1850 m for water depths between 100 and 1000 m), air gun operations commenced using a ramp-up, or “soft start” procedure (gradually increasing the operational pressure and air gun firing interval) to provide time for undetected animals to respond to the sounds and vacate the area. Once the air guns were at full power, the check shot survey proceeded. Marine mammal observations continued during the check shot survey and if a mammal entered the safety radius, the survey was suspended.

### Log data quality

The main influence on log data quality is the condition of the borehole wall. Where the borehole diameter varies over short intervals because of washouts (wide borehole) or ledges made of layers of harder material, the logs from tools that require good contact with the borehole wall (i.e., the FMS, density, and porosity tools) may be degraded. Deep investigation measurements such as gamma ray, resistivity, and sonic velocity, which do not require contact with the borehole wall, are generally less sensitive to

borehole conditions. Very narrow (“bridged”) sections will also cause irregular log results. The quality of the borehole is improved by minimizing the circulation of drilling fluid while drilling, flushing the borehole to remove debris, and logging as soon as possible after drilling and hole conditioning are completed. During the expedition, increased drilling fluid circulation was required to prevent clay from gumming up the roller-cones on the RCB bit, which resulted in washing out (widening) the borehole in places. Conversely, holes drilled with the APC/XCB polycrystalline diamond compact drill bit (PDC; without roller cones) were less washed out and therefore in better condition for logging.

The quality of the wireline depth determination depends on several factors. The depth of the logging measurements is determined from the length of the cable played out from the winch on the ship. The seafloor is identified on the NGR log by the abrupt reduction in gamma ray count at the water/sediment boundary (mudline). Discrepancies between the drilling depth and the wireline log depth occur. In the case of drilling depth, discrepancies are because of core expansion, incomplete core recovery, or incomplete heave compensation. In the case of log depth, discrepancies between successive runs occur because of incomplete heave compensation, incomplete correction for cable stretch, and cable slip. Tidal changes in sea level affect both drilling and logging depths. To minimize the wireline tool motion caused by ship heave, a hydraulic WHC was used to adjust the wireline length to compensate vertical rig motion during wireline logging operations.

### Wireline heave compensator

The current WHC system, which was first used during IODP Expedition 320T (February 2009), is designed to compensate for the vertical motion of the ship and maintain a steady motion of the logging tools. It uses vertical acceleration measurements made by a motion reference unit (MRU) located under the rig floor near the center of gravity of the ship, to calculate the vertical motion of the ship. It then adjusts the length of the wireline by varying the distance between two sets of pulleys through which the cable passes. Real-time measurements of uphole (surface) and downhole acceleration are made simultaneously by the MRU and the EDTC, respectively. A Lamont-Doherty Earth Observatory (LDEO)-developed software package allows these data to be analyzed and compared in real time, displaying the actual motion of the logging tool string and enabling monitoring of the efficiency of the compensator.

## Logging data flow and log depth scales

Data for each wireline logging run were monitored in real time and recorded using the Schlumberger MAXIS 500 system. The initial logging data were referenced to the rig floor (WRF). After logging was completed, the data were shifted to a seafloor reference (WSF), which was based on the step in gamma radiation at the sediment/water interface.

The data were transferred on shore to LDEO, where standardized data processing took place. The main part of the processing is depth matching to remove depth offsets between data from different logging runs, which results in a new depth scale, wireline log matched depth below seafloor (WMSF). Also, corrections are made to certain tools and logs (e.g., FMS imagery is corrected for tool acceleration, including “stick and slip” motion), documentation for the logs (with an assessment of log quality) is prepared, and the data are converted to ASCII for the conventional logs and GIF for the FMS images. Schlumberger GeoQuest’s GeoFrame software package is used for most of the wireline log data processing. The data were transferred back to the ship within a few days of logging, and this processed data set was made available to the science party (in ASCII and DLIS formats) through the shipboard IODP logging database and shipboard servers.

## In situ temperature measurements

During Expedition 339, in situ temperature measurements were made with the APCT-3. At least four in situ temperature measurements were made at each site using the APCT-3. The APCT-3 fits directly into the coring shoe of the APC and consists of a battery pack, data logger, and a platinum resistance-temperature device calibrated over a temperature range from 0° to 30°C. Before entering the borehole, the tool is first stopped at the mudline for 5 min to thermally equilibrate with bottom water. However, the lowest temperature recorded during the run down was occasionally preferred to the average temperature at the mudline as an estimate of the bottom water temperature because it was more repeatable and bottom water is expected to have the lowest temperature in the profile. After the APC penetrated the sediment, it was held in place for about 6 min as the APCT-3 recorded the temperature of the cutting shoe every second (a longer equilibration time is preferable). When the APC is plunged into the formation, there is an instantaneous temperature rise from frictional heating. This heat gradually dissipates into the surrounding sediments as the temperature at the APCT-3 equilibrates toward the temperature of the sediments.

The equilibrium temperature of the sediments was estimated by applying a mathematical heat-conduction model to the temperature decay record (Horai and Von Herzen, 1985). The synthetic thermal decay curve for the APCT-3 tool is a function of the geometry and thermal properties of the probe and the sediments (Bullard, 1954; Horai and Von Herzen, 1985). The equilibrium temperature must be estimated by applying a fitting procedure (Pribnow et al., 2000). However, where the APC has not achieved a full stroke or where ship heave pulls the APC up from full penetration, the temperature equilibration curve will be disturbed and temperature determination is more difficult. The nominal accuracy of the APCT-3 temperature measurements is  $\pm 0.05^\circ\text{C}$ .

The APCT-3 tool temperature data were combined with measurements of thermal conductivity (see “Physical properties”) obtained from whole-core samples to obtain heat flow values. Heat flow was calculated according to the Bullard method, to be consistent with the synthesis of ODP heat flow data by Pribnow et al. (2000).

## Stratigraphic correlation

Many of the scientific objectives of Expedition 339 depend on recovery of complete stratigraphic sections. Such sections cannot be recovered from a single IODP borehole because core-recovery gaps occur between successive cores despite 100% or more nominal recovery (e.g., Ruddiman, Kidd, Thomas, et al., 1987; Hagelberg et al., 1995; Acton et al., 2001). The construction of a complete composite section, referred to as a splice, requires the combination of stratigraphic intervals from two or more holes cored at the same site. To maximize the probability of bridging gaps between successive cores in individual holes, the starting depths below seafloor from which cores are recovered are offset between holes. This practice ensures that most missing sedimentary sections from intercore gaps within a given hole are recovered in one or more adjacent holes. Usually at least two complete holes and a third partial hole must be cored to recover a complete section in the APC portion at a site. Additional holes are cored to allow for the construction of alternate splices, where possible.

The composite section and splice construction methodology employed during Expedition 339 follows the basic strategy originally developed during ODP Leg 138 (e.g., Hagelberg et al., 1992, 1995) and later refined during many other ODP legs and IODP expeditions. This strategy is now common practice on all high-resolution paleoceanographic expeditions. Assembly and verification of a complete composite

stratigraphic section requires construction of a composite depth scale, referred to as the meters composite depth scale. The composite depth scale provides a common depth scale for the holes at a site unlike the original meters below seafloor scale, which is based on drill string measurements that are unique to each hole.

### Meters below seafloor depth scale

The depth to the top of each core is based on a drill string measurement, which is determined by the length of drill string below the rig floor to the top of the cored interval minus the length of drill string from the rig floor to the mudline (assumed to be the seafloor). The depth to a point along the core is determined by adding the distance the point occurs from the top of the core to the core top depth. This depth scale is referred to as meters CSF-A, which is equivalent to the ODP meters below seafloor depth scale.

The zero depth point of the meters below seafloor scale is defined by the mudline in the first core of each hole. It is often difficult to tell whether this empirical mudline recovers the true sediment/water interface. Some holes are inadvertently (or purposely) started below the sediment/water interface. In this case, the zero depth point in meters below seafloor units may be substantially offset from the zero depth point in adjacent holes that successfully recover the sediment/water interface.

The meters below seafloor scale may also be inaccurate because of ship heave, tidal variations in sea level, and other sources of error. Tidal influence on depth was first predicted during ODP Leg 138 (Hagelberg et al., 1995) and was proven by correlation of affine offset changes and tide height during ODP Leg 202 (Mix, Tiedemann, Blum, et al., 2003). Expedition 339 was fortunate to core during relatively benign seas, with ship heave remaining relatively small for all seven sites. Tidal variations were thus the largest source of variation in the meters below seafloor depth scale from one hole to the next. Because these are predictable, pipe offsets could be adjusted with the goal of avoiding core gap alignment. For a variety of practical reasons, such as failure to get a complete 9.6 m stroke with the APC system for one or more cores from each hole, the goal can be difficult to achieve with just two holes and sometimes even with three.

### Meters composite depth scale

The goal of constructing a composite depth scale is to place coeval, laterally continuous stratigraphic features into a common frame of reference by depth

shifting the meters below seafloor depth scales of individual cores to maximize correlation between holes. In the composite depth scale used by ODP and IODP, referred to as the meters composite depth (mcd) scale, the depths of the individual cores can only be shifted by a constant amount, without permitting expansion or contraction of the relative depth scale within any core. Ultimately, this provides good first-order correlation between cores from different holes while also avoiding more subjective, and potentially erroneous, interpretations that might arise without applying this restriction first. The meters composite depth scale, once established, provides a basis upon which higher order depth composite scales can be built.

In essence, the meters composite depth scale overcomes many of the inadequacies of the meters below seafloor depth scale, which is unique to each hole and may be inaccurate as discussed above. Rather than using a drill string measurement, the meters composite depth scale is built by correlating features downhole from the mudline. The mudline is not merely taken as the top of the first core in a hole but is the top of the first core with the most representative or best-preserved mudline. This mudline establishes the top of the stratigraphic section and the core with this mudline becomes the “anchor” in the composite depth scale. It is typically the only core in which the depths are the same for both the meters below seafloor and meters composite scales. Each core downhole is tied to the composite section by adding or subtracting a depth offset (a constant) that best aligns the observed lithologic variations to the correlative variations for cores from adjacent holes. If between-core gaps are not aligned for the different holes and recovery is high, it should be possible to correlate each successive core downhole to a core from an adjacent hole. Gaps common to all holes cored at a site can occur, in which case cores downhole can be appended to the composite section. In such cases, the depth offset for the appended core can be adjusted to convey an estimate of the true size of the coring gap. For example, one could use the average growth factor (i.e., expansion) of the meters composite depth scale relative to the meters below seafloor depth scale or could use continuous logging data from a hole at the site or observations from other nearby sites.

In the process of constructing the composite section, the meters composite depth is virtually always expanded relative to the meters below seafloor scale. The expansion, which is typically ~5% to 15%, is mostly caused by real decompression of the cores as they are brought to the surface, by stretching that occurs as part of the coring process, and/or from cu-

ration practice, in which material that has fallen downhole or gas expansion voids are curated as part of the core (e.g., Hagelberg et al., 1995; Acton et al., 2001).

### Goals

The goals for stratigraphic correlation for Expedition 339, in order of priority, were to

1. Guide drilling to ensure recovery of a complete stratigraphic section;
2. Establish a composite depth scale; and
3. Define a stratigraphically complete and representative sampling splice and, if possible, one or more alternate splices.

This first-order correlation is commonly refined postcruise with the generation of adjusted or revised composite depth scales, which may also be used to link core and logging depths at sites where logging was done.

### Measurements and methods specific to Expedition 339

The composite sections and splices are based on the stratigraphic correlation of data from the IODP whole-core logger systems that measure physical and magnetic properties. Initial correlation was based primarily on using magnetic susceptibility from the WRMSL and STMSL. Both loggers measure susceptibility and density, and the WRMSL also measures *P*-wave velocity. The primary whole-core physical property data are generated using the WRMSL, which is generally set to make higher resolution, higher precision, and more time consuming measurements. These measurements are only done after the temperature of the core has equilibrated to laboratory temperature, or roughly 3 h after the core is collected. The STMSL was set to make lower resolution, lower precision, and more rapid measurements of susceptibility and density, without the requirement that the core equilibrates. More details on the instruments and their settings and measurement intervals for Expedition 339 are given in “[Physical properties](#)”.

We typically only collected data with the WRMSL for cores from Hole A, given that the duration of coring did not require a rapid record from this hole. Core sections from subsequent holes were measured immediately after they were labeled using the STMSL. This provided a susceptibility record rapidly for correlation with the previously cored hole or holes at a site, with the resulting correlation used to make decisions about drill string offset during coring operations. The STMSL data were subsequently superseded

by the WRMSL once those measurements were completed.

Final correlation involved the use of several data sets, with the magnetic susceptibility and NGR total counts per second providing anomalies that could be correlated most consistently for the Expedition 339 sites. Occasionally the whole-core density data and the lithostratigraphic variations were used to aid in the correlation. Other data, including color reflectance variations ( $L^*a^*b^*$ ), point magnetic susceptibility, and paleomagnetic inclination and intensity, were evaluated but did not have features as correlative between holes as did the whole-core susceptibility and NGR data.

Between-hole correlation of these data was accomplished mainly using Microsoft Excel or Correlator (version 1.695), although several other software packages were investigated, including Match (Lisiecki and Lisiecki, 2002), Autocomp (Lisiecki and Herbert, 2007), AnalySeries (Palliard et al., 1996), and KaleidaGraph. We found that use of dynamic tables and visual graphic correlation in Excel and visual and statistical correlation in Correlator worked well given the time constraints and goals.

For both methods, we generated standard affine tables, which list the offset that is added to each core to place it in the meters composite depth scale, and splice tables, which give the intervals that comprise the splice. The tables were uploaded into the LIMS database, which will provide composite depths in CCSF-A and CCSF-B, and spliced data sets for users directly from the LIMS database, although as of Expedition 339 those capabilities were lacking. The affine and splice tables provide all the necessary information needed to place any of the Expedition 339 data into the meters composite depth scale and for users to generate spliced data sets for each site.

## References

- Acton, G.D., Borton, C.J., and the Leg 178 Shipboard Scientific Party, 2001. Palmer Deep composite depth scales for Leg 178 Sites 1098 and 1099. *In* Barker, P.F., Camerlenghi, A., Acton, G.D., and Ramsay, A.T.S. (Eds.), *Proc. ODP, Sci. Results*, 178: College Station, TX (Ocean Drilling Program), 1–35. [doi:10.2973/odp.proc.sr.178.202.2001](#)
- Almogi-Labin, A., Luz, B., and Duplessy, J.-C., 1986. Quaternary paleo-oceanography, pteropod preservation and stable-isotope record of the Red Sea. *Palaeogeogr., Palaeoclimatol., Palaeoecol.*, 57(2–4):195–211. [doi:10.1016/0031-0182\(86\)90013-1](#)
- Alvarez Zariqian, C.A., 2009. Data report: late Quaternary ostracodes at IODP Site U1314 (North Atlantic Ocean). *In* Channell, J.E.T., Kanamatsu, T., Sato, T., Stein, R., Alvarez Zariqian, C.A., Malone, M.J., and the Expedition

- 303/306 Scientists, *Proc. IODP*, 303/306: College Station, TX (Integrated Ocean Drilling Program Management International, Inc.). doi:10.2204/iodp.proc.303306.213.2009
- Alvarez Zariqian, C.A., Stepanova, A.Y., and Grützner, J., 2009. Glacial–interglacial variability in deep sea ostracod assemblage composition at IODP Site U1314 in the subpolar North Atlantic. *Mar. Geol.*, 258(1–4):69–87. doi:10.1016/j.margeo.2008.11.009
- ASTM International, 1990. Standard method for laboratory determination of water (moisture) content of soil and rock (Standard D2216–90). In *Annual Book of ASTM Standards for Soil and Rock* (Vol. 04.08): Philadelphia (Am. Soc. Testing Mater.). [revision of D2216-63, D2216-80]
- Ayress, M., Neil, H., Passlow, V., and Swanson, K., 1997. Benthic ostracods and deep water masses: a qualitative comparison of Southwest Pacific, Southern, and Atlantic Oceans. *Palaeogeogr., Palaeoclimatol., Palaeoecol.*, 131(3–4):287–302. doi:10.1016/S0031-0182(97)00007-2
- Balsam, W.L., and Damuth, J.E., 2000. Further investigations of shipboard vs. shore-based spectral data: implications for interpreting Leg 164 sediment composition. In Paull, C.K., Matsumoto, R., Wallace, P., and Dillon, W.P. (Eds.), *Proc. ODP, Sci. Results*, 164: College Station, TX (Ocean Drilling Program), 313–324. doi:10.2973/odp.proc.sr.164.222.2000
- Balsam, W.L., Damuth, J.E., and Schneider, R.R., 1997. Comparison of shipboard vs. shore-based spectral data from Amazon Fan cores: implications for interpreting sediment composition. In Flood, R.D., Piper, D.J.W., Klaus, A., and Peterson, L.C. (Eds.), *Proc. ODP, Sci. Results*, 155: College Station, TX (Ocean Drilling Program), 193–215. doi:10.2973/odp.proc.sr.155.210.1997
- Balsam, W.L., Deaton, B.C., and Damuth, J.E., 1998. The effects of water content on diffuse reflectance spectrophotometry studies of deep-sea sediment cores. *Mar. Geol.*, 149(1–4):177–189. doi:10.1016/S0025-3227(98)00033-4
- Baumann, K.-H., Andruleit, H., Böckel, B., Geisen, M., and Kinkel, H., 2005. The significance of extant coccolithophores as indicators of ocean water masses, surface water temperature, and paleoproductivity: a review. *Paläontol. Z.*, 79(1):93–112.
- Berggren, W.A., Kent, D.V., Swisher, C.C., III, and Aubry, M.-P., 1995. A revised Cenozoic geochronology and chronostratigraphy. In Berggren, W.A., Kent, D.V., Aubry, M.-P., and Hardenbol, J. (Eds.), *Geochronology, Time Scales and Global Stratigraphic Correlation*. Spec. Publ.—SEPM (Soc. Sediment. Geol.), 54:129–212.
- Blum, P., 1997. Physical properties handbook: a guide to the shipboard measurement of physical properties of deep-sea cores. *ODP Tech. Note*, 26. doi:10.2973/odp.tn.26.1997
- Bullard, E.C., 1954. The flow of heat through the floor of the Atlantic Ocean. *Proc. R. Soc. London, Ser. A*, 222(1150):408–429. doi:10.1098/rspa.1954.0085
- Chaisson, W.P., and Pearson, P.N., 1997. Planktonic foraminifer biostratigraphy at Site 925: middle Miocene–Pleistocene. In Shackleton, N.J., Curry, W.B., Richter, C., and Bralower, T.J. (Eds.), *Proc. ODP, Sci. Results*, 154: College Station, TX (Ocean Drilling Program), 3–31. doi:10.2973/odp.proc.sr.154.104.1997
- Coles, G., and Whatley, R., 1989. New Paleogene to Miocene genera and species of Ostracoda from DSDP sites in the North Atlantic. *Rev. Esp. Micropaleontol.*, 21:81–124.
- Colmenero-Hidalgo, E., Flores, J.-A., Sierro, F.J., Bárcena, M.A., Löwemark, L., Schönfeld, J., and Grimalt, J.O., 2004. Ocean surface water response to short-term climate changes revealed by coccolithophores from the Gulf of Cádiz (NE Atlantic) and Alboran Sea (W Mediterranean). *Palaeogeogr., Palaeoclimatol., Palaeoecol.*, 205(3–4):317–336. doi:10.1016/j.palaeo.2003.12.014
- Cook, H.E., Johnson, P.D., Matti, J.C., and Zemmels, I., 1975. Methods of sample preparation and X-ray diffraction data analysis, X-ray Mineralogy Laboratory, Deep Sea Drilling Project, University of California, Riverside. In Hayes, D.E., Frakes, L.A., et al., *Init. Repts. DSDP*, 28: Washington (U.S. Govt. Printing Office), 999–1007. doi:10.2973/dsdp.proc.28.app4.1975
- Corrège, T., 1993. The relationship between water masses and benthic ostracod assemblages in the western Coral Sea, Southwest Pacific. *Palaeogeogr., Palaeoclimatol., Palaeoecol.*, 105(3–4):245–266. doi:10.1016/0031-0182(93)90086-X
- Cronin, T.M., DeMartino, D.M., Dwyer, G.S., and Rodriguez-Lazaro, J., 1999. Deep-sea ostracode species diversity: response to late Quaternary climate change. *Mar. Micropaleontol.*, 37(3–4): 231–249. doi:10.1016/S0377-8398(99)00026-2
- Daniau, A.-L., Sánchez Goñi, M.F., Beaufort, L., Laggoun-Défarge, F., Loutre, M.-F., and Duprat, J., 2007. Dansgaard–Oeschger climatic variability revealed by fire emissions in southwestern Iberia. *Quat. Sci. Rev.*, 26(9–10):1369–1383. doi:10.1016/j.quascirev.2007.02.005
- Desprat, S., Sánchez Goñi, M.F., Turon, J.-L., McManus, J.F., Loutre, M.F., Duprat, J., Malaizé, B., Peyron, O., and Peypouquet, J.-P., 2005. Is vegetation responsible for glacial inception during periods of muted insolation changes? *Quat. Sci. Rev.*, 24(12–13):1361–1374. doi:10.1016/j.quascirev.2005.01.005
- Dingle, R.V., and Lord, A.R., 1990. Benthic ostracods and deep water-masses in the Atlantic Ocean. *Palaeogeogr., Palaeoclimatol., Palaeoecol.*, 80(3–4):213–235. doi:10.1016/0031-0182(90)90133-R
- Droser, M.L., and Bottjer, D.J., 1986. A semiquantitative field classification of ichnofabric. *J. Sediment. Res.*, 56(4):558–559. <http://jsedres.sepmonline.org/cgi/content/abstract/56/4/558>
- Ellis, D.V., and Singer, J.M., 2007. *Well Logging for Earth Scientists*, (2nd ed.): Dordrecht, The Netherlands (Springer).
- Evans, H.B., 1965. GRAPE—a device for continuous determination of material density and porosity. *Trans. SPWLA Annu. Logging Symp.*: 6(2):B1–B25.

- Expedition 303 Scientists, 2006. Site U1302–U1308 methods. In Channell, J.E.T., Kanamatsu, T., Sato, T., Stein, R., Alvarez Zarikian, C.A., Malone, M.J., and the Expedition 303/306 Scientists, *Proc. IODP*, 303/306: College Station, TX (Integrated Ocean Drilling Program Management International, Inc.). [doi:10.2204/iodp.proc.303306.102.2006](https://doi.org/10.2204/iodp.proc.303306.102.2006)
- Expedition 339 Scientists, 2013. Site U1385. In Stow, D.A.V., Hernández-Molina, F.J., Alvarez Zarikian, C.A., and the Expedition 339 Scientists, *Proc. IODP*, 339: Tokyo (Integrated Ocean Drilling Program Management International, Inc.). [doi:10.2204/iodp.proc.339.103.2013](https://doi.org/10.2204/iodp.proc.339.103.2013)
- Fletcher, W.J., Boski, T., and Moura, D., 2007. Palynological evidence for environmental and climatic change in the lower Guadiana Valley, Portugal, during the last 13,000 years. *The Holocene*, 17(4):481–494. [doi:10.1177/0959683607077027](https://doi.org/10.1177/0959683607077027)
- Flood, R.D., 1978. X-ray mineralogy of DSDP Legs 44 and 44A, Western North Atlantic: lower continental rise hills, Blake Nose, and Blake-Bahama Basin. In Benson, W.E., Sheridan, R.E., et al., *Init. Repts. DSDP*, 44: Washington, DC (U.S. Govt. Printing Office), 515–521. [doi:10.2973/dsdp.proc.44.112.1978](https://doi.org/10.2973/dsdp.proc.44.112.1978)
- Flores, J.-A., Colmenero-Hidalgo, E., Mejía-Molina, A.E., Baumann, K.-H., Hendericks, J., Larsson, K., Prabhu, C.N., Sierro, F.J., and Rodrigues, T., 2010. Distribution of large *Emiliania huxleyi* in the central and northeast Atlantic as a tracer of surface ocean dynamics during the last 25,000 years. *Mar. Micropaleontol.*, 76(3–4):53–66. [doi:10.1016/j.marmicro.2010.05.001](https://doi.org/10.1016/j.marmicro.2010.05.001)
- Gerhardt, S., Groth, H., Rühlemann, C., and Heinrich, R., 2000. Aragonite preservation in late Quaternary sediment cores on the Brazilian continental slope: implications for intermediate water circulation. *Int. J. Earth Sci.*, 88(4):607–618. [doi:10.1007/s005310050291](https://doi.org/10.1007/s005310050291)
- Geisen, M., Billard, C., Broerse, A., Cros, L., Probert, I., and Young, J., 2002. Life-cycle associations involving pairs of holococcolithophorid species: intraspecific variation or cryptic speciation? *Eur. J. Phycol.*, 37(4):531–550. [doi:10.1017/S0967026202003852](https://doi.org/10.1017/S0967026202003852)
- Gibbard, P.L., Head, M.J., and Walker, M.J.C., 2010. Formal ratification of the Quaternary system/period and the Pleistocene series/epoch with a base at 2.58 Ma. *J. Quat. Sci.*, 25(2):96–102. [doi:10.1002/jqs.1338](https://doi.org/10.1002/jqs.1338)
- Gieskes, J.M., Gamo, T., and Brumsack, H., 1991. Chemical methods for interstitial water analysis aboard *JOIDES Resolution*. *ODP Tech. Note*, 15. [doi:10.2973/odp.tn.15.1991](https://doi.org/10.2973/odp.tn.15.1991)
- Goldberg, D., 1997. The role of downhole measurements in marine geology and geophysics. *Rev. Geophys.*, 35(3):315–342. [doi:10.1029/97RG00221](https://doi.org/10.1029/97RG00221)
- Gupta, P., Noone, D., Galewsky, J., Sweeney, C., and Vaughn, B.H., 2009. Demonstration of high-precision continuous measurements of water vapor isotopologues in laboratory and remote field deployments using wave-length-scanned cavity ring-down spectroscopy (WS-CRDS) technology. *Rapid Commun. Mass Spectrom.*, 23(16):2534–2542. [doi:10.1002/rcm.4100](https://doi.org/10.1002/rcm.4100)
- Hagelberg, T., Shackleton, N., Pisias, N., and Shipboard Scientific Party, 1992. Development of composite depth sections for Sites 844 through 854. In Mayer, L., Pisias, N., Janecek, T., et al., *Proc. ODP, Init. Repts.*, 138: College Station, TX (Ocean Drilling Program), 67–77. [doi:10.2973/odp.proc.ir.138.105.1992](https://doi.org/10.2973/odp.proc.ir.138.105.1992)
- Hagelberg, T.K., Pisias, N.G., Shackleton, N.J., Mix, A.C., and Harris, S., 1995. Refinement of a high-resolution, continuous sedimentary section for studying equatorial Pacific Ocean paleoceanography, Leg 138. In Pisias, N.G., Mayer, L.A., Janecek, T.R., Palmer-Julson, A., and van Andel, T.H. (Eds.), *Proc. ODP, Sci Results*, 138: College Station, TX (Ocean Drilling Program), 31–46. [doi:10.2973/odp.proc.sr.138.103.1995](https://doi.org/10.2973/odp.proc.sr.138.103.1995)
- Harms, J.C., and Choquette, P.W., 1965. Geologic evaluation of a gamma-ray porosity device. *Trans. SPWLA Annu. Logging Symp.*: 6(2):C1–C37.
- Hayward, B.W., 2002. Late Pliocene to middle Pleistocene extinctions of deep-sea benthic foraminifera (“*Stilostomella* extinction”) in the southwest Pacific. *J. Foraminiferal Res.*, 32(3):274–307. [doi:10.2113/32.3.274](https://doi.org/10.2113/32.3.274)
- Herman, Y., 1971. Vertical and horizontal distribution of pteropods in Quaternary sequences. In Funnel, B.M., and Riedel, W.R. (Eds.), *The Micropaleontology of the Oceans*: Cambridge (Cambridge Univ. Press), 463–486.
- Hilgen, F.J., 1991. Extension of the astronomically calibrated (polarity) time scale to the Miocene/Pliocene boundary. *Earth Planet. Sci. Lett.*, 107(2):349–368. [doi:10.1016/0012-821X\(91\)90082-S](https://doi.org/10.1016/0012-821X(91)90082-S)
- Horai, K., and Von Herzen, R.P., 1985. Measurement of heat flow on Leg 86 of the Deep Sea Drilling Project. In Heath, G.R., Burckle, L.H., et al., *Init. Repts. DSDP*, 86: Washington, DC (U.S. Govt. Printing Office), 759–777. [doi:10.2973/dsdp.proc.86.135.1985](https://doi.org/10.2973/dsdp.proc.86.135.1985)
- Jiménez-Moreno, G., Fauquette, S., and Suc, J.-P., 2010. Miocene to Pliocene vegetation reconstruction and climate estimates in the Iberian Peninsula from pollen data. *Rev. Palaeobot. Palynol.*, 162(3):403–415. [doi:10.1016/j.revpalbo.2009.08.001](https://doi.org/10.1016/j.revpalbo.2009.08.001)
- Joannin, S., Bassinot, F., Combourieu Nebout, N., Peyron, O., and Beaudouin, C., 2011. Vegetation response to obliquity and precession forcing during the mid-Pleistocene transition in western Mediterranean region (ODP Site 976). *Quat. Sci. Rev.*, 30(3–4):280–297. [doi:10.1016/j.quascirev.2010.11.009](https://doi.org/10.1016/j.quascirev.2010.11.009)
- Kawagata, S., Hayward, B.W., Grenfell, H.R., and Sabaa, A., 2005. Mid-Pleistocene extinction of deep-sea foraminifera in the North Atlantic Gateway (ODP Sites 980 and 982). *Palaeogeogr., Palaeoclimatol., Palaeoecol.*, 221(3–4):267–291. [doi:10.1016/j.palaeo.2005.03.001](https://doi.org/10.1016/j.palaeo.2005.03.001)
- Kennett, J.P., and Srinivasan, M.S., 1983. *Neogene Planktonic Foraminifera: A Phylogenetic Atlas*: Stroudsburg, PA (Hutchinson Ross).
- Klejine, A., 1993. Morphology, taxonomy, and distribution of extant coccolithophorids (calcareous nannoplankton) [Ph.D. thesis]. Vrije Univ., Amsterdam.
- Knappertsbusch, M., Cortes, M.Y., and Thierstein, H.R., 1997. Morphologic variability of the coccolithophorid *Calcidiscus leptoporus* in the plankton, surface sedi-

- ments, and from the early Pleistocene. *Mar. Micropaleontol.*, 30(4):293–317. doi:10.1016/S0377-8398(96)00053-9
- Krijgsman, W., Gaboardi, S., Hilgen, F.J., Iaccarino, S., de Kaenel, E., and van der Laan, E., 2004. Revised astrochronology for the Ain el Beida section (Atlantic Morocco): no glacio-eustatic control for the onset of the Messinian salinity crisis. *Stratigraphy*, 1(1):87–101. <http://igitur-archive.library.uu.nl/geo/2006-0801-205238/UUindex.html>
- Kristiansen, J.I., 1982. The transient cylindrical probe method for determination of thermal parameters of earth materials [Ph.D. dissert.]. Århus Univ., Århus, Denmark.
- Kucera, M., 2007. Planktonic foraminifera as tracers of past oceanic environments. In Hillaire, M., and de Vernal, A. (Eds.), *Proxies in Late Cenozoic Paleooceanography*. Dev. Mar. Geol., 1:213–262. doi:10.1016/S1572-5480(07)01011-1
- Lézine, A.-M., and Denèfle, M., 1997. Enhanced anticyclonic circulation in the eastern North Atlantic during cold intervals of the last deglaciation inferred from deep-sea pollen records. *Geology*, 25(2):119–122. doi:10.1130/0091-7613(1997)025<0119:EACITE>2.3.CO;2
- Lisiecki, L.E., and Herbert, T.D., 2007. Automated composite depth scale construction and estimates of sediment core extension. *Paleoceanography*, 22(4):PA4213. doi:10.1029/2006PA001401
- Lisiecki, L.E., and Lisiecki, P.A., 2002. Application of dynamic programming to the correlation of paleoclimate records. *Paleoceanography*, 17(4):1049. doi:10.1029/2001PA000733
- Loeblich, A.R., and Tappan, H., 1988. *Foraminiferal Genera and Their Classification* (Vol. 2): New York (Van Nostrand Reinhold Co.).
- Lourens, L., Hilgen, F., Shackleton, N.J., Laskar, J., and Wilson, D., 2004. The Neogene period. In Gradstein, F.M., Ogg, J.G., and Smith, A. (Eds.), *A Geologic Time Scale 2004*: Cambridge (Cambridge Univ. Press), 409–440.
- Lovell, M.A., Harvey, P.K., Brewer, T.S., Williams, C., Jackson, P.D., and Williamson, G., 1998. Application of FMS images in the Ocean Drilling Program: an overview. In Cramp, A., MacLeod, C.J., Lee, S.V., and Jones, E.J.W. (Eds.), *Geological Evolution of Ocean Basins: Results from the Ocean Drilling Program*. Geol. Soc. Spec. Publ., 131(1):287–303. doi:10.1144/GSL.SP.1998.131.01.18
- Luthi, S.M., 1990. Sedimentary structures of clastic rocks identified from electrical borehole images. In Hurst, A., Lovell, M.A., and Morton, A.C. (Eds.), *Geological Applications of Wireline Logs*. Geol. Soc. Spec. Publ., 48(1):3–10. doi:10.1144/GSL.SP.1990.048.01.02
- Manheim, F.T., and Sayles, F.L., 1974. Composition and origin of interstitial waters of marine sediments, based on deep sea drill cores. In Goldberg, E.D. (Ed.), *The Sea* (Vol. 5): *Marine Chemistry: The Sedimentary Cycle*. New York (Wiley), 527–568.
- Margari, V., Skinner, L.C., Tzedakis, P.C., Ganopolski, A., Vautravers, M., and Shackleton, N.J., 2010. The nature of millennial-scale climate variability during the past two glacial periods. *Nat. Geosci.*, 3(2):127–131. doi:10.1038/ngeo740
- Martini, E., 1971. Standard Tertiary and Quaternary calcareous nannoplankton zonation. In Farinacci, A. (Ed.), *Proc. Second Planktonic Conf. Roma 1970*: Rome (Ed. Tecnosci.), 2:739–785.
- Mazzullo, J.M., Meyer, A., and Kidd, R.B., 1988. New sediment classification scheme for the Ocean Drilling Program. In Mazzullo, J.M., and Graham, A.G. (Eds.), *Handbook for shipboard sedimentologists*. ODP Tech. Note, 8:45–67. doi:10.2973/odp.tn.8.1988
- Mix, A.C., Tiedemann, R., Blum, P., et al., 2003. *Proc. ODP, Init. Repts.*, 202: College Station, TX (Ocean Drilling Program). doi:10.2973/odp.proc.ir.202.2003
- Munsell Color Company, Inc., 1994. *Munsell Soil Color Chart* (Revised ed.): Newburgh, MD (Munsell Color).
- Murray, J.W., 2006. *Ecology and Applications of Benthic Foraminifera*: Cambridge (Cambridge Univ. Press).
- Murray, R.W., Miller, D.J., and Kryc, K.A., 2000. Analysis of major and trace elements in rocks, sediments, and interstitial waters by inductively coupled plasma–atomic emission spectrometry (ICP-AES). *ODP Tech. Note*, 29. doi:10.2973/odp.tn.29.2000
- Narciso, A., Cachão, M., and de Abreu, L., 2006. *Coccolithus pelagicus* subsp. *pelagicus* versus *Coccolithus pelagicus* subsp. *braarudii* (Coccolithophore, Haptophyta): a proxy for surface subarctic Atlantic waters off Iberia during the last 200 kyr. *Mar. Micropaleontol.*, 59(1):15–34. doi:10.1016/j.marmicro.2005.12.001
- Naughton, F., Sánchez Goñi, M.F., Kageyama, M., Bard, E., Duprat, J., Cortijo, E., Desprat, S., Malaizé, B., Joly, C., Rostek, F., and Turon, J.-L., 2009. Wet to dry climatic trend in northwestern Iberia within Heinrich events. *Earth Planet. Sci. Lett.*, 284(3–4):329–342. doi:10.1016/j.epsl.2009.05.001
- Okada, H., and Bukry, D., 1980. Supplementary modification and introduction of code numbers to the low-latitude coccolith biostratigraphic zonation (Bukry, 1973; 1975). *Mar. Micropaleontol.*, 5:321–325. doi:10.1016/0377-8398(80)90016-X
- Paillard, D., Labeyrie, L., and Yiou, P., 1996. Macintosh program performs time-series analysis. *Eos, Trans. Am. Geophys. Union*, 77(39):379. doi:10.1029/96EO00259
- Parente, A., Cachão, M., Baumann, K.-H., de Abreu, L., and Ferreira, J., 2004. Morphometry of *Coccolithus pelagicus* s.l. (Coccolithophore, Haptophyta) from offshore Portugal, during the last 200 kyr. *Micropaleontology*, 50(1):107–120. doi:10.2113/50.Suppl\_1.107
- Perch-Nielsen, K., 1985. Cenozoic calcareous nannofossils. In Bolli, H.M., Saunders, J.B., and Perch-Nielsen, K. (Eds.), *Plankton Stratigraphy*: Cambridge (Cambridge Univ. Press), 427–554.
- Pribnow, D.F.C., Kinoshita, M., and Stein, C.A., 2000. *Thermal Data Collection and Heat Flow Recalculations for ODP Legs 101–180*: Hanover, Germany (Inst. Joint Geosci. Res., Inst. Geowiss. Gemeinschaftsauf. [GGA]). <http://www-odp.tamu.edu/publications/heatflow/ODPreprt.pdf>
- Quinn, P., Sáez, A., Baumann, K., Steel, B., Sprengel, C., and Medlin, L., 2004. Coccolithophorid biodiversity:

- evidence from the cosmopolitan species *Calcidiscus leptoporus*. In Thierstein, H.R., and Young, J.R. (Eds.), *Coccolithophores: From Molecular Processes to Global Impact*: Berlin (Springer), 299–326.
- Quinn, P., Thierstein, H.R., Brand, L., and Winter, A., 2003. Experimental evidence for the species character of *Calcidiscus leptoporus* morphotypes. *J. Paleontol.*, 77(5):825–830. doi:10.1666/0022-3360(2003)077<0825:EEFTSC>2.0.CO;2
- Raffi, I., Backman, J., Fornaciari, E., Pälike, H., Rio, D., Lourens, L., and Hilgen, F., 2006. A review of calcareous nannofossil astrobiochronology encompassing the past 25 million years. *Quat. Sci. Rev.*, 25(23–24):3113–3137. doi:10.1016/j.quascirev.2006.07.007
- Richter, C., Acton, G., Endris, C., and Radsted, M., 2007. Handbook for shipboard paleomagnetists. *ODP Tech. Note*, 34. doi:10.2973/odp.tn.34.2007
- Rider, M.H., 1996. *The Geological Interpretation of Well Logs* (2nd ed.): Caithness (Whittles Publ.).
- Rogerson, M., Rohling, E.J., Weaver, P.P.E., and Murray, J.W., 2004. The Azores Front since the Last Glacial Maximum. *Earth Planet. Sci. Lett.*, 222(3–4):779–789. doi:10.1016/j.epsl.2004.03.039
- Roucoux, K.H., Tzedakis, P.C., de Abreu, L., and Shackleton, N.J., 2006. Climate and vegetation changes 180,000 to 345,000 years ago recorded in a deep-sea core off Portugal. *Earth Planet. Sci. Lett.*, 249(3–4):307–325. doi:10.1016/j.epsl.2006.07.005
- Ruddiman, W.F., Kidd, R.B., Thomas, E., et al., 1987. *Init. Repts. DSDP*, 94: Washington, DC (U.S. Govt. Printing Office). doi:10.2973/dsdp.proc.94.1987
- Salgueiro, E., Voelker, A.H.L., de Abreu, L., Abrantes, F., Meggers, H., and Wefer, G., 2010. Temperature and productivity changes off the western Iberian margin during the last 150 ky. *Quat. Sci. Rev.*, 29(5–6):680–695. doi:10.1016/j.quascirev.2009.11.013
- Salimullah, A.R.M., and Stow, D.A.V., 1992. Application of FMS images in poorly recovered coring intervals: examples from ODP Leg 129. In Hurst, A., Griffiths, C.M., and Worthington, P.F. (Eds.), *Geological Application of Wireline Logs II*. Geol. Soc. Spec. Publ., 65(1):71–86. doi:10.1144/GSL.SP.1992.065.01.06
- Sánchez Goñi, M.F., Eynaud, F., Turon, J.L., and Shackleton, N.J., 1999. High-resolution palynological record off the Iberian margin: direct land-sea correlation for the last interglacial complex. *Earth Planet. Sci. Lett.*, 171(1):123–137. doi:10.1016/S0012-821X(99)00141-7
- Sánchez Goñi, M.F., Landais, A., Cacho, I., Duprat, J., and Rossignol, L., 2009. Contrasting intrainterstadial climatic evolution between high and middle North Atlantic latitudes: a close-up of Greenland Interstadials 8 and 12. *Geochem., Geophys., Geosyst.*, 10(4):Q04U04. doi:10.1029/2008GC002369
- Sánchez Goñi, M.F., Landais, A., Fletcher, W.J., Naughton, F., Desprat, S., and Duprat, J., 2008. Contrasting impacts of Dansgaard-Oeschger events over a western European latitudinal transect modulated by orbital parameters. *Quat. Sci. Rev.*, 27(11–12):1136–1151. doi:10.1016/j.quascirev.2008.03.003
- Sánchez Goñi, M.F., Turon, J.-L., Eynaud, F., and Gendreau, S., 2000. European climatic response to millennial-scale changes in the atmosphere–ocean system during the last glacial period. *Quat. Res.*, 54(3):394–403. doi:10.1006/qres.2000.2176
- Schiebel, R., Waniek, J., Zeltner, A., and Alves, M., 2002. Impact of the Azores Front on the distribution of planktic foraminifers, shelled gastropods, and coccolithophorids. *Deep-Sea Res., Part II*, 49(19):4035–4050. doi:10.1016/S0967-0645(02)00141-8
- Schlumberger, 1989. *Log Interpretation Principles/Applications*: Houston (Schlumberger Educ. Serv.), SMP-7017.
- Schlumberger, 1994. *IPL Integrated Porosity Lithology*: Houston (Schlumberger Wireline Testing), SMP-9270.
- Schönfeld, J., 1997. The impact of the Mediterranean Outflow Water (MOW) on benthic foraminiferal assemblages and surface sediments at the southern Portuguese continental margin. *Mar. Micropaleontol.*, 29(3–4):211–236. doi:10.1016/S0377-8398(96)00050-3
- Schönfeld, J., 2002. Recent benthic foraminiferal assemblages in deep high-energy environments from the Gulf of Cádiz (Spain). *Mar. Micropaleontol.*, 44(3–4):141–162. doi:10.1016/S0377-8398(01)00039-1
- Schönfeld, J., and Zahn, R., 2000. Late glacial to Holocene history of the Mediterranean Outflow. Evidence from benthic foraminiferal assemblages and stable isotopes at the Portuguese margin. *Palaeogeogr., Palaeoclimatol., Palaeoecol.*, 159(1–2):85–111. doi:10.1016/S0031-0182(00)00035-3
- Seeberg-Elverfeldt, J., Schlüter, M., Feseker, T., and Kölling, M., 2005. Rhizone sampling of porewaters near the sediment-water interface of aquatic systems. *Limnol. Oceanogr.: Methods*, 3(8):361–371.
- Serra, O., 1984. *Fundamentals of Well-Log Interpretation* (Vol. 1): *The Acquisition of Logging Data*: Amsterdam (Elsevier).
- Serra, O., 1986. *Fundamentals of Well-Log Interpretation* (Vol. 2): *The Interpretation of Logging Data*. Amsterdam (Elsevier).
- Serra, O., 1989. *Formation MicroScanner Image Interpretation*: Houston (Schlumberger Educ. Serv.), SMP-7028.
- Serrano, F., González-Donoso, J.M., and Linares, D., 1999. Biostratigraphy and paleoceanography of the Pliocene at Sites 975 (Menorca Rise) and 976 (Alboran Sea) from a quantitative analysis of the planktonic foraminiferal assemblages. In Zahn, R., Comas, M.C., and Klaus, A. (Eds.), *Proc. ODP, Sci. Results*, 161: College Station, TX (Ocean Drilling Program), 185–196. doi:10.2973/odp.proc.sr.161.239.1999
- Shipboard Scientific Party, 1995. Explanatory notes. In Flood, R.D., Piper, D.J.W., Klaus, A., et al., *Proc. ODP, Init. Repts.*, 155: College Station, TX (Ocean Drilling Program), 47–81. doi:10.2973/odp.proc.ir.155.104.1995
- Sierro, F.J., Flores, J.A., Civis, J., González-Delgado, J.A., and Francés, G., 1993. Late Miocene globorotaliid event-stratigraphy and biogeography in the NE-Atlantic and Mediterranean. *Mar. Micropaleontol.*, 21(1–3):143–167. doi:10.1016/0377-8398(93)90013-N
- Singh, A.D., Nisha, N.R., and Joydas, T.V., 2005. Distribution patterns of recent pteropods in surface sediments

- of the western continental shelf of India. *J. Micropaleontology*, 24(1):39–54. doi:10.1144/jm.24.1.39
- Steel, B.A., 2001. Physiology, growth, and morphometry of selected extant coccolithophorids, with particular reference to *Calcidiscus leptoporus* (Murray and Blackman, 1889) Loeblich and Tappan 1987 [M.S. thesis]. Univ. College London.
- Stow, D.A.V., 2005. *Sedimentary Rocks in the Field: A Colour Guide*: London (Manson Publ.).
- Suc, J.-P., 1984. Origin and evolution of the Mediterranean vegetation and climate in Europe. *Nature (London, U. K.)*, 307(5950):429–432. doi:10.1038/307429a0
- Traverse, A., 1988. *Paleopalynology*: Boston (Unwyn Hyman).
- Voelker, A.H.L., Lebreiro, S.M., Schönfeld, J., Cacho, I., Erlenkeuser, H., and Abrantes, F., 2006. Mediterranean Outflow strengthening during Northern Hemisphere coolings: a salt source for the glacial Atlantic? *Earth Planet. Sci. Lett.*, 245(1–2):39–55. doi:10.1016/j.epsl.2006.03.014
- Von Herzen, R.P., and Maxwell, A.E., 1959. The measurement of thermal conductivity of deep-sea sediments by a needle-probe method. *J. Geophys. Res.*, 64(10):1557–1563. doi:10.1029/JZ064i010p01557
- Weaver, P.P.E., and Clement, B.M., 1987. Magnetobiostratigraphy of planktonic foraminiferal datums: Deep Sea Drilling Project Leg 94, North Atlantic. In Ruddiman, W.F., Kidd, R.B., Thomas, E., et al., *Init. Repts. DSDP, 94*: Washington (U.S. Govt. Printing Office), 815–829. doi:10.2973/dsdp.proc.94.120.1987
- Wentworth, C.K., 1922. A scale of grade and class terms for clastic sediments. *J. Geol.*, 30(5):377–392. doi:10.1086/622910
- Whatley, R., and Coles, G., 1987. The late Miocene to Quaternary Ostracoda of Leg 94, Deep Sea Drilling Project. *Rev. Esp. Micropaleontol.*, 19:33–97.
- Yasuhara, M., Cronin, T.M., Hunt, G., and Hodell, D.A., 2009a. Deep-sea ostracods from the south Atlantic sector of the Southern Ocean during the last 370,000 years. *J. Paleontol.*, 83(6):914–930. doi:10.1666/08-149.1
- Yasuhara, M., Okahashi, H., and Cronin, T.M., 2009b. Taxonomy of Quaternary deep-sea ostracods from the western North Atlantic Ocean. *Palaeontology*, 52(4):879–931. doi:10.1111/j.1475-4983.2009.00888.x

**Publication:** 17 June 2013  
**MS 339-102**

Figure F1. Schematic of the advanced piston coring system used during Expedition 339. ID = inner diameter.

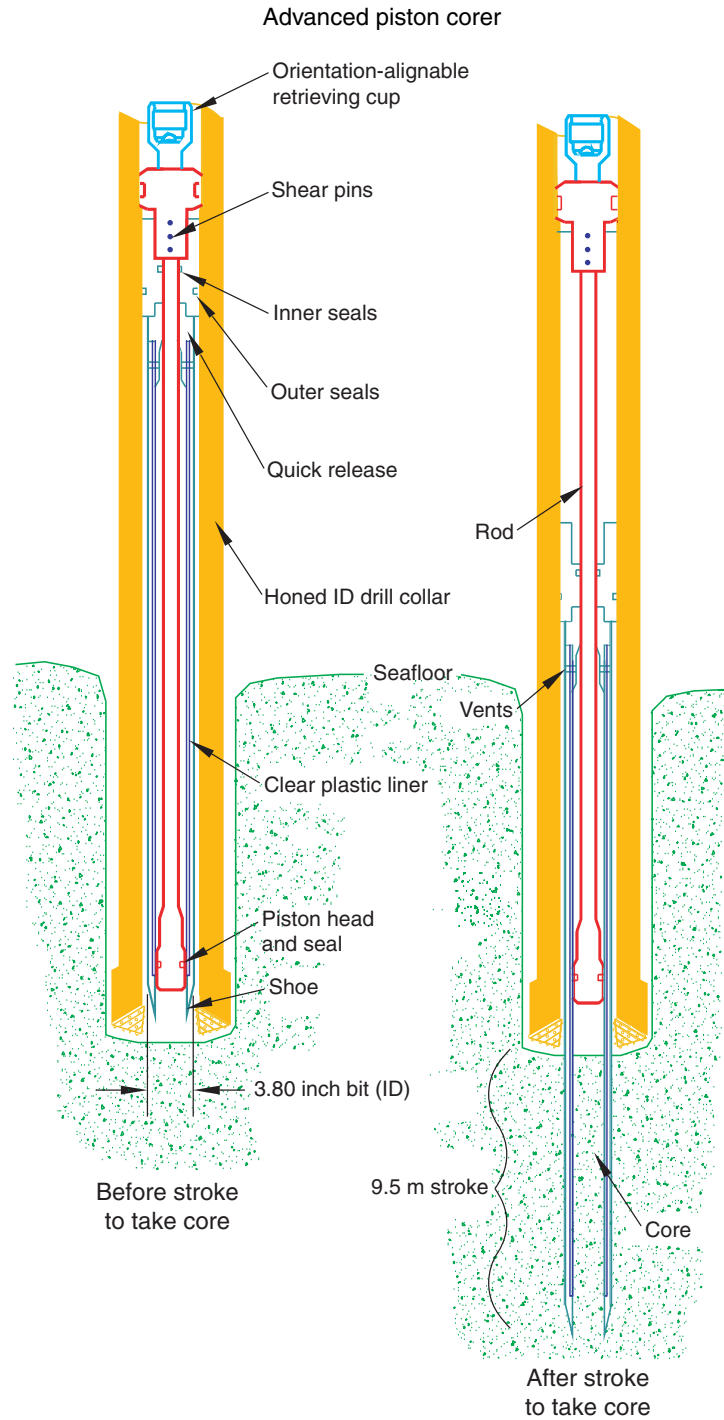
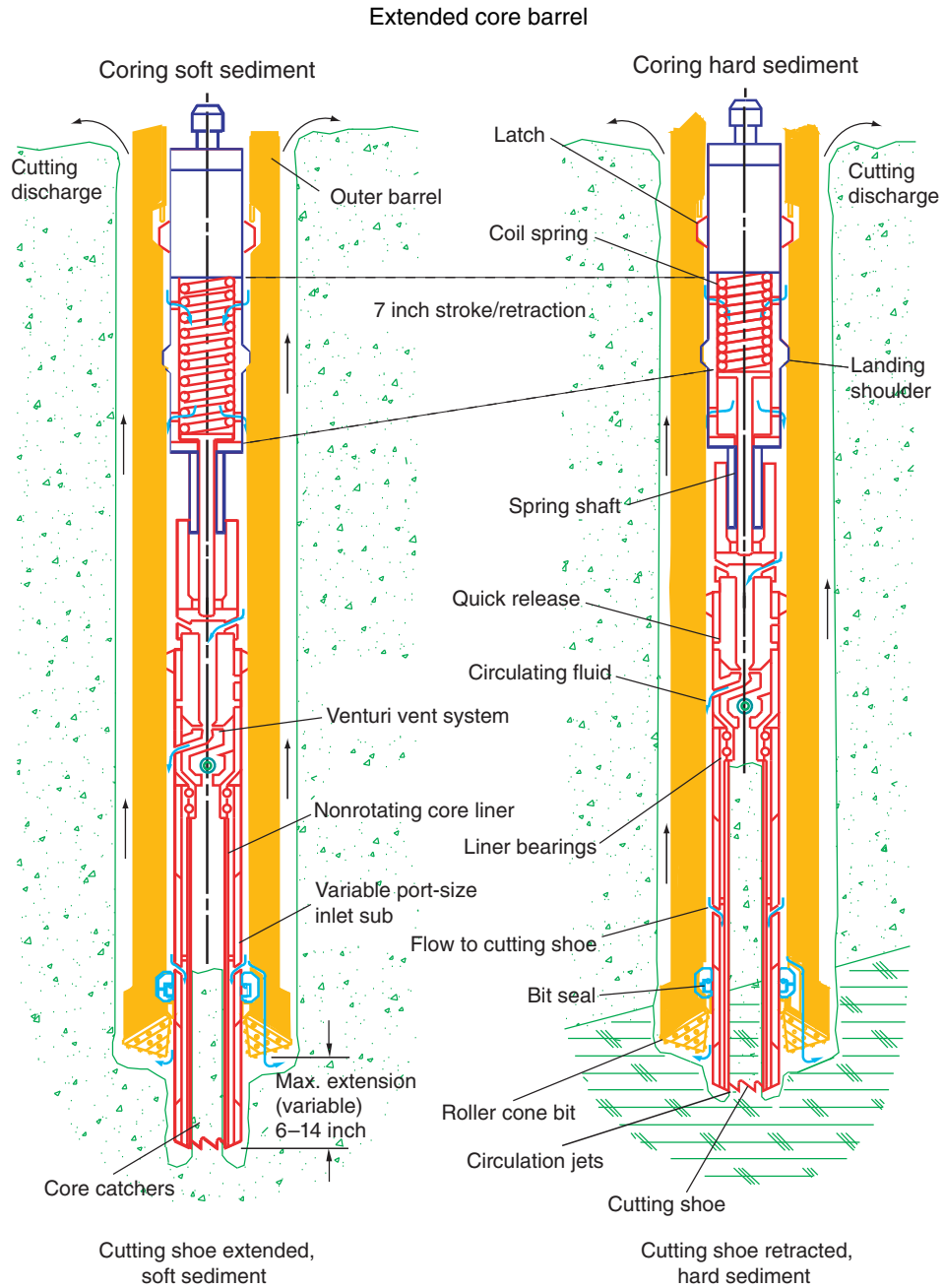
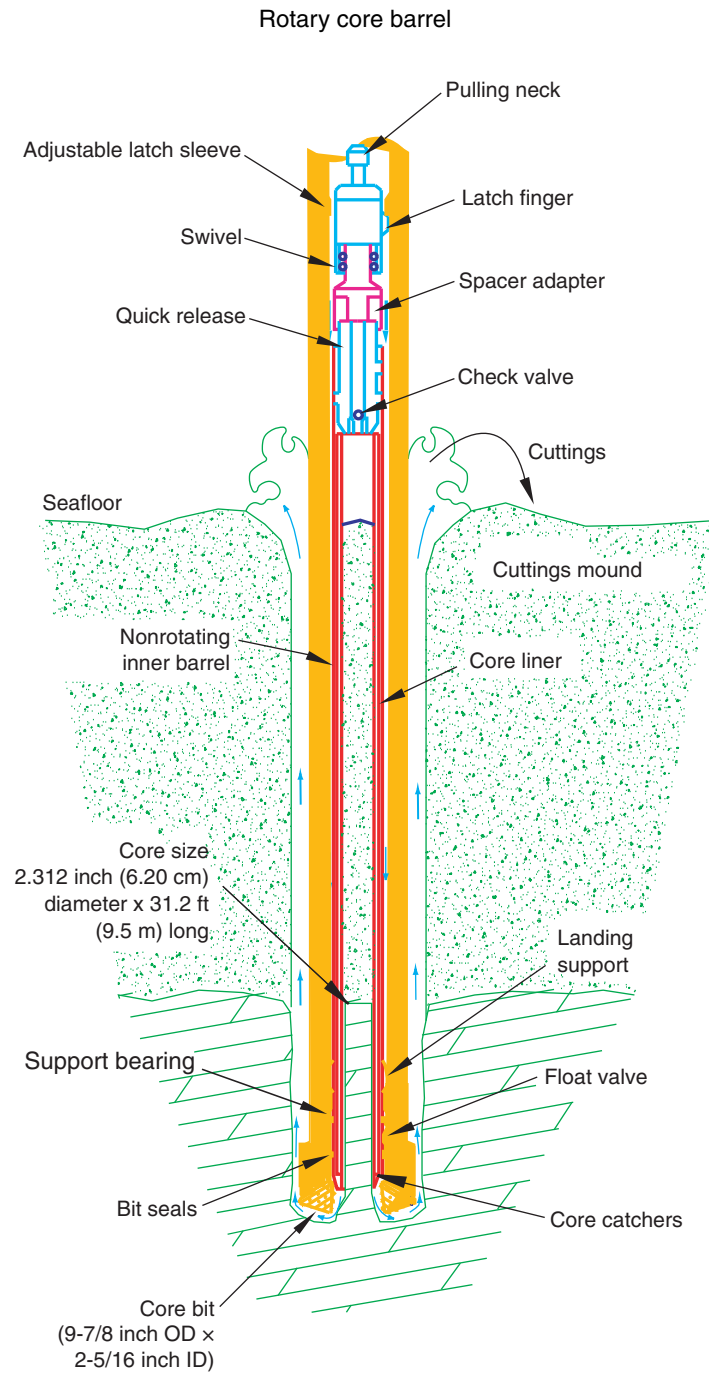


Figure F2. Schematic of the extended core barrel system used during Expedition 339.



**Figure F3.** Schematic of the rotary core barrel system used during Expedition 339. ID = inner diameter, OD = outer diameter.



**Figure F4.** Siliciclastic–biogenic, carbonate–biogenic silica ternary diagram used during Expedition 339 for sediment names of different compositions.

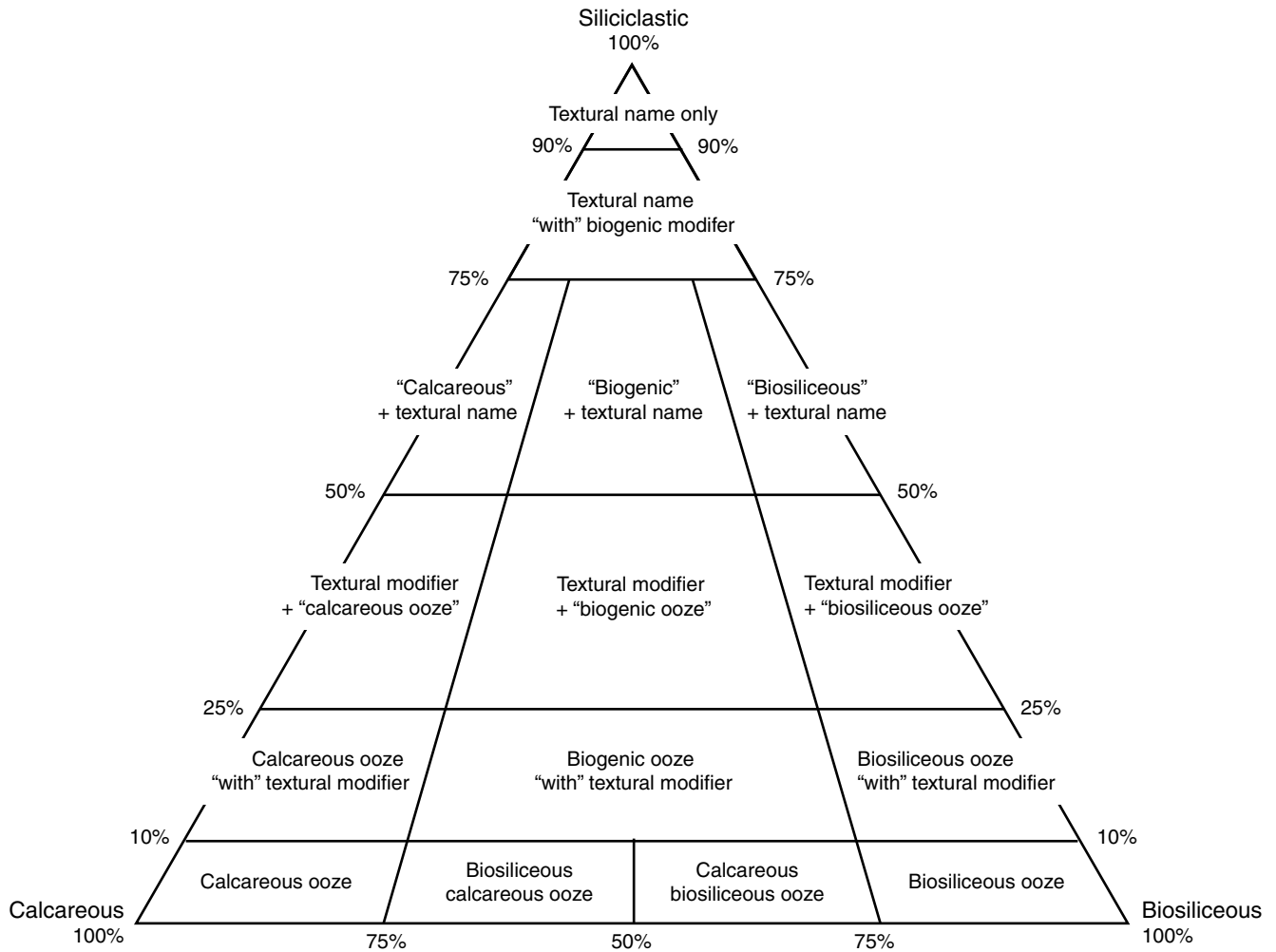


Figure F5. Sand-silt-clay ternary diagram used during Expedition 339 for textural names.



Figure F6. Example visual core description sheet, Expedition 339.

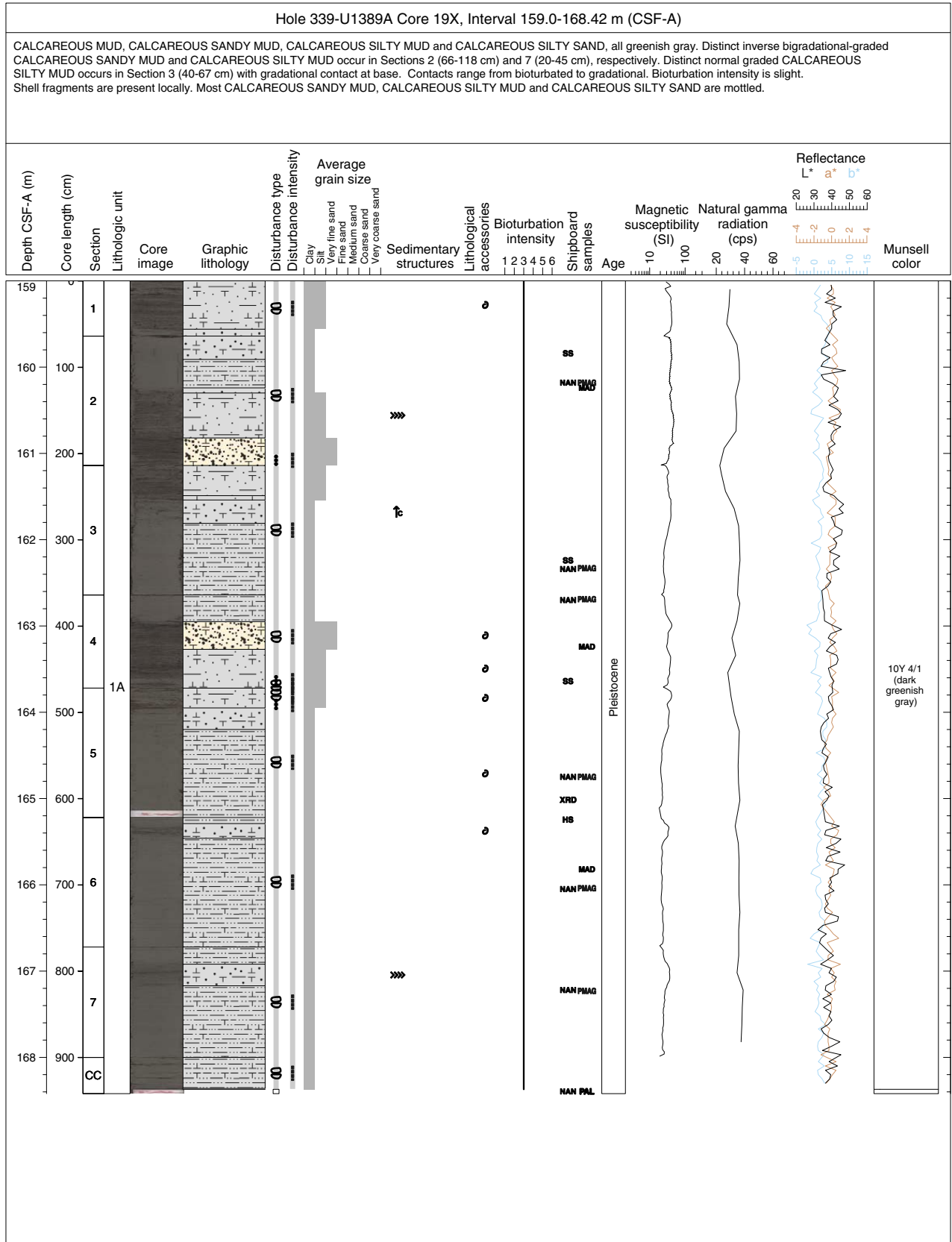


Figure F7. Graphic keys for visual core description sheets, Expedition 339. A. Lithology patterns. (Continued on next page.)

**A** Lithology

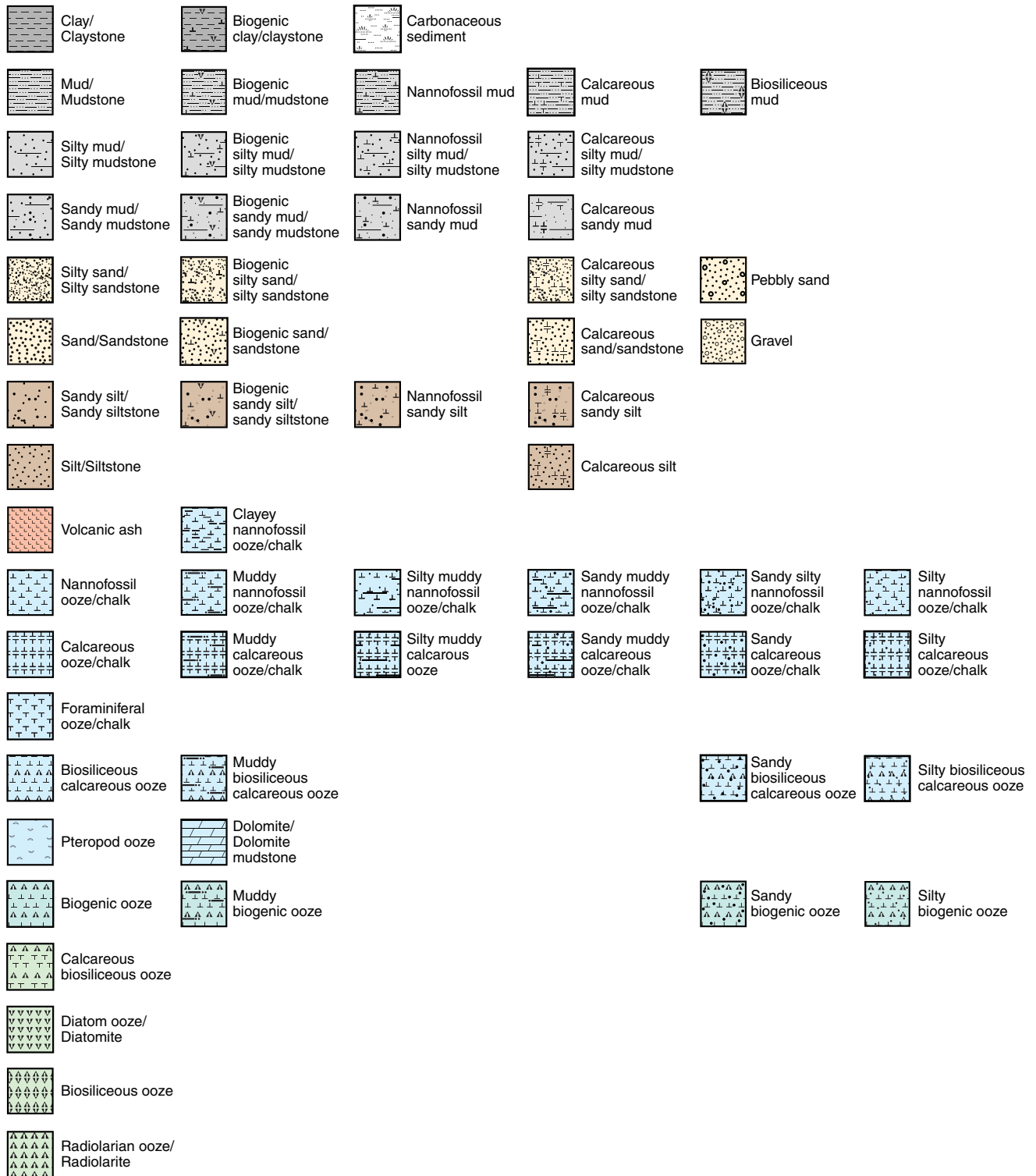


Figure F7 (continued). B. Sedimentary structure, bedding, and bioturbation symbols.

**B Sedimentary structures**

Horizontal stratification/ Parallel stratification	Climbing ripple cross- stratification	<b>Other sedimentary features</b>	<b>Layer or bedding thickness</b>
Nonparallel stratification	Wavy strata/Laminations	Interference ripples	<b>ThB</b> Thin bed/Very thin bed
Cross bedding	Bigradational bedding	Sole marks/Flute clast/ Tool mark/Bottom cast/ Load cast	<b>MB</b> Medium bed
Interstratification/ Parallel lamination	Lens/Pod/Patch/Bleb	Mud crack /Desiccation cracks	<b>TkB</b> Thick bed/Very thick bed
Color banding	Mud drape	Wave ripples	<b>ThL</b> Thin lamination
Tilted bedding	Normal grading /Fining upward	Liquefaction/Pipe and dish /Fluid escape structures	<b>ML</b> Medium lamination
Lenticular bedding/ Flaser bedding	Inverse grading /Coarsening upward	Ball and pillow	<b>TkL</b> Thick lamination
Grain packing layer/ Grain size layering/ Grain composition layering	Massive bedding	Current ripple mark/Ripple	<b>Deformational structures:</b>
Grain orientation layering /Imbrication		Convolute bedding	Synsedimentary deformation
		Flame structure	Fault breccia
			Fault
			Contorted strata

**Bioturbation intensity**

1 Absent	3 Slight	5 Heavy
2 Sparse	4 Moderate	6 Complete

**Lithologic accessories**

Shell fragments/ Other macrofossils	Cement	Nodule/Concretion
--	--------	-------------------

**Drilling disturbances**

Biscuit	Gas expansion	Flow-in/Along-core gravel/Sand contamination	<b>Intensity of disturbance</b>
Brecciated	Fragmented	Fall-in	Slightly disturbed
Mousselike	Bowed	Slurry	Moderately disturbed
Washed gravel	Fractured/Cracked	Void	Heavily disturbed
Soupy	Puncture		Destroyed

**Shipboard sampling**

<b>SS</b> Smear slide	<b>MBIO</b> Microbiology	<b>IW</b> Interstitial water	<b>TS</b> Thin section
<b>CRB</b> Carbonate	<b>NAN</b> Nannofossil	<b>IWs</b> Interstitial water, syringe	<b>HS</b> Headspace
<b>XRD</b> X-ray diffraction	<b>PAL</b> Micropaleontology	<b>PMAG</b> Paleomagnetic	<b>MAD</b> Moisture/Density



Figure F8. Example of a drafted (mechanically drawn) hand-drawn log of Sections 339-U1386A-1H-1 through 12H-5.

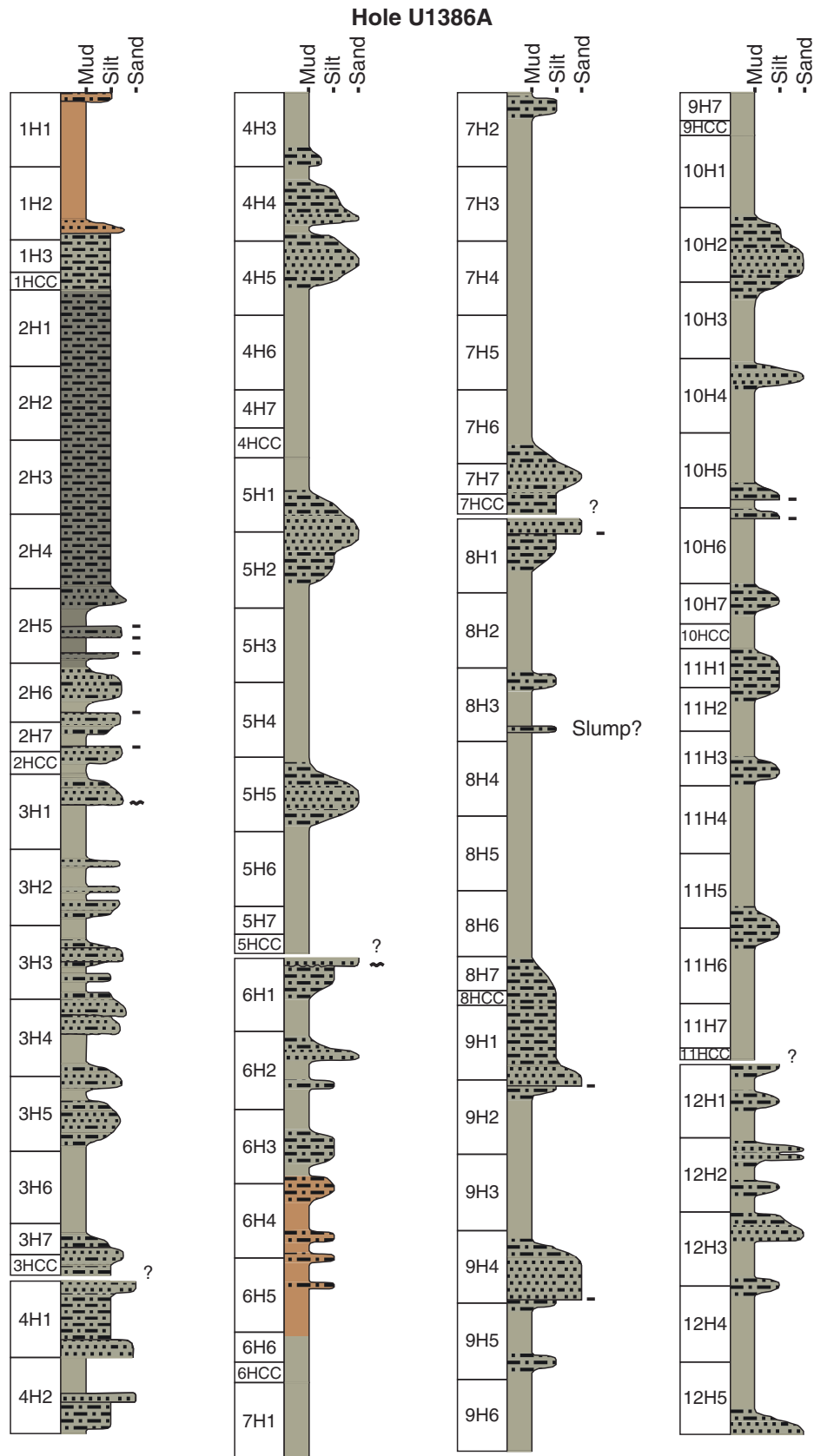


**Figure F9.** Graphic key for Site U1386 drafted (mechanically drawn) hand-drawn logs. Legends may vary slightly between sites.

### Patterns

	Nannofossil mud
	Calcareous silty mud
	Sandy silt/Sandy mud
	Silty bioclastic sand
	Debrite
	Contorted strata/Slump
	Granules/Pebbles
	Bioturbation
	Shell fragment
	Shell
	Plant/Wood debris
	Parallel lamination
	Cross-lamination
	Sharp contact
	Bioturbated/Gradational contact
	Irregular contact
	Erosional contact

### Colors

	Grayish brown/Reddish (2.5Y 3/1, 2.5Y 4/2, 10YR 5/1, 10YR 6/1)
	Greenish gray/Dark greenish gray/Olive-gray (5GY 4/1, 5Y 4/1, 5Y 4/2, 10Y 4/1, 10Y 5/1, 10GY 4/1)
	Very dark greenish gray (10Y 3/1)
	Dark gray/Very dark gray (N 4/1, N 3/1)

**Figure F10.** Plot of X-ray intensity of calcite + dolomite peaks versus percent  $\text{CaCO}_3$  determined by COUL carbonate analysis, Expedition 339.

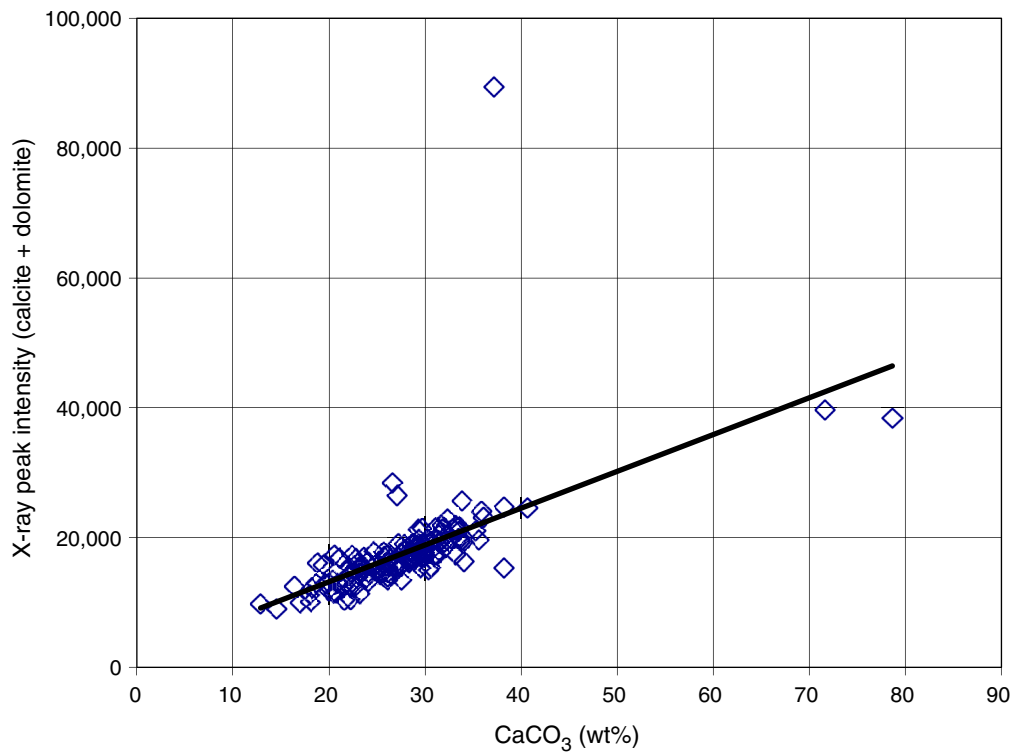


**Figure F11.** Correlation of geomagnetic polarity timescale (Lourens et al., 2004), biostratigraphic zonation, and biohorizons used during Expedition 339. Magnetic polarity: n = normal, r = reversed. Datum: FO = first occurrence, LO = last occurrence, LcO = last common occurrence, LrO = last regular occurrence, AB = acme bottom, FcO = first common occurrence, LaO = last abundant occurrence, FaO = first abundant occurrence, T = top, B = bottom, s = sinistral, d = dextral.

Age (Ma)	Magnetic polarity	Calcareous nannofossils			Planktonic foraminifers																																								
		Zone Okada and Bukry (1980)	Zone Martini (1971)	Datum	Datum	Berggren et al. (1995)																																							
1	Pleistocene C1	n	Brunhes	Matuyama	CN15	NN21	LrO <i>Emiliana huxleyi</i> >4 µm (0.01)	PT1																																					
					b	NN20	FO <i>Emiliana huxleyi</i> (0.26)																																						
					a		LO <i>Pseudoemiliana lacunosa</i> (0.46)																																						
					Jaramillo	NN19	LO <i>Reticulofenestra asanoi</i> (0.90)																																						
							Reentrance medium <i>Gephyrocapsa</i> + FO <i>Geph. sp. 3</i> (1.007)																																						
							FO <i>Reticulofenestra asanoi</i> (1.07)																																						
							LO large <i>Gephyrocapsa</i> (1.24)																																						
							LO <i>Helicosphaera sellii</i> (1.25)																																						
					Olduvai	NN13	FcO large <i>Gephyrocapsa</i> (1.46)																																						
							FO large <i>Gephyrocapsa</i> (1.61)																																						
LO <i>Calcidiscus macintyrei</i> (1.66)																																													
FO medium <i>Gephyrocapsa</i> (1.68)																																													
LO <i>Discoaster brouweri</i> (1.95)																																													
2	Pleistocene C2	r	Matuyama	Matuyama	d	NN18	AB <i>Discoaster triradiatus</i> (2.13)	PL6																																					
					c	NN17	LO <i>Discoaster pentaradiatus</i> (2.39)																																						
					b		LO <i>Discoaster surculus</i> (2.53)																																						
					Kaena	NN16	LO <i>Discoaster tamalis</i> (2.8)																																						
							Mammoth		Gauss	CN12	a	LO <i>Sphenolithus</i> spp. (3.52)																																	
												C2A	n	Gauss	CN11	a	b	NN15/14	LO <i>Reticulofenestra pseudoumbilicus</i> (3.81)																										
																	FcO <i>Discoaster asymmetricus</i> (4.12)																												
																	Cochiti	NN13	LO <i>Amaurolithus primus</i> (4.5)																										
					Nunivak	c													NN10	b	LO <i>Ceratolithus acutus</i> (5.04)																								
							FO <i>Ceratolithus rugosus</i> (5.05)																																						
LO <i>Triquetrorhabdulus rugosus</i> (5.27)																																													
FO <i>Ceratolithus acutus</i> (5.34)																																													
LO <i>Discoaster quinqueramus</i> (5.54)																																													
3	Pliocene late	n	Brunhes	Gauss	CN10	a	NN12	c	NN11	a	NN11	FO <i>Amaurolithus</i> spp. (7.36)	M14																																
														C3	r	Gilbert	CN9	a	A	NN11	FO <i>Amaurolithus</i> spp. (7.36)																								
																						C3A	n	Gilbert	CN9	a	A	NN11	FO <i>Amaurolithus</i> spp. (7.36)																
																														C3B	r	Gilbert	CN9	a	A	NN11	FO <i>Amaurolithus</i> spp. (7.36)								
																																						C4	n	Gilbert	CN9	a	A	NN11	FO <i>Amaurolithus</i> spp. (7.36)
														C3B	r	Gilbert	CN9	a	A	NN11	FO <i>Amaurolithus</i> spp. (7.36)																								
																						C4	n	Gilbert	CN9	a	A	NN11	FO <i>Amaurolithus</i> spp. (7.36)																
																														C3A	n	Gilbert	CN9	a	A	NN11	FO <i>Amaurolithus</i> spp. (7.36)								
																																						C3B	r	Gilbert	CN9	a	A	NN11	FO <i>Amaurolithus</i> spp. (7.36)
C4	n	Gilbert	CN9	a	A	NN11	FO <i>Amaurolithus</i> spp. (7.36)																																						
								C3A	n	Gilbert	CN9	a	A	NN11	FO <i>Amaurolithus</i> spp. (7.36)																														
																C3B	r	Gilbert	CN9	a	A	NN11	FO <i>Amaurolithus</i> spp. (7.36)																						
																								C4	n	Gilbert	CN9	a	A	NN11	FO <i>Amaurolithus</i> spp. (7.36)														
																																C3A	n	Gilbert	CN9	a	A	NN11	FO <i>Amaurolithus</i> spp. (7.36)						
C3B	r	Gilbert	CN9	a	A	NN11	FO <i>Amaurolithus</i> spp. (7.36)																																						
								C4	n	Gilbert	CN9	a	A	NN11	FO <i>Amaurolithus</i> spp. (7.36)																														
																C3A	n	Gilbert	CN9	a	A	NN11	FO <i>Amaurolithus</i> spp. (7.36)																						
																								C3B	r	Gilbert	CN9	a	A	NN11	FO <i>Amaurolithus</i> spp. (7.36)														
																																C4	n	Gilbert	CN9	a	A	NN11	FO <i>Amaurolithus</i> spp. (7.36)						
C3A	n	Gilbert	CN9	a	A	NN11	FO <i>Amaurolithus</i> spp. (7.36)																																						
								C3B	r	Gilbert	CN9	a	A	NN11	FO <i>Amaurolithus</i> spp. (7.36)																														
																C4	n	Gilbert	CN9	a	A	NN11	FO <i>Amaurolithus</i> spp. (7.36)																						
																								C3A	n	Gilbert	CN9	a	A	NN11	FO <i>Amaurolithus</i> spp. (7.36)														
																																C3B	r	Gilbert	CN9	a	A	NN11	FO <i>Amaurolithus</i> spp. (7.36)						
C4	n	Gilbert	CN9	a	A	NN11	FO <i>Amaurolithus</i> spp. (7.36)																																						
								C3A	n	Gilbert	CN9	a	A	NN11	FO <i>Amaurolithus</i> spp. (7.36)																														
																C3B	r	Gilbert	CN9	a	A	NN11	FO <i>Amaurolithus</i> spp. (7.36)																						
																								C4	n	Gilbert	CN9	a	A	NN11	FO <i>Amaurolithus</i> spp. (7.36)														
																																C3A	n	Gilbert	CN9	a	A	NN11	FO <i>Amaurolithus</i> spp. (7.36)						
C3B	r	Gilbert	CN9	a	A	NN11	FO <i>Amaurolithus</i> spp. (7.36)																																						
								C4	n	Gilbert	CN9	a	A	NN11	FO <i>Amaurolithus</i> spp. (7.36)																														
																C3A	n	Gilbert	CN9	a	A	NN11	FO <i>Amaurolithus</i> spp. (7.36)																						
																								C3B	r	Gilbert	CN9	a	A	NN11	FO <i>Amaurolithus</i> spp. (7.36)														
																																C4	n	Gilbert	CN9	a	A	NN11	FO <i>Amaurolithus</i> spp. (7.36)						
C3A	n	Gilbert	CN9	a	A	NN11	FO <i>Amaurolithus</i> spp. (7.36)																																						
								C3B	r	Gilbert	CN9	a	A	NN11	FO <i>Amaurolithus</i> spp. (7.36)																														
																C4	n	Gilbert	CN9	a	A	NN11	FO <i>Amaurolithus</i> spp. (7.36)																						
																								C3A	n	Gilbert	CN9	a	A	NN11	FO <i>Amaurolithus</i> spp. (7.36)														
																																C3B	r	Gilbert	CN9	a	A	NN11	FO <i>Amaurolithus</i> spp. (7.36)						
C4	n	Gilbert	CN9	a	A	NN11	FO <i>Amaurolithus</i> spp. (7.36)																																						
								C3A	n	Gilbert	CN9	a	A	NN11	FO <i>Amaurolithus</i> spp. (7.36)																														
																C3B	r	Gilbert	CN9	a	A	NN11	FO <i>Amaurolithus</i> spp. (7.36)																						
																								C4	n	Gilbert	CN9	a	A	NN11	FO <i>Amaurolithus</i> spp. (7.36)														
																																C3A	n	Gilbert	CN9	a	A	NN11	FO <i>Amaurolithus</i> spp. (7.36)						
C3B	r	Gilbert	CN9	a	A	NN11	FO <i>Amaurolithus</i> spp. (7.36)																																						
								C4	n	Gilbert	CN9	a	A	NN11	FO <i>Amaurolithus</i> spp. (7.36)																														
																C3A	n	Gilbert	CN9	a	A	NN11	FO <i>Amaurolithus</i> spp. (7.36)																						
																								C3B	r	Gilbert	CN9	a	A	NN11	FO <i>Amaurolithus</i> spp. (7.36)														
																																C4	n	Gilbert	CN9	a	A	NN11	FO <i>Amaurolithus</i> spp. (7.36)						
C3A	n	Gilbert	CN9	a	A	NN11	FO <i>Amaurolithus</i> spp. (7.36)																																						
								C3B	r	Gilbert	CN9	a	A	NN11	FO <i>Amaurolithus</i> spp. (7.36)																														
																C4	n	Gilbert	CN9	a	A	NN11	FO <i>Amaurolithus</i> spp. (7.36)																						
																								C3A	n	Gilbert	CN9	a	A	NN11	FO <i>Amaurolithus</i> spp. (7.36)														
																																C3B	r	Gilbert	CN9	a	A	NN11	FO <i>Amaurolithus</i> spp. (7.36)						
C4	n	Gilbert	CN9	a	A	NN11	FO <i>Amaurolithus</i> spp. (7.36)																																						
								C3A	n	Gilbert	CN9	a	A	NN11	FO <i>Amaurolithus</i> spp. (7.36)																														
																C3B	r	Gilbert	CN9	a	A	NN11	FO <i>Amaurolithus</i> spp. (7.36)																						
																								C4	n	Gilbert	CN9	a	A	NN11	FO <i>Amaurolithus</i> spp. (7.36)														
																																C3A	n	Gilbert	CN9	a	A	NN11	FO <i>Amaurolithus</i> spp. (7.36)						
C3B	r	Gilbert	CN9	a	A	NN11	FO <i>Amaurolithus</i> spp. (7.36)																																						
								C4	n	Gilbert	CN9	a	A	NN11	FO <i>Amaurolithus</i> spp. (7.36)																														
																C3A	n	Gilbert	CN9	a	A	NN11	FO <i>Amaurolithus</i> spp. (7.36)																						
																								C3B	r	Gilbert	CN9	a	A	NN11	FO <i>Amaurolithus</i> spp. (7.36)														
																																C4	n	Gilbert	CN9	a	A	NN11	FO <i>Amaurolithus</i> spp. (7.36)						
C3A	n	Gilbert	CN9	a	A	NN11	FO <i>Amaurolithus</i> spp. (7.36)																																						
								C3B	r	Gilbert	CN9	a	A	NN11	FO <i>Amaurolithus</i> spp. (7.36)																														
																C4	n	Gilbert	CN9	a	A	NN11	FO <i>Amaurolithus</i> spp. (7.36)																						
																								C3A	n	Gilbert	CN9	a	A	NN11	FO <i>Amaurolithus</i> spp. (7.36)														
																																C3B	r	Gilbert	CN9	a	A	NN11	FO <i>Amaurolithus</i> spp. (7.36)						
C4	n	Gilbert	CN9	a	A	NN11	FO <i>Amaurolithus</i> spp. (7.36)																																						
								C3A	n	Gilbert	CN9	a	A	NN11	FO <i>Amaurolithus</i> spp. (7.36)																														
																C3B	r	Gilbert	CN9	a	A	NN11	FO <i>Amaurolithus</i> spp. (7.36)																						
																								C4	n	Gilbert	CN9	a	A	NN11	FO <i>Amaurolithus</i> spp. (7.36)														
																																C3A	n	Gilbert	CN9	a	A	NN11	FO <i>Amaurolithus</i> spp. (7.36)						
C3B	r	Gilbert	CN9	a	A	NN11	FO <i>Amaurolithus</i> spp. (7.36)																																						
								C4	n	Gilbert	CN9	a	A	NN11	FO <i>Amaurolithus</i> spp. (7.36)																														
																C3A	n	Gilbert	CN9	a	A	NN11	FO <i>Amaurolithus</i> spp. (7.36)																						
																								C3B	r	Gilbert	CN9	a	A	NN11	FO <i>Amaurolithus</i> spp. (7.36)														
																																C4	n	Gilbert	CN9	a	A	NN11	FO <i>Amaurolithus</i> spp. (7.36)						
C3A	n	Gilbert	CN9	a	A	NN11	FO <i>Amaurolithus</i> spp. (7.36)																																						
								C3B	r	Gilbert	CN9	a	A	NN11	FO <i>Amaurolithus</i> spp. (7.36)																														
																C4	n	Gilbert	CN9	a	A	NN11	FO <i>Amaurolithus</i> spp. (7.36)																						
																								C3A	n	Gilbert	CN9	a	A	NN11	FO <i>Amaurolithus</i> spp. (7.36)														
																																C3B	r	Gilbert	CN9	a	A	NN11	FO <i>Amaurolithus</i> spp. (7.36)						
C4	n	Gilbert	CN9	a	A	NN11	FO <i>Amaurolithus</i> spp. (7.36)																																						
								C3A	n	Gilbert	CN9	a	A	NN11	FO <i>Amaurolithus</i> spp. (7.36)																														
																C3B	r	Gilbert	CN9	a	A	NN11	FO <i>Amaurolithus</i> spp. (7.36)																						
																								C4	n	Gilbert	CN9	a	A	NN11	FO <i>Amaurolithus</i> spp. (7.36)														
																																C3A	n	Gilbert	CN9	a	A	NN11	FO <i>Amaurolithus</i> spp. (7.36)						
C3B	r	Gilbert	CN9	a	A	NN11	FO <i>Amaurolithus</i> spp. (7.36)																																						
								C4	n	Gilbert	CN9	a	A	NN11	FO <i>Amaurolithus</i> spp. (7.36)																														
																C3A	n	Gilbert	CN9	a	A	NN11	FO <i>Amaurolithus</i> spp. (7.36)																						
																								C3B	r	Gilbert	CN9	a	A	NN11	FO <i>Amaurolithus</i> spp. (7.36)														
																																C4	n	Gilbert	CN9	a	A	NN11	FO <i>Amaurolithus</i> spp. (7.36)						
C3A	n																																												

**Figure F12.** Diagram of interstitial water sampling plan. High-resolution interstitial water (IW) sampling at Sites U1385, U1386, U1389, and U1391 included syringe (IWSy) and whole-round (WRND) samples. Low-resolution sampling at Sites U1387, U1388, and U1390 consisted of IW samples only.

All cores

- Upper 50 mbsf: IWSy (1/2 of 50 cm<sup>3</sup> syringe), length = 5 cm, bottom of Section 1–4 or 5.
- 50–150 mbsf: IWSy (50 cm<sup>3</sup> syringe), length = 10 cm, bottom of Section 1–4 or 5.
- 0–200 mbsf: IW (5 cm WR), bottom of Section 5 or 6.

IWSy entry	IW (WR) entry
Sample type = CYL	Sample type = WRND
Sample tool = SYRINGE	Sample tool = SPATULA
Test = IW	Test = IW
Name = IWSy(interval)	Name = IW(interval)
Volume = 25 or 50 cm <sup>3</sup>	Volume = 176 cm <sup>3</sup>

IW(WR) bottom 5 or 10 cm, Section 6 or 7.

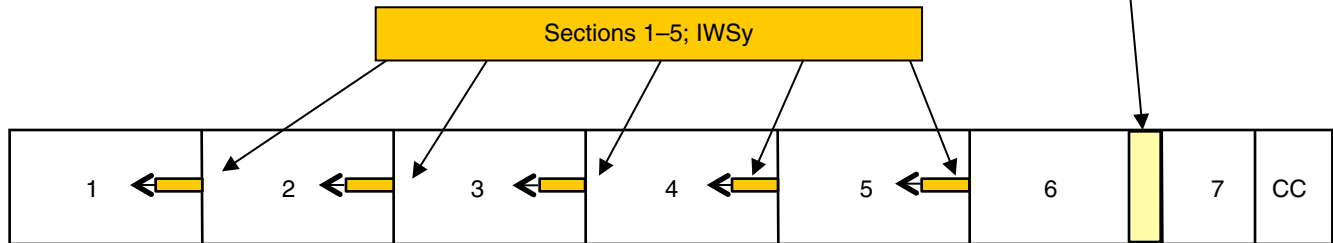


**Figure F13.** Plot of measured and normalized  $\delta^{18}\text{O}$  results of internal seawater standard analyzed every other sample to correct for instrument drift. Standard deviation ( $1\sigma$ ) of normalized  $\delta^{18}\text{O}$  is  $\pm 0.2\text{‰}$ . S = time of autosampler septum change, PO = power outage.

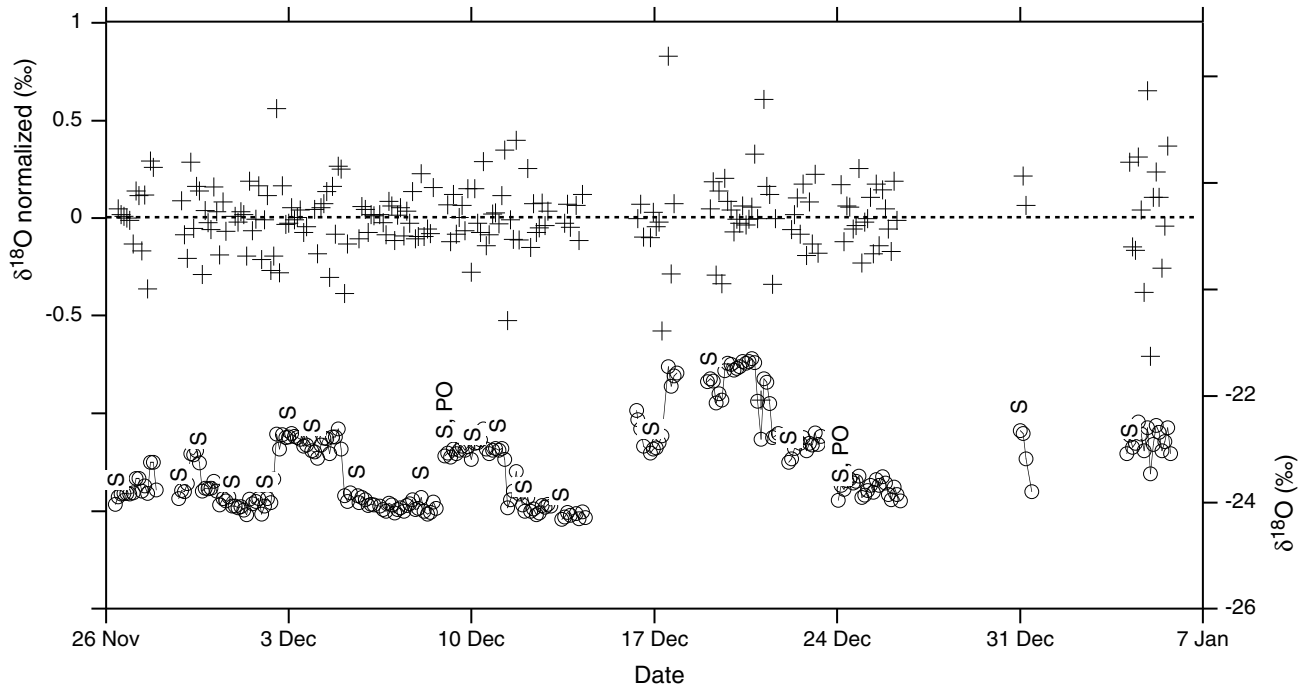


**Figure F14.** Plot of measured and normalized  $\delta D$  results of the internal seawater standard analyzed every other sample to correct for instrument drift. The standard deviation ( $1\sigma$ ) of normalized  $\delta D$  is  $\pm 0.6\text{‰}$ . S = time of autosampler septum change, PO = power outage.

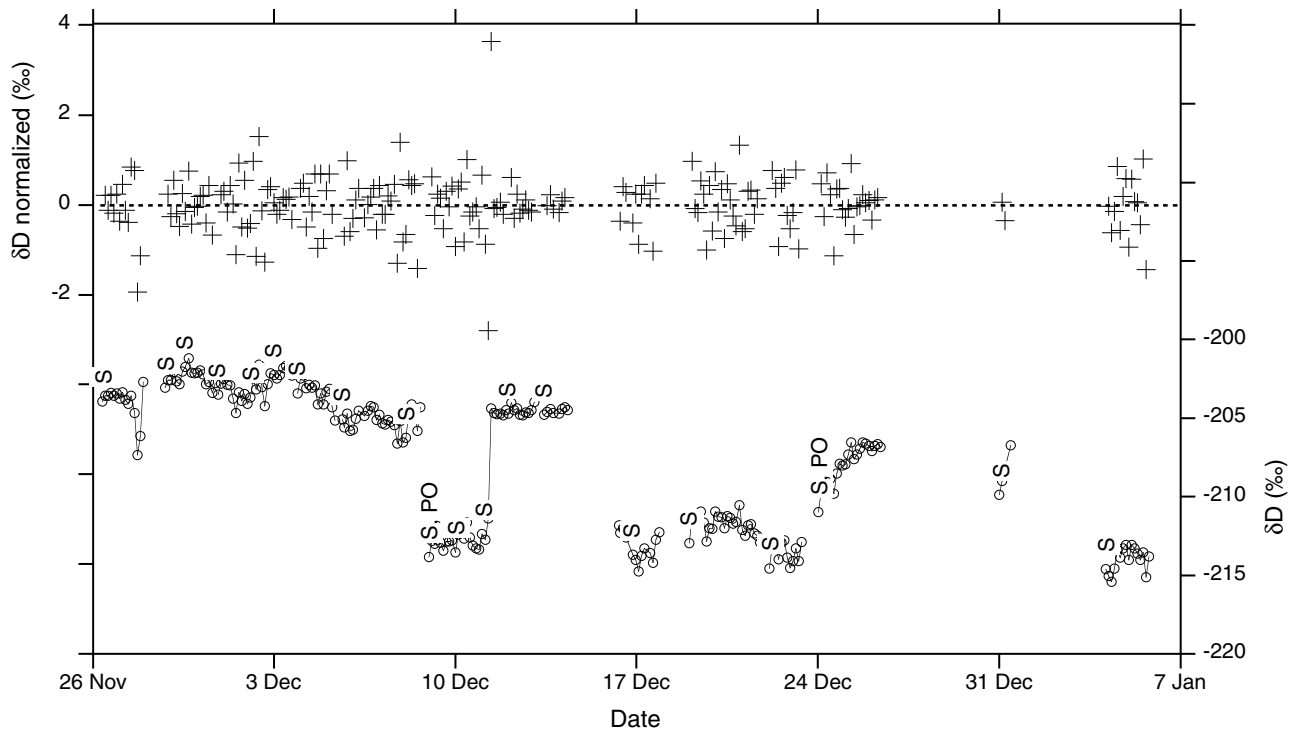


**Figure F15.** Diagrams of wireline tool strings used during Expedition 339. Several variants of the main tool string configurations were run during the expedition; the main configurations are shown here. The APS porosity tool was added to the triple combination in Holes U1387C and U1389E. The HNGS natural gamma ray tool was added to the FMS-sonic tool string in Hole U1386C. For definitions of tool acronyms, see Table T6. LEH-QT = logging equipment head (model QT).

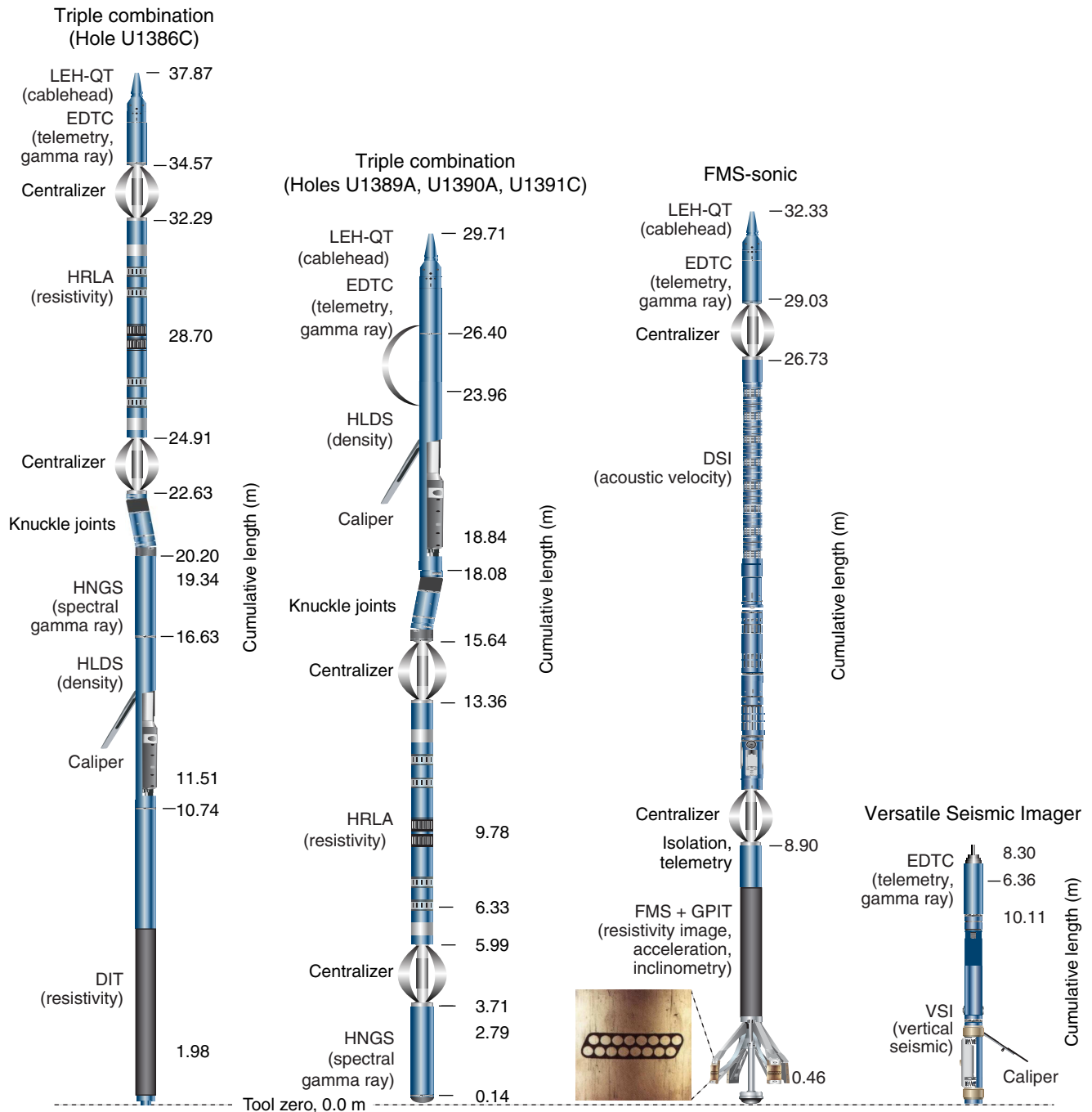


Table T1. Minerals and XRD peak positions, Expedition 339.

Mineral	Window start (°2θ)	Window end (°2θ)	Target angle (°2θ)
Chlorite	6.2	6.3	6.25
Illite	8.7	9.02	8.785
Hornblende	10.3	10.7	10.5
Kaolinite	12.2	12.6	12.4
Aragonite	26.1	26.35	26.25
Quartz	26.45	26.95	26.7
K-feldspar	27.35	27.79	27.57
Plagioclase	27.8	28.15	27.975
Calcite	29.25	29.6	29.425
Augite	29.7	30	29.85
Dolomite	30.65	31.1	30.96
Pyrite	33	33.1	33.05

Table T2. Calcareous nannofossil datums and regional distribution, Expedition 339.

Calcareous nannofossil event	Age calibration (Ma)	Polarity interval	Region
LrO <i>Emiliana huxleyi</i> (>4 μm)	0.01	C1n	Atlantic
FO <i>Emiliana huxleyi</i>	0.28/0.26	C1n	Atlantic, Mediterranean
LO <i>Pseudoemiliana lacunosa</i>	0.44/0.46	C1n	Atlantic, Mediterranean
LO <i>Reticulofenestra asanoi</i>	0.905/0.901	C1r.1r	Atlantic, Mediterranean
Reentrance medium <i>Gephyrocapsa</i>	1.007/0.956	C1r.1n	Atlantic, Mediterranean
FO <i>Reticulofenestra asanoi</i>	1.13/1.07	C1r.2r	Atlantic, Mediterranean
LO large <i>Gephyrocapsa</i> (>5.5 μm)	1.25/1.24	C1r.3r	Atlantic, Mediterranean
LO <i>Helicosphaera sellii</i>	1.34/1.25	C1r.3r	Pacific, Mediterranean
FcO large <i>Gephyrocapsa</i> (>5.5 μm)	1.46	C1r.3r	Pacific
FO large <i>Gephyrocapsa</i> (>5.5 μm)	1.56/1.61	C1r.3r	Atlantic, Mediterranean
LO <i>Calcidiscus macintyreii</i>	1.60/1.66	C1r.3r	Atlantic, Mediterranean
FO medium <i>Gephyrocapsa</i> (3–5.5 μm)	1.68/1.73	C1r.3r	Atlantic, Mediterranean
LO <i>Discoaster brouweri</i>	1.92/1.95	C2n/C2r.1r	Atlantic, Mediterranean
AB <i>Discoaster triradiatus</i>	2.13/2.21	C2r.1n/2r	Atlantic, Mediterranean
LO <i>Discoaster pentaradiatus</i>	2.39/2.51	C2r.2r	Atlantic, Mediterranean
LO <i>Discoaster surculus</i>	2.48/2.53	C2r.2r	Atlantic, Mediterranean
LO <i>Discoaster tamalis</i>	2.80	C2An.1n	Atlantic, Mediterranean
LO <i>Sphenolithus</i> spp.	3.52/3.70	C2Ar	Atlantic, Mediterranean
LO <i>Reticulofenestra pseudoumbilicus</i> (>7 μm)	3.81/3.83	C2Ar	Atlantic, Mediterranean
FcO <i>Discoaster asymmetricus</i>	4.12	C2Ar	Mediterranean
LO <i>Amaurolithus primus</i>	4.50	C3n.1r/2r	Pacific
LO <i>Ceratolithus acutus</i>	5.04	C3n.4n	Atlantic
FO <i>Ceratolithus rugosus</i>	5.05	C3n.4n	Atlantic
LO <i>Triquetrorhabdulus rugosus</i>	5.27	C3r	Atlantic
FO <i>Ceratolithus acutus</i>	5.34	C3r	Atlantic
LO <i>Discoaster quinquerramus</i>	5.54	C3r	Atlantic, Mediterranean
LO <i>Amaurolithus amplificus</i>	5.97/5.93	C3r	Atlantic, Mediterranean
FO <i>Amaurolithus amplificus</i>	6.90/6.68	C3Ar	Atlantic, Mediterranean
FO <i>Amaurolithus</i> spp.	7.36/7.42	C3Br.2r	Atlantic, Mediterranean

Age calibration based on Raffi et al. (2006) and Flores et al. (2010). Polarity interval from ATNTS04 (Lourens et al., 2004). FO = first occurrence, LO = last occurrence, AB = acme bottom. FcO = first common occurrence, LcO = last common occurrence, LrO = last regular occurrence.



**Table T3.** Planktonic foraminifer stratigraphic events and regional distribution, Expedition 339.

Planktonic foraminifer event	Age (Ma)	Polarity interval	Reference	Region
T paracme <i>Neogloboquadrina pachyderma</i> (sin)	1.21	Below B C1r.2n (Cobb Mountain)	Lourens et al., 2004	North Atlantic, Mediterranean
B paracme <i>Neogloboquadrina pachyderma</i> (sin)	1.37	Below B C1r.2n (Cobb Mountain)	Lourens et al., 2004	North Atlantic, Mediterranean
FcO <i>Neogloboquadrina pachyderma</i> (sin)	1.79	Near/below B C1r.3r	Lourens et al., 2004	North Atlantic, Mediterranean
FO <i>Globorotalia truncatulinoides</i>	2.00	C2r.1r	Lourens et al., 2004	North Atlantic, Mediterranean
FO <i>Globorotalia inflata</i> (Sprovieri, 1993)	2.09	Above B C2r.1r	Lourens et al., 2004	North Atlantic, Mediterranean
LO <i>Globorotalia miocenica</i>	2.38	C2r.2r (Matuyama)	Lourens et al., 2004	Atlantic
LO <i>Neogloboquadrina atlantica</i> (sin)	2.41	Near B C2r.2r (Matuyama)	Weaver and Clement, 1987	North Atlantic
LO <i>Globorotalia puncticulata</i>	2.41	Near B C2r.2r (Matuyama)	Lourens et al., 2004	North Atlantic, Mediterranean
FO <i>Neogloboquadrina atlantica</i> (sin)	2.72	C2An.1n (Gauss)	Lourens et al., 2004	North Atlantic, Mediterranean
LO <i>Dentoglobigerina altispira</i>	3.17	Near/below B C2An.2n	Lourens et al., 2004	Atlantic, Mediterranean
LO <i>Sphaeroidinellopsis seminulina</i>	3.19	Near/above B C2An.2n	Hilgen, 1991	Mediterranean
T temporal disappearance <i>Globorotalia puncticulata</i>	3.31	Near B C2An.2r (Mammoth)	Lourens et al., 2004	North Atlantic, Mediterranean
B temporal disappearance <i>Globorotalia puncticulata</i>	3.57	Near B C2An.3n (Gauss)	Lourens et al., 2004	North Atlantic, Mediterranean
LO <i>Globorotalia margaritae</i> (Chaisson and Pearson, 1997)	3.81	C2Ar (Gilbert)	Lourens et al., 2004	North Atlantic, Mediterranean
LaO <i>Globorotalia margaritae</i>	3.98	C2Ar (Gilbert)	Lourens et al., 2004	North Atlantic, Mediterranean
LO <i>Globigerina nepenthes</i>	4.37	C3n.1r	Chaisson and Pearson, 1997	North Atlantic, Mediterranean
FO <i>Globorotalia crassaformis</i>	4.50	C3n.2n (Nunivak)	Chaproniere et al., 1994	Atlantic
FO <i>Globorotalia puncticulata</i>	4.52	C3n.2n (Nunivak)	Lourens et al., 2004	North Atlantic, Mediterranean
FaO <i>Globorotalia margaritae</i>	5.80	C3r (Gilbert)	Krijgsman et al., 2004	North Atlantic
LaO <i>Globorotalia miotumida</i>	6.35	Below B C3A.1n	Krijgsman et al., 2004	North Atlantic
<i>Neogloboquadrina pachyderma</i> (sin)/(dex) coiling change	6.37	Below B C3A.1n	Lourens et al., 2004	North Atlantic, Mediterranean
FcO <i>Globorotalia miotumida</i> group	7.24	Near B C3Br.1r	Lourens et al., 2004	Atlantic, Mediterranean

Reference after species name indicates primary reference. Polarity intervals from ATNTS04 (Lourens et al., 2004). T = top, B = bottom, LO = last occurrence, FO = first occurrence, LaO = last abundant occurrence, FaO = first abundant occurrence, FcO = first common occurrence. sin = sinistral, dex = dextral.

**Table T4.** Pollen morphotypes and temporal and regional occurrences, Expedition 339.

More abundant pollen morphotype	Epoch	Age (Ma)	Region
Mediterranean forest: Deciduous <i>Quercus</i> , evergreen <i>Quercus</i> , <i>Pinus</i> , <i>Olea</i> , <i>Phillyrea</i> , <i>Pistacia</i> , <i>Cistus</i>	Holocene Late Pleistocene Late mid-Pleistocene	~0.425–present	Southwest Iberia (Lézine and Denèfle, 1997; Sánchez Goñi et al., 1999, 2000, 2008, 2009; Roucoux et al., 2006; Margari et al., 2010)
Semidesert: <i>Artemisia</i> , Chenopodiaceae, <i>Ephedra dystachia</i> type, <i>Ephedra</i> <i>fragilis</i> type			
Others: Ericaceae, Cupressaceae, Asteraceae			
Temperate and subtropical plants: Deciduous <i>Quercus</i> , Ericaceae	Early mid-Pleistocene Early Pleistocene Gelasian	2.6–0.425	Southeast Iberia (Joannin et al., 2011, for MIS 31–23)
High/mid-altitude conifers: <i>Cedrus</i> , <i>Abies</i> , <i>Tsuga</i> (presence), <i>Picea</i> (presence)			
Semidesert: <i>Artemisia</i> , <i>Ephedra</i>			
Herbs: Asteraceae, Caryophyllaceae, Poaceae			
Others: <i>Pinus</i>			
Mega-mesothermic trees: <i>Cathaya</i> , <i>Engelhardtia</i> , <i>Sequoia</i> , <i>Myrica</i> , <i>Taxodium</i>	Pliocene	5.3–2.6	Southwest Iberia (Jiménez-Moreno et al., 2010)
Mediterranean xerophytes: <i>Olea</i> , <i>Phillyrea</i> , <i>Cistus</i> , Rhamnaceae, evergreen <i>Quercus</i>			
Others: Ericaceae, <i>Pinus</i>			
Herbs: Poaceae, Asteraceae	Messinian	7.2–5.3	Southwest Iberia (Jiménez-Moreno et al., 2010)
Semidesert: <i>Lygeum</i> , <i>Neurada</i>			
Trees: <i>Pinus</i> , deciduous <i>Quercus</i>			
Herbs: Poaceae, Asteraceae, <i>Nitraria</i> , <i>Calligonum</i>			South Iberia (Jiménez-Moreno et al., 2010)
Semidesert: <i>Lygeum</i> , <i>Neurada</i>			
Trees: <i>Pinus</i> , deciduous <i>Quercus</i> , Taxodiaceae, <i>Myrica</i> , <i>Alnus</i>			
High/mid-altitude conifers: <i>Cathaya</i> , <i>Tsuga</i> , <i>Cedrus</i> , <i>Abies</i> , <i>Picea</i>	Tortonian	~11.6–7.2	South Iberia (Jiménez-Moreno et al., 2010)
Herbs and shrubs: Poaceae, Amaranthaceae-Chenopodiaceae, <i>Ephedra</i> , Plumbaginaceae, Caryophyllaceae, <i>Plantago</i> , <i>Tamarix</i> , <i>Nitraria</i> , <i>Lygeum</i> , <i>Prosopis</i> , <i>Neurada</i> , <i>Calligonum</i>			
Others: <i>Pinus</i>			

MIS = marine isotope stage.

**Table T5.** Wireline tool string downhole measurements, Expedition 339.

Tool string	Tool	Measurement	Sampling interval (cm)	Approximate vertical resolution (cm)
Triple combination	HNGS	Spectral gamma ray	15	20–30
	APS	Porosity	5 and 15	36
	HLDS	Bulk density	2.5 and 15	38
	DIT	Resistivity	15	240/180/92
	HRLA	Resistivity	15	30
Formation MicroScanner-sonic	HNGS	Spectral gamma ray	15	20–30
	GPIIT	Tool orientation	3.8	15
	FMS	Microresistivity	0.25	0.5
	DSI	Acoustic velocity	15	107
Versatile Seismic Imager	EDTC	Total gamma ray	15	30
	VSI	Acoustic travelttime	Stations at 25 m	NA

Tool names are trademarks of Schlumberger. See Table T6 for explanations of acronyms used to describe tool strings and tools. NA = not applicable.

**Table T6.** Acronyms and units used for downhole wireline tools and measurements, Expedition 339.

Tool	Output	Description	Unit
APS		Accelerator Porosity Sonde	
	APLC	Near array limestone porosity corrected	%
	STOF	Computed standoff	inch
	SIGF	Formation capture cross section	Capture units
DIT		Dual Induction Tool	
	IDPH	Deep induction resistivity	$\Omega\text{m}$
	IMPH	Medium induction resistivity	$\Omega\text{m}$
	SFLU	Spherically focused resistivity	$\Omega\text{m}$
DSI		Dipole Sonic Imager	
	DTCO	Compressional wave slowness ( $\Delta t$ )	$\mu\text{s}/\text{ft}$
	DTSM	Shear wave slowness ( $\Delta t$ )	$\mu\text{s}/\text{ft}$
FMS		Formation MicroScanner	
	C1, C2	Orthogonal hole diameters	inch
	P1AZ	Pad 1 azimuth	$^{\circ}$
		Spatially oriented resistivity images of borehole wall	
GPIT		General Purpose Inclinator Tool	
	DEVI	Hole deviation	$^{\circ}$
	HAZI	Hole azimuth	$^{\circ}$
	F <sub>x</sub> , F <sub>y</sub> , F <sub>z</sub>	Earth's magnetic field (three orthogonal components)	$^{\circ}$
	A <sub>x</sub> , A <sub>y</sub> , A <sub>z</sub>	Acceleration (three orthogonal components)	$\text{m}/\text{s}^2$
HLDS		Hostile Environment Litho-Density Sonde	
	RHOM	Bulk density	$\text{g}/\text{cm}^3$
	PEFL	Photoelectric effect	b/e <sup>-</sup>
	LCAL	Caliper (measure of borehole diameter)	inch
	DRH	Bulk density correction	$\text{g}/\text{cm}^3$
HNGS		Hostile Environment Gamma Ray Sonde	
	HSGR	Standard (total) gamma ray	gAPI
	HCGR	Computed gamma ray (HSGR minus uranium contribution)	gAPI
	HFK	Potassium	wt%
	HTHO	Thorium	ppm
	HURA	Uranium	ppm
HRLA		High-Resolution Laterolog Array tool	
	RLA1-5	Apparent resistivity from computed focusing modes 1-5	$\mu\text{m}$
	RT	True resistivity	$\mu\text{m}$
	MRES	Borehole fluid resistivity	$\mu\text{m}$
EDTC		Enhanced Digital Telemetry Cartridge	
	GR_EDTC	Total gamma ray	gAPI
	A <sub>x</sub> , A <sub>y</sub> , A <sub>z</sub>	Acceleration (three orthogonal components)	$\text{m}/\text{s}^2$
VSI		Versatile Seismic Imager	
		Acoustic traveltimes	ms

For the complete list of acronyms used in IODP and for additional information about tool physics, consult IODP-USIO Science Services, LDEO, at [iodp.ldeo.columbia.edu/TOOLS\\_LABS/tools.html](http://iodp.ldeo.columbia.edu/TOOLS_LABS/tools.html).